
HTGR Graphite Core Component Stress Analysis Research Program – Task 1 Technical Letter Report

Manuscript Completed: September, 2011
Date Published:

Prepared by
S. Mohanty and S. Majumdar
Argonne National Laboratory
Argonne, IL 60439

M. Srinivasan, NRC Project Manager

Prepared for
Division of Engineering
Office of Nuclear Regulatory Research
U.S. Nuclear Regulatory Commission
Washington, DC 20555
NRC Job Code V6218



This page is intentionally left blank.

ABSTRACT

This is the Task 1 technical letter report of the NRC-sponsored HTGR Graphite Core Components Stress Analysis Research program. The report summarizes the results from a literature search of the current graphite core components stress analysis models that incorporate graphite nonlinear behavior and the contribution and role played by irradiation creep of graphite in governing its properties. Physical and mechanical properties of graphite are collected and evaluated; changes in the properties due to neutron irradiation are documented. Material models to account for effects of change of temperature and neutron fluence on mechanical and physical properties are reviewed.

This page is intentionally left blank.

CONTENT

ABSTRACT.....	III
FIGURES.....	IX
TABLES.....	XIII
EXECUTIVE SUMMARY.....	XVII
ACKNOWLEDGMENTS.....	XIX
ACRONYMS AND ABBREVIATIONS.....	XXI
SYMBOLS.....	XXIII
1. INTRODUCTION.....	1
1.1 Peach Bottom Reactor Unit-I.....	1
1.2 Fort St. Vrain Nuclear Reactor.....	1
1.3 General Atomics Gas Turbine Modular Helium Reactor (GT-MHR).....	2
1.4 Other International HTGR Programs.....	2
1.5 Current HTGRs in the Context of Generation IV and NGNP Programs.....	3
1.6 Motivation for This Research Program.....	4
2. LITERATURE REVIEW AND EVALUATION OF HTGR STRESS ANALYSIS/HEAT CONDUCTION METHODS.....	7
2.1 Finite Element Stress Analysis Model.....	7
2.2 Analytical Stress Analysis Models.....	10
2.3 Analytical Heat Conduction Model.....	11
3. REVIEW OF HTGR GRAPHITE CORE DESIGN STANDARDS.....	13
3.1 ASME Code, Section III, Division 5, Subsection HH ²⁸	13
3.1.1 Classification of Graphite Core Components (HHA-3111 and 3112).	13
3.1.2 Loadings (HHA-3122).....	14

3.1.3	Terms Relating to Design and Service Loading (HHA-3124)	14
3.1.4	Terms Related to Stress Analysis (HHA-3214)	15
3.1.5	Irradiation Fluence Limits (HHA-3142.1)	15
3.1.6	Stress Limits for Graphite Core Components (HHA-3220, 3230, 3240).....	16
3.1.7	Material Properties Requirements for Design (Mandatory Appendix HHA-II- 2000)	17
3.2	Japanese (JAEA) Code for HTGR Graphite Core Components.....	19
3.2.1	Graphite Component Class Terminology	19
3.2.2	JAEA Design Limits	20
4.	REVIEW OF GRAPHITE CORE COMPONENTS	23
4.1	Candidate Graphite Grade Options for HTGR\INGNP Program.....	23
4.2	Ideal Requirements for HTGR Graphite Grade	24
4.3	Typical Graphite Core Geometry and Dimensions	25
4.4	Preliminary Neutronics Information for Stress Analysis.....	28
4.5	Thermal Hydraulics Input for Stress Analysis	30
4.6	Irradiation damage mechanics in graphite.....	30
4.6.1	Graphite Microstructure	31
4.6.2	Mechanism of Irradiation Induced Dimensional Change in Nuclear Graphite ...	32
4.6.3	Effects of Grain Orientation and Irradiation Temperature on Dimensional Change.....	33
4.7	Oxidation of Graphite.....	34
4.7.1	Reactions and Thermodynamics	34
4.7.2	Oxidation Mechanisms	35
4.7.3	Oxidation Regimes and Kinetics.....	36
5.	GRAPHITE MATERIAL PROPERTIES AND MATERIAL MODELS.....	39
5.1	Non-irradiated H-451 & IG-110 Graphite Material Properties.....	39

5.1.1	Non-irradiated Stress-Strain Curve	41
5.1.2	Effect of Oxidation on Material Properties	42
5.2	Irradiated Material Properties and Material Models	43
5.2.1	Irradiation-induced Dimension Change Material Data and Material Models	45
5.2.2	Irradiated coefficient of thermal expansion (CTE) change material data and model.....	48
5.2.3	Irradiated elastic modulus change material data	50
5.2.4	Irradiated Strength Change Material Data	53
5.2.5	Irradiated Thermal Conductivity Change Material Data and Model.....	55
5.2.6	Effect of Water Vapor Oxidation on Irradiated Material Properties.....	59
5.3	Semi-Empirical Material Models	60
6.	IRRADIATED CREEP MATERIAL MODELS.....	61
6.1	H-451 Graphite	61
6.2	IG-110 Graphite.....	65
6.3	Irradiated Creep Poisson's Ratio	65
6.4	Irradiation Creep Interaction Effects	66
6.4.1	Effect of Creep Strain on Coefficient of Thermal Expansion	67
6.4.2	Effect of Creep Strain on Dimensional Change Strain	67
7.	PROPOSED STRESS ANALYSIS CODE AND APPROACH	69
7.1	Analysis Steps	69
7.2	Direct Matrix Inversion Method	71
8.	CONCLUSIONS.....	73
	REFERENCES	75
	APPENDIX A GRADE H-451 GRAPHITE PROPERTIES DATA.....	81
A1	Dimensional Change Strain.....	81

A2	Coefficient of Thermal Expansion (CTE).....	84
A3	Tensile Strength	88
A4	Elastic Modulus	90
A5	Thermal Conductivity.....	93
APPENDIX B GRADE IG-110 GRAPHITE PROPERTIES DATA		95
B1	Dimensional Change Strain.....	95
B2	CTE	99
B3	Tensile Strength	102
B4	Elastic Modulus	106
B5	Thermal Conductivity.....	111
B6	Creep Coefficient.....	114

FIGURES

Figure 1.	Maxwell-Kelvin Model of Graphite.....	7
Figure 2.	Maxwell-Kelvin Model of Graphite (Iyoku ¹⁶).	8
Figure 3.	Cross-section of a cylinder with uniformly spaced m number of cooling holes. 11	
Figure 4.	Core arrangement of GT-MHR. ²³	26
Figure 5.	Dimensions of a typical outer reflector block. ²³	27
Figure 6.	Typical prismatic fuel element dimensions. ²³	27
Figure 7.	1/6 th of core section ³²	28
Figure 8.	Fast neutron flux near core mid plane or maximum core fluxes. ³²	29
Figure 9.	Fast neutron flux near core mid plane for neutrons of energy >0.18 MeV. ³² ..	29
Figure 10.	Neutron fluence at different rings with respect to operating years	30
Figure 11.	Schematic of graphite microstructure. Each basal plane consists of honeycomb-like hexagonal lattice. The axis parallel to basal plane is referred as a-axis, and perpendicular to basal plane is referred as c-axis.	31
Figure 12.	Schematic showing interstitial defects (swelling along 'c' direction).....	32
Figure 13.	Schematic showing vacancy defects (shrinkage along 'a' direction).....	33
Figure 14.	Uniaxial stress-strain curves of IG-110 at room temperature in tension (red) and compression (blue).....	41
Figure 15.	(a) Tensile and (b) compressive stress-strain curves (black lines) of IG-110 and the Ramberg-Osgood equation fits (blue lines) and Jenkin's equation fits (red lines).....	42
Figure 16.	Strength change of IG-110 graphite due to oxidation.....	43
Figure 17.	Rescaled H-451 dimensional change data taken from General Atomics Report. ⁴⁰	45
Figure 18.	Calculated values of dimensional change strain in H-451 graphite.....	46
Figure 19.	Rescaled IG-110 dimensional change data taken from JAERI report.	47

Figure 20.	Rescaled CTE change data for H-451 graphite (original data taken from General Atomics graphite handbook. ⁴⁰).....	48
Figure 21.	Rescaled CTE change data for IH-110 graphite (original data taken from JAERI Graphite Handbook.)	49
Figure 22.	Rescaled Young's modulus change data for H-451 graphite (original data taken from the General Atomics handbook ⁴⁰).....	50
Figure 23.	Original vs. fitted (regenerated) dynamic Young's modulus of H-451.	51
Figure 24.	Rescaled elastic modulus change data for IG-110 graphite (original data taken from JAERI report).....	52
Figure 25.	Rescaled UTS change data for H-451 graphite (original data taken from a General Atomics report ⁴⁷).	53
Figure 26.	Rescaled UTS change data for IG-110 graphite (original data taken from JAERI report.)	54
Figure 27.	Rescaled thermal conductivity change data for H-451 graphite (original data taken from a General Atomics Handbook ⁴⁰ . Note: the thermal conductivity at non-irradiated condition (i.e. K_0) considered average of the against grain (AG) and with grain (WG) non-irradiated thermal conductivity as given in Table 11.56	56
Figure 28.	Original ~ fitted thermal conductivity change data for H-451.	58
Figure 29.	Rescaled thermal conductivity change data for IG-110 graphite (original data taken from JAERI report).....	58
Figure 30.	Axial creep strain for H-451 at 900°C and 20.7 MPa compressive stress (Burchell ⁵⁶).....	64
Figure 31.	Axial and radial creep strains for H-451 at 900°C and 13.8 MPa compressive stress (Burchell ⁵⁶).	64
Figure 32.	Dependency of Poisson's ratio of H-451 graphite on creep strain (by permission of JAERI)......	66
Figure A1	Design curves for dimensional change of H-451 graphite, axial orientation, as a function of irradiation conditions (General Atomics report ⁴⁰)	81
Figure A2	Design curves for CTE change of H-451 graphite at (a) 650°C and 850°C and at (b) 1050°C and 1250°C, as a function of irradiation conditions (General Atomics report) ⁴⁰	85
Figure A3	Design curves for UTS change of H-451 graphite, as a function of irradiation conditions (General Atomics report).....	88

Figure A4	Design curves for elastic modulus change of H-451 graphite, as a function of irradiation conditions (General Atomics report) ⁴⁰	90
Figure A5	Design curves for thermal conductivity change of various near-isotropic graphite, as a function of irradiation conditions (General Atomics report).....	93
Figure B1	IG-110 graphite irradiation dimensional change data as reported in (by permission of JAERI).....	95
Figure B2	IG-110 graphite irradiation coefficient of thermal expansion data as reported in (by permission of JAERI).....	99
Figure B3	Design curves for UTS change of IG-110 graphite, as a function of irradiation conditions (by permission of JAERI)	102
Figure B4	Design curves for elastic modulus change of IG-110 graphite, as a function of irradiation conditions (by permission of JAERI).....	106
Figure B5	Design curves for thermal conductivity change of IG-110 graphite, as a function of irradiation conditions (by permission of JAERI)	111
Figure B6	Creep coefficient plot of IG-110 graphite, as a function of temperature (by permission of JAERI).....	114

This page is intentionally left blank.

TABLES

Table 1.	Design allowable probability of failure (GA-3221-1).....	16
Table 2.	Grade designation.....	17
Table 3.	Temperature-dependent properties.....	17
Table 4.	Temperature-independent properties.....	18
Table 5.	Design strength values.....	18
Table 6.	Irradiated material properties.	19
Table 7,	List of oxidized condition material properties.	19
Table 8.	Possible graphite grade for HTGR\NGNP program. ³⁰	23
Table 9.	Ideal graphite grade requirements for HTGR\NGNP program. ³⁰	24
Table 10.	Ideal graphite grade requirements for HTGR\NGNP program. ³⁰	25
Table 10.	Non-irradiated properties of H-451 graphite (Virgil'ev and Kalyagina, 2003) ⁴⁴ ..	39
Table 11.	Non-irradiated properties of H-451 graphite (Virgil'ev and Kalyagina, 2003) ⁴⁴ ..	40
Table 11.	Non-irradiated material properties for IG-110 graphite (JAERI report, 2009)...	40
Table 12	Polynomial coefficients for dimensional change strain of H-451 graphite ⁴⁰	46
Table 13	Polynomial coefficients for dimensional change strain material model of IG-110 graphite.	47
Table 14.	Polynomial coefficients for CTE change material model of IG-110 graphite	50
Table 15.	Polynomial coefficients for dynamic Young's modulus of H-451 graphite.....	51
Table 16.	Polynomial coefficients for elastic modulus change material model	53
Table 17	Polynomial coefficients of relative thermal conductivity data on H-451.....	57
Table 18.	Polynomial coefficients a ₁ and a ₂ for thermal conductivity change material model as given in Eq. 39.....	59
Table A1	H-451 graphite irradiation dimensional change data extracted from Fig. A1 using a data processing software (Fluence is in X 10 ²¹ n/m ²).....	82
Table A1	H-451 graphite irradiation dimensional change data extracted from Fig. A1 using a data processing software (Fluence is in X 10 ²¹ n/m ²).....	83

Table A2	H-451 graphite irradiation CTE change data extracted from Figure A3 and A4 using a data processing software (Fluence is in $X 10^{21} \text{ n/m}^2$).....	86
Table A2	H-451 graphite irradiation CTE change data extracted from Figure A3 and A4 using a data processing software (Fluence is in $X 10^{21} \text{ n/m}^2$).....	87
Table A3	H-451 graphite irradiation UTS change data extracted from Fig. A6 using a data processing software (Fluence is in $X 10^{25} \text{ n/m}^2$).	89
Table A4	H-451 graphite irradiation elastic modulus change data extracted from Fig. A8 using a data processing software (Fluence is in $X 10^{26} \text{ n/m}^2$).....	91
Table A4	H-451 graphite irradiation elastic modulus change data extracted from Fig. A8 using a data processing software (Fluence is in $X 10^{26} \text{ n/m}^2$).....	92
Table A5	H-451 (axial direction) graphite irradiation thermal conductivity change data extracted from Fig. A10 using a data processing software (Fluence is in $X 10^{25} \text{ n/m}^2$).....	94
Table B1	IG-110 graphite irradiation dimensional change data extracted from Fig. A2 using a data processing software (Fluence is in $X 10^{26} \text{ n/m}^2$).....	96
Table B1	IG-110 graphite irradiation dimensional change data extracted from Fig. A2 using a data processing software (Fluence is in $X 10^{26} \text{ n/m}^2$).....	97
Table B1	IG-110 graphite irradiation dimensional change data extracted from Fig. A2 using a data processing software (Fluence is in $X 10^{26} \text{ n/m}^2$).....	98
Table B2	IG-110 graphite irradiation CTE change data extracted from Fig. A6 using a data processing software (Fluence is in $X 10^{26} \text{ n/m}^2$).	100
Table B2	IG-110 graphite irradiation CTE change data extracted from Fig. A6 using a data processing software (Fluence is in $X 10^{26} \text{ n/m}^2$).	101
Table B3	IG-110 graphite irradiation UTS change data extracted from Figure A7 using a data processing software (Fluence is in $X 10^{26} \text{ n/m}^2$).	103
Table B3	IG-110 graphite irradiation UTS change data extracted from Figure A7 using a data processing software (Fluence is in $X 10^{26} \text{ n/m}^2$).	103
Table B3	IG-110 graphite irradiation UTS change data extracted from Figure A7 using a data processing software (Fluence is in $X 10^{26} \text{ n/m}^2$).	105
Table B4	IH-110 graphite irradiation elastic modulus change data extracted from Fig. A9 using a data processing software (Fluence is in $X 10^{26} \text{ n/m}^2$).....	107
Table B4	IH-110 graphite irradiation elastic modulus change data extracted from Fig. A9 using a data processing software (Fluence is in $X 10^{26} \text{ n/m}^2$).....	108

Table B4	IH-110 graphite irradiation elastic modulus change data extracted from Fig. A9 using a data processing software (Fluence is in $\times 10^{26}$ n/m ²).	109
Table B4	IH-110 graphite irradiation elastic modulus change data extracted from Fig. A9 using a data processing software (Fluence is in $\times 10^{26}$ n/m ²).	110
Table B5	IG-110 graphite irradiation thermal conductivity change data extracted from Fig. A11 using a data processing software (Fluence is in $\times 10^{26}$ n/m ²).	111
Table B5	IG-110 graphite irradiation thermal conductivity change data extracted from Fig. A11 using a data processing software (Fluence is in $\times 10^{26}$ n/m ²).	112
Table B5	IG-110 graphite irradiation thermal conductivity change data extracted from Fig. A11 using a data processing software (Fluence is in $\times 10^{26}$ n/m ²).	113
Table B6	The numerical values of the IG-110 irradiation creep coefficient extracted from Fig. B6 using a data processing software.	115

This page is intentionally left blank.

EXECUTIVE SUMMARY

In the core of a high temperature gas-cooled reactor (HTGR), graphite components act as neutron moderators and reflectors, contain fuel elements, and provide a conduction path for helium coolant. During normal reactor operation, graphite core components are subjected to varying temperatures (up to about 1,273 °K) and fluences (up to 10^{23} n/cm²). The temperature and fluence at a given location depend on whether the graphite brick is at the inlet or at the outlet of the coolant flow, at the center or at the periphery of the core, or at the bottom or the top of the core/core support structure. The cumulative dose causes damage to the graphite crystal lattice and the general structure. This damage in turn affects the governing properties, ultimately influencing the load-bearing capacity of core components. Excessive deformation of the core bricks could result in distortion of the coolant and control rod channels as well as a potential increase in the coolant bypass flow.

The U.S. Nuclear Regulatory Commission (NRC) staff has initiated a research program at Argonne National Laboratory (ANL) to develop a suitable methodology for modeling governing properties for use in finite element stress analysis of graphite core components. The methodology, which incorporates the effects of irradiation-induced degradation, will be the basis for an independent structural finite-element analysis (FEA) tool to estimate the stresses in graphite core components of an HTGR. This methodology will be useful to both licensees and the staff who will use it to verify and confirm applicants' data, models, and technical bases for ensuring the structural integrity of graphite core components and the operational safety of the HTGR itself.

The American Society of Mechanical Engineers (ASME) has developed a draft rule for the design of HTGR graphite core components. Currently, there are several distinctly different stress analysis codes for graphite components, which are design-specific, and, thus, proprietary to the HTGR vendors. No consensus, unified stress analysis code for graphite components has been verified and validated by a benchmark exercise. The ASME draft code case may be evaluated in this research for possible acceptance and endorsement via the publication of a regulatory guide detailing such analysis procedure.

Work in this program is divided into the following four technical tasks:

Task 1 Evaluate current graphite core stress analysis models; Issue a technical letter report on graphite core stress analysis models.

Task 2 Develop a finite-element stress analysis code; Issue a technical letter report on graphite core stress analysis.

Task 3 Conduct verification and validation of the stress analysis method.

Task 4 Publish the methodology.

As a first step in this research, ANL has completed Task 1 which is a review of published literature on the stress analysis of graphite components used in existing and developmental gas-cooled reactors. This report provides an overview of the complex aspects of nonlinear and time- and dose-dependent properties that influence the load-bearing capability of graphite components. Using existing data from previous reactor grade graphites, ANL has developed

preliminary material behavior model empirical relationships that can be used as input data in finite element model and stress estimation. Additional research will involve the consideration of uncertainties in the data and procedures to incorporate such uncertainties into the stress analysis model.

This report summarizes the results from Task 1 of the HTGR Graphite Core Components Stress Analysis Research program. The primary objective of Task 1 is to evaluate current graphite core stress analysis models. As specified in this task, we conducted review and evaluation of currently-published information on the subject of HTGR graphite core stress analysis models and procedures, including input material data through established relationships for various graphite classes that are intended for use in NGNP HTGR graphite core components. We realize that there could be other potential stress analysis methodology, which may be available, such as the British Energy (now EdF) proprietary method used to evaluate the British AGRs. The search for finite-element analysis assessment included the following properties:

- a) Non-irradiated Properties:
 - i. Young's modulus versus temperature
 - ii. Elastic Poisson's ratio
 - iii. Coefficient of thermal expansion (CTE) versus temperature
 - iv. Thermal conductivity versus temperature
- b) Irradiated properties as a function of temperature and irradiation dose
 - v. Dimensional Change
 - vi. CTE
 - vii. Young's modulus
 - viii. Elastic Poisson's ratio
 - ix. Thermal conductivity
- c) Irradiation creep as a function of temperature, dose, and stress
 - x. Creep law constants and variables
 - xi. Poisson ratio in creep
- d) Effect of oxidation on graphite mechanical properties
- e) Interaction between Irradiation creep and thermal expansion and dimensional change strains

Significant data were obtained for graphite grades H-451 and IG-110. However, the grades of graphite chosen for NGNP are different and their properties are currently being measured at Idaho National Laboratory and at Oak Ridge National Laboratory, and not yet available.

The finite element code ABAQUS was chosen for conducting the heat conduction and stress analyses of graphite core components. A procedure has been developed to incorporate the graphite properties into the ABAQUS code. A user-defined subroutine UMAT is being implemented for taking into account the interactive thermal and dimensional change strains due to irradiation creep.

ACKNOWLEDGMENTS

This work is sponsored by the Office of Nuclear Regulatory Research, U.S. Nuclear Regulatory Commission, under Job Code V6218; Program Manager: Dr. M. Srinivasan.

This page is intentionally left blank.

ACRONYMS AND ABBREVIATIONS

AEA	Atomic Energy Act
AEC	Atomic Energy Commission
AG	Against Grain
ANL	Argonne National Laboratory
ASME	American Society of Mechanical Engineers
AVR	German Pebble Bed Reactor
CFD	Computational Fluid Dynamics
CTE	Coefficient of Thermal expansion
dpa	Displacement per atom - damage dose unit
EdF	Electricité de France
EDN	Equivalent DIDO Nickel - damage dose unit
FE	Finite Element
GCFR	Gas Cooled Fast Reactor
GT-MHR	Gas Turbine Modular Helium Reactor
HTGR	High Temperature Gas Cooled Reactor
HTR	High Temperature Reactor
HTR-PM	High Temperature Gas-Cooled Reactor-Pebble bed Module
HTTR	High Temperature Test Reactor
INL	Idaho National Laboratory
JAERI	Japan Atomic Energy Research Institute
LFR	Lead Cooled Fast Reactor
LWR	Light Water Reactor
MDE	Maximum Deformation Energy
MW _e	Megawatt Electric
MW _{th}	Megawatt Thermal
MSR	Molten Salt Cooled Fast Reactor
NRC	Nuclear Regulatory Commission
ORNL	Oak Ridge National Laboratory
PWR	Pressurized Water Reactor
SCWR	Super Critical Water Reactor
SFR	Sodium Cooled Fast Reactor
UMAT	User-Defined Material Properties Subroutine
VHTR	Very High Temperature Gas Cooled Reactor
WG	With Grain

This page is intentionally left blank.

SYMBOLS

i	Subscript 'i' represents irradiated
o	Subscript 'o' represents original or unirradiated
pc	Superscript 'pc' represents primary creep
sc	Superscript 'sc' represents secondary creep
t	Time
Δt	Time increment
γ	Fluence
θ	Temperature
E	Elastic young's modulus
S	UTS or strength
ν	Poisson's ratio
α	Coefficient of thermal expansion
K	Thermal conductivity
K^c	Creep constant
ϵ	Total strain
ϵ^e	Elastic strain
ϵ^{pc}	Primary creep strain
ϵ^{sc}	Secondary creep strain
ϵ^θ	Thermal strain
ϵ^{dc}	Dimensional change strain
$\epsilon^{i\theta}$	Interaction thermal strain
ϵ^{idc}	Interaction dimensional change strain

This page is intentionally left blank.

1. INTRODUCTION

The high temperature gas-cooled reactor (HTGR) is a gas cooled reactor with a graphite core that can operate at reactor outlet temperatures much higher than conventional light water reactors (LWRs). In recent years, the interest in HTGR technology has been increasing in the United States and other countries due to a growing recognition of the potential of HTGRs to provide high efficiency, cost effective electricity and process heat. The following subsections briefly describe the historical development of HTGR technology in the US and abroad.

1.1 Peach Bottom Reactor Unit-I

The HTGR design was first proposed by Oak Ridge National Laboratory (then Power Pile Division of the Clinton Laboratory) in 1947¹. The Peach Bottom reactor in the United States was the first HTGR to produce electricity. The Unit-I of the Peach Bottom reactor was based on HTGR technology and designed and operated successfully as concept demonstration. It was operated from 1966 through 1974 and had a power generation capacity of 40 MWe. The Peach Bottom reactor was a helium-cooled, graphite-moderated, 115 MWt reactor operating on a thorium-uranium fuel cycle. The outlet and inlet coolant temperatures were 700°C and 300°C, respectively. The reactor used standard fuel elements and had the outward appearance of a graphite cylinder 3.5 in. in diameter and 12 ft. long. The core was designed to contain 804 fuel elements. The standard fuel element was a solid semi homogeneous graphite block in which graphite served as the moderator, reflector, and structure, and contained the cladding and fuel matrix. The performance of almost all reactor systems was without major problems, verifying in many areas the design philosophy. The decision to shut down and decommission the Peach Bottom HTGR in October 1974 was based upon several factors. First and foremost was the fact that the program for which the plant had been originally designed was completed; second, the objective of demonstrating the technical feasibility and commercial operation of an HTGR had been met with; and third, the size of the Peach Bottom Unit 1 plant (of 40 MW(e)) made it uneconomical in terms of operating costs or manpower relative to the large nuclear plants. A more detailed review can be found in the publications of Kohler² and Kingrey³.

The original 40-year license term for the Peach Bottom Reactor, Unit 1 was selected on the basis of economic and antitrust considerations, not technical limitations. However, some individual plant and equipment designs may have been engineered on the basis of an expected 40-year service life.⁴

1.2 Fort St. Vrain Nuclear Reactor

Fort St. Vrain (FSV) HTGR⁵ was based on the original design of Peach Bottom demonstration HTGR. It operated from 1977 until 1992. The reactor had a power output of 330MWe (842 MWt). The reactor fuel was a combination of fissile uranium and fertile thorium microspheres dispersed within a prismatic graphite matrix. Many problems related to water infiltration and corrosion issues, electrical system issues, and general facility issues occurred early in the operational experience of the FSV HTGR. Though these issues did not threaten the safety of the station, the problems that did occur put considerable stress upon the personnel, equipment, and facilities present at FSV. The economical consideration caused the owner of the FSV power plant to shut it down prior to the end of its design life.

Both the construction permit and the operating license granted to FSV were issued under Section 104(b) of the *Atomic Energy Act of 1954*, as amended, (AEA). Therefore, the Atomic Energy Commission (AEC) and later the Nuclear Regulatory Commission (NRC) imposed “the minimum amount of such regulations and terms of license as will permit the Commission to fulfill its obligations under this chapter” of the AEA.⁶ The original AEC licensing officials commented verbally that FSV was considered by them to be a “research and development reactor that could be shutdown immediately if there were any real safety problems”.⁶

1.3 General Atomics Gas Turbine Modular Helium Reactor (GT-MHR)

Lessons learned at Fort St. Vrain have led more recent reactor designs of the HTGR type to adopt different strategies to confront issues that were previously encountered. For instance, more recent HTGR designs have tended to avoid large per-unit cores in favor of more compact modular units with simpler design. One such design is the Gas Turbine Modular Helium Reactor (GT-MHR) designed by General Atomics. The design is based on the original design of Fort St. Vrain HTGR. It is a helium gas cooled, graphite moderated reactor and uses TRISO fuel compacts in a prismatic core design. It has a power rating of 350 MWt/135 MWe and was designed to meet the need for smaller, simpler nuclear power plants with passive safety characteristics. The GT-MHR was formally selected in 1993 as the reference concept for development by the US gas reactor program for commercial deployment. The experience from the early HTGR plants and related design and development activities provided a solid technology base when gas-cooled reactor development shifted towards smaller, passively safe designs. Although operating experience and past developments are still applicable, the push for safer, highly efficient and economical units, and the need for special applications, has added new requirements that demand and justify further research and development. A more detailed review can be found in a publication by General Atomics, GA-AI91527.

1.4 Other International HTGR Programs

HTGRs have also existed in other countries. For example the United Kingdom’s Dragon reactor, was operated successfully between 1964 and 1975. It was basically an experimental reactor to irradiate a variety of experimental and prototype coated particle fuel as well as to test technological components and structural materials. The full thermal power capacity of the reactor was 20 MWt. At full power, the average core outlet and inlet temperatures were 750 °C and 300 °C, respectively. It used 37 prismatic fuel elements. A more detailed review can be found in the publication by Simon⁸.

Similarly, Germany had a research HTGR program called AVR⁹. The AVR was a pebble bed reactor with capacity of 15 Mwe or 46 MWt. It had a coolant outlet temperature of 950 °C. It started operating from 1967. The plant was short down in 1988 because of serious contamination problems in its primary circuit. The AVR contamination was mainly caused by inadmissible high core temperatures that lead to the instabilities of the fuel particle. A more detail review can be found in the publication of Moorman⁹.

Currently, Japan has an HTGR, operated by Japan Atomic Energy Research institute (JAERI) and under the name of high temperature engineering test reactor (HTTR)¹⁰. This is a research reactor of capacity 30 MW_{th}. The objective of this reactor is to develop and upgrade high temperature gas-cooled reactor technology, and conduct research on high temperature engineering. The reactor reached its first criticality on November 1998. This reactor uses

prismatic fuel with a design coolant outlet temperature of 1000 °C. A more detailed review can be found in the JAERI report.¹⁰

The most recent addition to the HTGR family is the Chinese HTR-10. This is a 10 MWth pebble bed research reactor that reached its criticality in 2002. The design of this reactor is based on the original German AVR design. Based on the experience gained by the demonstration HTR-10, China is currently developing a commercial version named as High Temperature Gas-Cooled Reactor-Pebble bed Module (HTR-PM). The HTR-PM plant will have power of 210 MWe. A more detailed review can be found in the paper by Zhang et al.¹¹

To the best of our knowledge, none of the other nations have a consensus design code that is applicable to HTGR. The KTA and JAEA design codes were in the draft status. The British AGRs, which are not HTGRs, were designed by proprietary code of British Energy (now, EdF-Energy), which is not a consensus design code.

1.5 Current HTGRs in the Context of Generation IV and NGNP Programs

Currently, there are international efforts for developing Generation IV reactor systems. Table 1 summarizes the main characteristics of the planned six generation IV systems.

The Very High Temperature Reactor (VHTR) is a Generation IV reactor concept that uses graphite as a moderator with a once-through uranium fuel cycle. The VHTR represents a modern and highly evolved version of the original HTGR design. A Next Generation Nuclear Plant (NGNP) is a generation IV version of the Very High Temperature Reactor (VHTR) currently under research and development stage in United States.

Table 1 Overview of generation IV systems¹².

System	Neutron spectrum	Coolant	Design Outlet Temp. °C	Fuel cycle	Size (MWe)
VHTR (Very-High-temperature-Reactor)	thermal	Helium gas	900 – 1000*	open	250 - 300
SFR (Sodium-cooled Fast Reactor)	fast	Sodium liquid	550	closed	30 - 150, 300 - 1500, 1000 - 2000
SCWR (Super-critical water cooled reactor)	Thermal/fast	water	510 - 625	Open/closed	300 - 700, 1000 - 1500

Table 1 Overview of generation IV systems¹²

System	Neutron spectrum	Coolant	Design Outlet Temp. °C	Fuel cycle	Size (MWe)
GCFR(Gas-cooled fast reactor)	fast	Helium gas	850	closed	1200
LFR (Lead-cooled fast reactor)	fast	Lead liquid	480 - 800	closed	20 - 180, 300 - 1200, 600 - 1000
MSR (Molten salt reactor)	Fast/thermal	Fluoride liquid salts	700 - 800	closed	1000

* The inlet and outlet coolant temperatures of the current NGNP design are 250 and 700°C, respectively*

1.6 Motivation for This Research Program

Though research work is continuing and a number of HTGR research reactors are currently under operation, a commercial HTGR has not been constructed since the 1980s. While the general characteristics necessary for producing nuclear grade graphite are understood, historical “nuclear” grade graphites no longer exist. In addition, few data are available related to assess the structural integrity of large commercial HTGRs under high fluence, temperature and long duration of operation. For example even after ~60 years of graphite use in reactors, the microstructural mechanisms of irradiation creep and crystal deformation are still being debated and a complete understanding has been elusive¹³

Since the late 1980s, new powerful structural analysis tools have been developed, such as the high performance finite element analysis software packages, as well as analytical microscopy and nondestructive evaluation tools, such as computed x-ray tomography, in examining the graphite structure. These tools can be used to study the individual graphite component behavior as well as the overall structural integrity of the graphite core assembly. Analyses of assembly and component-scale models will allow designers to predict the dimensional distortion, component stresses, residual strength, and the probability of failure during normal and off-normal conditions. The purpose of this research is to develop generic finite element models of the graphite core components and develop procedures for analyzing stresses, strains, deformation and failure of the components based on existing material properties database. Once the procedure is developed, it can be used to analyze any graphite grade component chosen for any particular HTGR design and ensure that the ASME structural design criteria for graphite core components are satisfied.

This specific research activity will assist in developing an independent calculation tool via a structural finite-element analysis (FEA) computer code to determine the stresses in graphite core components of a high-temperature gas cooled reactor (HTGR). This stress analysis capability will provide the tools necessary for the NRC staff to independently verify and confirm

* Communicated by Email from Dr. D. Carlson to Dr. M. Srinivasan, July 19, 2011.

applicants' data, models, and technical bases for ensuring the structural integrity of graphite core components and the operational safety of the HTGR itself.

The current report is divided into the following general headings:

- Literature review of HTGR stress /heat conduction analysis methods
- Review of HTGR graphite core design standards
- Review of graphite core components
- Review and/or development of graphite material properties and material models
- Review of irradiation creep material models
- Proposed stress analysis code and approach

2. LITERATURE REVIEW AND EVALUATION OF HTGR STRESS ANALYSIS/HEAT CONDUCTION METHODS

2.1 Finite Element Stress Analysis Model

The chronology of finite element stress analysis code for HTGR graphite components is discussed in this section. In 1981, after reviewing the earlier data on irradiation-induced creep in graphite, Price¹⁴ suggested that irradiation-induced creep in graphite can be modeled using a linear viscoelastic creep model. The total strain was decomposed into a recoverable transient strain component followed by a steady-state strain component, except that the steady-state creep strain must be treated as a function of the neutron fluence. The total transient creep strain is approximately equal to the preceding elastic strain. No temperature dependence of the transient creep parameters has been demonstrated. In 1983, Smith and Pelessone¹⁵ presented a finite element based method to calculate stresses in graphite fuel elements of a HTGR core. They assumed that graphite under irradiation may be treated as a linear viscoelastic material and idealized with the Maxwell-Kelvin model as shown in Fig. 1.

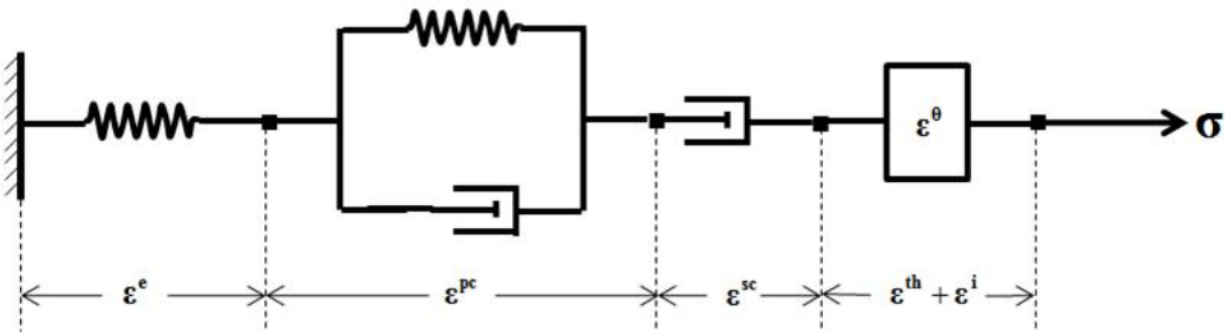


Figure 1. Maxwell-Kelvin Model of Graphite

Smith and Pelessone assumed that the total strain is a linear sum of elastic strain (ϵ^e), steady state creep strain (ϵ^{sc}), transient creep strain (ϵ^{pc}), and combined thermal and irradiation strain (ϵ^θ), which can be expressed as:

$$\epsilon = \epsilon^e + \epsilon^{pc} + \epsilon^{sc} + \epsilon^\theta. \quad (1)$$

Smith and Pelessone idealized the fuel block as a 1-dimensional body and used bar elements to develop the finite element model. From the different strain fields, the combined thermal and irradiation strain (ϵ^θ), was given or known; the strain fields such as elastic strain (ϵ^e), steady state creep strain (ϵ^s), transient creep strain (ϵ^T) are unknown. These unknown strains along with total internal strain and stress are estimated explicitly by solving the equilibrium equation combined with the constitutive relationship. Their work was one of the earliest published works on finite element based stress analysis of HTGR core graphite components.

Later, a standalone finite element code called VIENUS¹⁶ was developed by JAERI in Japan for the analysis of stresses in HTTR graphite blocks. The purpose of this code was to analyze the effects of both fast neutron fluence and temperature on material properties. Since almost all of

the general purpose finite element codes were only able to treat temperature dependence of the material properties and strains, these codes were not suitable for JAERI's stress analysis requirements. Unlike the work of Smith¹⁵, the VIENUS code considered the thermal (ϵ^θ) and irradiation strain (ϵ^i) separately and the corresponding total strain relation is schematically depicted in Fig. 2. Also, the expression for the total strain is given by,

$$\epsilon = \epsilon^e + \epsilon^{pc} + \epsilon^{sc} + \epsilon^\theta + \epsilon^i. \quad (2)$$

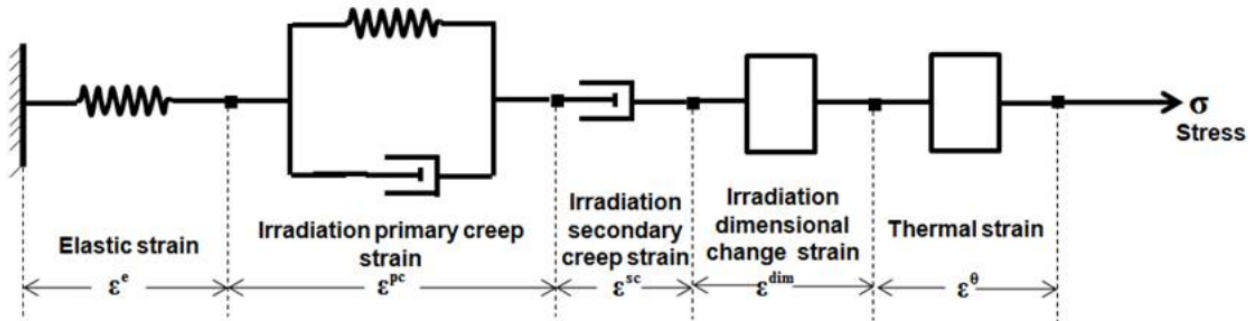


Figure 2. Maxwell-Kelvin Model of Graphite (Iyoku¹⁶).

The VIENUS code is a two-dimensional finite element visco-elastic stress analytical code with a library containing linear and parabolic quadrilateral elements. The temperature input data to the VIENUS code were calculated by the ABAQUS code. The code has been evaluated by the irradiation test results of the Peach Bottom fuel elements to confirm the thermal/irradiation stresses in the graphite block. From this study, the JAERI researcher found that the VIENUS code was able to estimate the trend of the test results, and that both the irradiation induced creep and dimensional change are the most important parameters in the thermal/ irradiation stress analysis. Although more general viscoelastic rheological models consisting of infinite assemblage of Maxwell-Kelvin type elements are theoretically possible, as a practical matter because of a lack of extensive in-reactor mechanical properties data on graphite, the current practice is to use the simple model depicted in Fig. 2.

Later, a material model subroutine called MAN UMAT was developed by an UK research group¹⁷ for analysis of nuclear graphite under fast neutron irradiation and radiolytic oxidation conditions. The subroutine was developed together with the ABAQUS finite element program to perform three-dimensional, time-integrated, non-linear irradiated graphite stress analyses. Based on this code, Li, Marsden and Fok¹⁸ presented stress analysis results for a hypothetical cylindrical graphite moderator block, considering dimensional and other property changes due to fast neutron irradiation. Applying symmetric conditions, only one eighth of the block was selected for calculation. Three-dimensional eight-node elements were used in this particular analysis. For simplicity, the temperature was assumed to be uniform throughout the whole block at 500°C throughout reactor life. But the fast neutron dose was assumed to have a radial profile, i.e. decreasing with increasing radius, and to be uniform along the length of the block. It was assumed that the dose increased linearly with time. The model simulated a period of 30 years operation with a shutdown every 2.5 years.

Further development of the ABAQUS-based three-dimensional MAN UMAT code was presented by Tsang and Marsden¹⁹ in 2006. The irradiated graphite material properties were implemented into the ABAQUS finite element code using a user-defined material subroutine (UMAT). At the beginning of each increment, the finite element calculation scheme estimates the total strain within the model. There are two functions performed by the UMAT subroutine. Firstly, it updates the stresses to their values at the end of the increment from the estimated total strain. Secondly, it provides the graphite material Jacobian matrix for the mechanical constitutive model. The total strain within the model is considered as the sum of seven different strain components, as:

$$\varepsilon = \varepsilon^e + \varepsilon^{pc} + \varepsilon^{sc} + \varepsilon^\theta + \varepsilon^{dc} + \varepsilon^{i\theta} + \varepsilon^{idc}, \quad (3)$$

where, the additional terms $\varepsilon^{i\theta}$ and ε^{idc} represent interaction thermal and dimensional change strain, respectively. These two interaction terms were assumed to be functions of irradiation creep. If interaction strain terms are not included in the analysis, all the strain can be calculated explicitly. However, the interaction terms are implicit functions of the total creep strain. Hence, a predictor-corrector approach was used to evaluate the interaction strains. For numerical study, they considered a simple three-dimensional model depicting a hypothetical graphite moderator block. The model represents one-eighth of a half-height graphite moderator block used in a hypothetical reactor design. To perform the stress analysis they considered four field variables such as irradiation fluence, irradiation temperature, weight loss, and radiolytic oxidation rate. Simpler field variable profiles are assumed, for example all field variables vary in radial direction but are uniform along the circumferential direction and the height of the block. It is assumed that the maximum and minimum values for these field variables occur at the internal radius and external radius, respectively. Both irradiation fluence and weight loss are assumed to vary linearly with time whereas the temperature and the oxidation rate are assumed to remain constant through the whole reactor life. Before reactor start-up and after shut-down the block was assumed to be at a uniform ambient temperature.

In recent years, significant HTGR core stress analysis activities have taken place in France. Lejeail and Cabrilat²⁰ calculated the temperature and thermal stress distributions in an HTGR core graphite block parametrically, taking into account the effect of fluence on thermal and mechanical properties. The finite element model was based on an earlier developed Cast3M CEA code²¹ developed by Verpeaux, et al. The paper presented results for a realistic geometry, though two-dimensional. However, it did not include information on theoretical basis of the Cast3M CEA code. One twelfth of a graphite fuel block was modeled in Cast3M code. Each assembly contains 216 fuel elements of 12.5 mm diameter, and 108 coolant channels of 16 mm diameter.

In addition to calculations conducted with FEA by countries with prior HTGR experience, significant amount of research on HTGR graphite core modeling and stress analysis are being conducted in China. Based on the earlier work of Tsang and Marsden¹⁹, Wang and Wu²² have presented an implicit finite element model with application to Chinese HTR program. The stress analysis and evaluation of graphite components are carried out using a three-dimensional finite element code named INET-GRA3D. The code is based on user subroutines specifically developed for the commercial software MSC.MARC and takes into account the irradiation-induced dimensional and material property changes and irradiation creep. Relationships for irradiated Young's modulus, coefficient of thermal expansion, coefficient of thermal conductivity and the secondary creep coefficient are defined in user subroutines and vary as functions of temperature and cumulative dose.

Recently, Idaho National Laboratory²³ presented a report on modeling the mechanical behavior of prismatic reflector block. This report outlines the development of finite element models used to determine temperature and stresses in a H-451 graphite prismatic core reflector block. A commercially available multi-physics finite element software COMSOL was used to conduct a fully-coupled thermal fluid and structural analysis. For numerical calculations, they considered a two-dimensional model of an outer reflector block. The analysis was performed considering thermal and fast fluence gradient in the radial direction at the interface of the fuel ring and an outer control rod blocks.

2.2 Analytical Stress Analysis Models

With the advent of modern finite element analysis tools, structures with complex and interacting geometry and exhibiting complex material mechanisms have been modeled. Often, the finite element based codes are revised based on operational experience and/or new material test data. However, to validate the results computed by finite element codes independently, either experimental results or results obtained by independent analytical models are required. For HTGR application, few experimental results are currently available, especially for the newer graphite classes. The acquisition of long duration (30-60 years) structural degradation data from experiments or from operational experience is highly unlikely at present. Hence, it is necessary to validate the complex FE codes with results from analytical models. Though analytical models are not practically possible for each geometry, for simpler geometries, analytical models are either available or can be formulated. The results of these simpler models can be used to validate the finite element procedure followed for any stress analysis application. Also, analytical models provide a quick way of estimating the stresses in a graphite component with a changing operational requirement. Marsden et al.²⁴ and Li et al.²⁵ have presented an analytical model for a graphite moderator block of simplified geometry, and considered the dimensional change and other property changes due to fast neutron irradiation. They assumed a simplified long and hollow cylindrical geometry for the moderator block. The three-dimensional stress fields (in polar coordinates) for the proposed simplified model are given in Eqs 4a-c.

$$\sigma_{rr} = \frac{E}{1-\nu} \exp[(-0.23E / E_c)\gamma] \int_0^{g=\gamma} \exp[(-0.23E / E_c)g] d[\zeta_1(g)] \quad (4a)$$

$$\sigma_{\theta\theta} = \frac{E}{1-\nu} \exp[(-0.23E / E_c)\gamma] \int_0^{g=\gamma} \exp[(-0.23E / E_c)g] d[\zeta_2(g)] \quad (4b)$$

$$\sigma_{zz} = \frac{E}{1-\nu} \exp[(-0.23E / E_c)\gamma] \int_0^{g=\gamma} \exp[(-0.23E / E_c)g] d[\zeta_3(g)] \quad (4c)$$

where σ_{rr} , $\sigma_{\theta\theta}$, and σ_{zz} are radial, hoop and axial stresses, respectively. E and E_c are dynamic Young's modulus and creep Young's modulus, respectively, and ν is Poisson's ratio, all of which are functions of the neutron fluence γ .

$$\zeta_1 = \frac{1}{r^2} \frac{r^2 - a^2}{b^2 - a^2} \int_a^b \varepsilon^d r dr - \frac{1}{r^2} \int_a^r \varepsilon^d r dr \quad (5a)$$

$$\zeta_2 = \frac{1}{r^2} \frac{r^2 + a^2}{b^2 - a^2} \int_a^b \varepsilon^d r dr + \frac{1}{r^2} \int_a^r \varepsilon^d r dr - \varepsilon^d \quad (5b)$$

$$\epsilon_3 = \frac{2}{b^2 - a^2} \int_a^b \epsilon^d r dr - \epsilon^d \quad (5c)$$

where ϵ^d is fluence-dependent dimensional change strain, a and b are inner and outer radius, respectively, and r is radial coordinate.

2.3 Analytical Heat Conduction Model

An analytical solution for a steady-state heat conduction in a heat-generating circular region cooled by uniformly spaced ring of equal holes (Fig. 3) was presented by Rowley and Payne²⁶. The basic equations for the problem are as follows:

$$\nabla^2 T(r, \theta) = -q/k \quad (6)$$

where q is the heat generation rate constant and k is thermal conductivity. For convective cooling at the holes and insulated outer surface, Eq. 6 is subjected to the boundary conditions

$$\frac{\partial T}{\partial r} = 0 \text{ at } r = r_o \quad (7a)$$

$$k \frac{\partial T}{\partial \rho} = bh(T - T_b) \text{ at } \rho = \lambda \quad (7b)$$

Also, using $q=0$ in Eq. 6, and

$$T = T_o \text{ at } r = r_o \quad (8a)$$

$$T = 0 \text{ at } \rho = \lambda \quad (8b)$$

the conductance or shape factor for the region is obtained. The two boundary value problems were solved numerically using harmonic series and the results were presented graphically for temperature distribution in a non-dimensional form for various number (m) of holes and other geometric parameters.

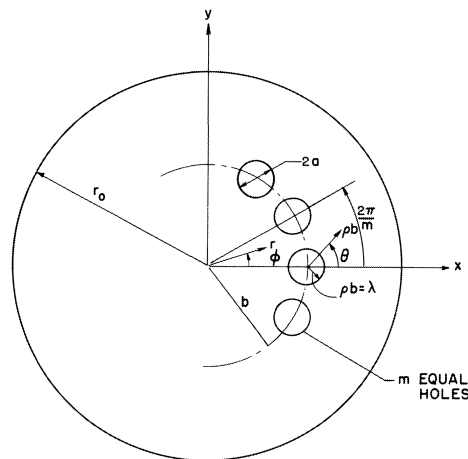


Figure 3. Cross-section of a cylinder with uniformly spaced m number of cooling holes.

3. REVIEW OF HTGR GRAPHITE CORE DESIGN STANDARDS

In this chapter we review and evaluate the various design codes which have been used by the gas cooled reactor designers and the current status of the ASME draft code case. The results from the stress-strain analysis of graphite core components have to satisfy the ASME code or some other code rules for nuclear design applications. The metallic reactor component design criteria as described in Section III, subsection NH of the ASME Boiler and Pressure Vessel (BPV) Code cannot be applied. This code is based on deterministic calculation and is suitable for ductile metallic materials. Current computation techniques such as finite element tools used to model the stress states in metallic components have shown excellent predictive capabilities. However, the current state-of-the-art modeling capabilities for graphite materials do not permit stress predictions to the same accuracy as metallic components. Therefore, the use of deterministic methods to predict safety margins in graphite component stress states is considered unreliable.²⁷ Currently, Subsection NH of the ASME Code rules do not adequately cover the stress analysis of High Temperature Gas Cooled Reactor (HTGRs) components. Design criteria for HTGR graphite core components are contained in the draft 2011 edition of the ASME code²⁸ and published JAEA report²⁹. Highlights of both design criteria are summarized in Sections 3.1 and 3.2.

3.1 ASME Code, Section III, Division 5, Subsection HH²⁸

3.1.1 Classification of Graphite Core Components (HHA-3111 and 3112).

Graphite core components shall be assigned to one of the following Structural Reliability Classes in the Design Specification:

- (a) SRC-1: The structural reliability of components in this class is important to safety. These parts may be subject to environmental degradation;
- (b) SRC-2: The structural reliability of components in this class is not important to safety. These parts are subject to environmental degradation during life;
- (c) SRC-3: The structural reliability of components in this class is not important to safety. These parts are not subject to environmental degradation during life.

Enveloping Graphite Core Components: A graphite core assembly may consist of many hundreds of graphite core components. These graphite core components may have minor geometric differences and be exposed to variations in loading. It is acceptable to subdivide the graphite core assembly into groups of components and then to assess graphite core components that see the highest utilization. The responsibility for identifying and justifying the enveloping graphite core components is allocated to the designer.

3.1.2 Loadings (HHA-3122)

The following fourteen loadings that shall be taken into account in designing the graphite core components include, but are not limited to, those in (a) to (n) below.

- (a) Pressure differences due to coolant flow;
- (b) Weight of the core components and fuel;
- (c) Superimposed loads such as those due to other structures, the reactor core, flow distributors and baffles, thermal shields, and safety equipment;
- (d) Earthquake loads or other loads that result from motion of the reactor vessel;
- (e) Reactions from supports, restraints, or both;
- (f) Loads due to temperature effects, thermal gradients and differential expansion of the graphite core assembly, or any combination thereof;
- (g) Loads resulting from the impingement or flow of reactor coolant, or other contained or surrounding fluids or gases;
- (h) Transient pressure difference loads, such as those that result from rupture of the main coolant pipe;
- (i) Vibratory loads;
- (j) Loads resulting from operation of machinery such as snubbing of control rods;
- (k) Handling loads experienced in preparation for or during refuelling or in service inspection;
- (l) Internal loads such as those resulting from thermal stresses or irradiation induced stresses resulting from temperature and flux/fluence distribution within a graphite core component;
- (m) Loading due to instabilities caused by component distortion (such as bowing of graphite columns);
- (n) Assembly loads and loading during construction.

3.1.3 Terms Relating to Design and Service Loading (HHA-3124)

The following five loading categories are defined in the ASME Code

- (a) **Design Loadings:** The Design Loadings are the distributions of pressure, temperature, fast neutron flux or damage dose and dose rate, and various forces applicable to Graphite Core Components as defined in the following subparagraphs. These are defined as the enveloping Service Level A Loadings for the Graphite Core Component in the core.
- (b) **Level A Service Loading:** These include loads resulting from system start-up, power range operation, fueling, refueling, and system shutdown. This corresponds to normal operating condition.
- (c) **Level B Service Loadings:** These are loads that are anticipated to occur with a moderate recurrence frequency. The design shall provide the capability to withstand these loads without operational impairment. The Level B Plant Operating Condition includes the Operating Basis Earthquake (OBE) load and loads resulting from unscheduled events such as operator error, equipment failure, etc. This corresponds to abnormal operating condition.

- (d) **Level C Service Loadings:** These include events and resulting loads that occur with a low probability. Level C Plant Operating Condition may result in situations that require immediate corrective actions or orderly shutdown of the plant and localized damage to the system requiring repair. This corresponds to emergency condition.
- (e) **Level D Service Loadings:** These include events and resulting loads that have a very low probability of occurring. The component may be damaged, requiring repair or replacement. This corresponds to broken down condition.

3.1.4 Terms Related to Stress Analysis (HHA-3214)

- (a) **Primary stress** is any normal stress or a shear stress developed by an imposed loading that is necessary to satisfy the laws of equilibrium of external and internal forces and moments. The basic characteristic of a primary stress is that it is not self-limiting. Primary stresses that considerably exceed the material strength will result in failure. A thermal stress is not classified as a primary stress.
- (b) **Secondary stress** is a normal stress or a shear stress developed by the constraint of adjacent material or by self constraint of the structure. The basic characteristic of a secondary stress is that it is self-limiting.
- (c) **Combined stress** is the combination of primary and secondary stress. Due to the brittle nature of graphite, no distinction is made between primary and secondary stresses for the purpose of assessment to these rules.
- (d) **Peak stress** is that increment of stress that is additive to the combined stresses by reason of local discontinuities or local thermal stress. This includes the effect of stress concentrations. The basic characteristic of a peak stress is that it does not cause any noticeable distortion and is objectionable only as a possible source of a fatigue crack or a brittle fracture. Due to the brittle nature of graphite, it is important that peak stresses are considered explicitly when assessing the compliance of a Graphite Core Component to these rules.
- (e) **Equivalent stress** is computed using a Maximum Deformation Energy (MDE) criterion. The equivalent stress (σ_v) at a point within a graphite structure shall be calculated as follows:

$$\sigma_v = \sqrt{\bar{\sigma}_1^2 + \bar{\sigma}_2^2 + \bar{\sigma}_3^2 - 2\nu(\bar{\sigma}_1\bar{\sigma}_2 + \bar{\sigma}_1\bar{\sigma}_3 + \bar{\sigma}_2\bar{\sigma}_3)} , \quad (9a)$$

where:

$$\bar{\sigma}_i = f\sigma_i \quad (9b)$$

$$f = \begin{cases} 1 & \text{if } \sigma_i (i = 1, 2, 3) \text{ is tensile} \\ R_{ic} & \text{if } \sigma_i (i = 1, 2, 3) \text{ is compressive} \end{cases}$$

R_{ic} is the ratio between the mean tensile and compressive strength for the specific grade of graphite.

The assessment of graphite core components is based on peak equivalent stress.

3.1.5 Irradiation Fluence Limits (HHA-3142.1)

The following three fluence categories are defined in the ASME intermediate Code. Graphite components in a core are classified according to their cumulative fast ($E > 0.1$ MeV) neutron irradiation fluence.

- (a) For fluence (at any point in the component) < 0.001 dpa ($0.7 \times 10^{18}/\text{cm}^2$ (EDN)), the effects of neutron irradiation are negligible and may be ignored.
- (b) For fluence (at any point in the component) > 0.001 dpa ($0.7 \times 10^{18}/\text{cm}^2$ (EDN)), the effect of neutron irradiation on thermal conductivity shall be taken into account.
- (c) For fluence (at any point in the component) > 0.25 dpa ($2 \times 10^{20}/\text{cm}^2$ (EDN)), all effects of neutron irradiation shall be considered and a viscoelastic analysis applied.

For the purpose of code assessment, the graphite core components are considered irradiated. Use of materials within the core shall be limited by the range of temperature and fast neutron damage dose over which the material is characterized.

3.1.6 Stress Limits for Graphite Core Components (HHA-3220, 3230, 3240)

Rules for the design of graphite core components and graphite core assemblies are to be followed for three alternative approaches to the design. These are:

- (a) **Simplified assessment:** Design of Graphite Core Components to meet the reliability targets based on stress limits derived from the material reliability curve. This is referred to as a simplified assessment.
- (b) **Full assessment:** Design of Graphite Core Components to meet the reliability targets based on calculated reliability values derived from the distribution of stresses in the Graphite Core Components and the material reliability curve. This is referred to as Full Assessment.
- (c) **Design by test:** Design of Graphite Core Components to meet the reliability targets based on experimental proof of Graphite Core Component performance with margins derived from the Material reliability curve. This is referred to as design by test. Note that not all parts and loadings may be suitable to design by test as complex loadings and environmental effects may not be adequately reproducible in a test.

In all of the above cases, the design approach selected is semi-probabilistic, based on the variability in the experimentally observed strength data of the graphite grade. Due to the nature of the material, it is not possible to ensure absolute reliability, expressed as an absence of cracks, of graphite core components. This is reflected in the setting of probability of failure targets. For all of the above cases, the design allowable probabilities of failure are give in Table 2.

Table 2. Design allowable probability of failure

SRC	Design	Service Level			
		A	B	C	D
SRC-1	10^{-4}	10^{-4}	10^{-4}	10^{-4}	10^{-3}
SRC-2 ^(a)	10^{-4} (10^{-2})	10^{-4} (10^{-2})	10^{-4} (10^{-2})	5×10^{-2}	5×10^{-2}
SRC-3	10^{-2}	10^{-2}	10^{-2}	5×10^{-2}	5×10^{-2}

^(a) Allowance for degradation due to irradiation effects

Also note that due to the complex nature of the loadings of graphite components in a reactor, combined with the possibility of disparate failures of material due to undetectable manufacturing

defects, the probability of failure values used as design targets may not be precisely accurate predictions of the rate of cracking of components in service. The designer is required to evaluate the effects of cracking of individual graphite core components in the course of the design of the graphite core assembly and ensure that the assembly is damage tolerant.

3.1.7 Material Properties Requirements for Design (Mandatory Appendix HHA-II-2000)

Graphite properties used for design shall be determined by the designer and published in the Material Data Sheet. Tables 3-8 are the mandatory data sheet to be provided by the designer in the following subcategories. Because many mechanical properties change significantly with temperature and neutron fluence, it is essential to have all the material properties available as functions of temperature and neutron fluence in order to carry out a full design life evaluation.

3.1.7.1 As-Manufactured Material Properties

Table 3. Grade designation. Numbers within parentheses denote sequence numbers of properties.

Material Grade	(1)	Material Spec. ID	(2)	ASTM Spec.	(3)	Max Grain Size (mm)	(4)
Designation	(5)						

Table 4. Temperature-dependent properties. Numbers within parentheses denote sequence numbers of properties.

Property	Units	Orientation	20 °C	200 °C	400 °C	600 °C	800 °C	1000 °C
Bulk density	kg-m ⁻³	(6)						
Tensile strength	MPa	(7)						
Flexural Strength (4-point bend)	MPa	(8)						
Compressive strength	MPa	(9)						
Elastic modulus (dynamic)	GPa	(10)						

Table 4. Temperature-dependent properties. Numbers within parentheses denote sequence numbers of properties.

Property	Units	Orientation	20 °C	200 °C	400 °C	600 °C	800 °C	1000 °C
Elastic modulus (static)	GPa	(11)						
Coefficient of thermal expansion	°C ⁻¹	(12)						
Thermal Conductivity	W/m-K	(13)						

Table 5. Temperature-independent properties. Numbers within parentheses denote sequence numbers of properties.

Poisson's ratio	(14)	Anisotropy factor	(15)	Critical Stress Intensity Factor K_{IC} , MPa.m ^{1/2}	(16)
-----------------	------	-------------------	------	--	------

Table 6. Design strength values. Numbers within parentheses denote sequence numbers of properties.

Ratio of compressive to tensile strength (R_{tc})	(17)	Ratio of flexural to tensile strength (R_{tf})	(18)	S_c (95%) MPa	(19)	m (95%)	(20)
		S_o (95%) MPa	(21)	S_{co} (95%) MPa		m_o (95%)	(23)
S_g (10 ⁻⁴) MPa	(24)	S_g (10 ⁻³) MPa	(25)	S_g (10 ⁻²) MPa		S_g (5 x 10 ⁻²) MPa	(27)

3.1.7.2 Irradiated Material Properties

Table 7. Irradiated material properties. Numbers within parentheses denote sequence numbers of properties.

Property	Unit	With grain (wg)	Against grain (ag)
Dimensional change	(28)		
Creep coefficient	(29)		
Coefficient of thermal expansion	(30)		
Strength	(31)		
Elastic modulus	(32)		
Thermal conductivity	(33)		

3.1.7.3 Oxidized Condition Material Properties

Table 8, List of oxidized condition material properties.

Property	Unit	2%	4%	6%	8%	10%
Strength	(34)					
Elastic modulus (dynamic)	(35)					
Thermal conductivity	(36)					

3.2 Japanese (JAEA) Code for HTGR Graphite Core Components

3.2.1 Graphite Component Class Terminology

- (a) **Graphite class A** is graphite components whose damage might lead directly to collapse of a reactor core or loss of safety features (control rod insertion and cooling of reactor core), and is not replaced in principle during a reactor lifetime and its damage influences on the reactor lifetime directly.

- (b) **Graphite class B** is graphite components other than the graphite component Class A, whose damage might lead indirectly to collapse of a reactor core or loss of safety features (failure of fuels etc.)
- (c) **Graphite class C** is graphite component other than the graphite component classes A and B

3.2.2 JAEA Design Limits

The stress limits etc. shall be determined by deterministic evaluation principle. Alternatively, it is possible to determine them by probabilistic evaluation with an appropriate fracture probability. The evaluation results of graphite components shall meet the requirements of the stress limit and fatigue limit taking into account irradiation, oxidation effects etc. for the each service condition of reactor. The probabilistic evaluation limits are not described in the JAEA code. However, the deterministic stress and fatigue limits are described in the JAEA code and summarized as follows.

3.2.2.1 Stress Limits

(a) Stress Limits of Service Conditions A and B

The principal stress produced in service conditions A and B shall satisfy the following limits of 1), 2) and 3).

- 1) $P_m + Q_m \leq S_m$
- 2) $P_p + Q_p \leq S_p$
- 3) $P_p + Q_p + F \leq S_F$

Where

P_m : Primary membrane stress

Q_m : Secondary membrane stress

P_b : Primary bending stress

Q_b : Secondary bending stress

P_p : Primary point stress ($P_m + P_b$)

Q_p : Secondary bending stress ($Q_m + Q_b$)

F : Peak stress

S_m : Allowable stress limit to the membrane stress (Primary + secondary) corresponding to 1/4 of the specified minimum ultimate strength

S_p : Allowable stress limit to the sum of membrane and bending stress or to point stress (Primary + secondary) corresponding to 1/3 of the specified minimum ultimate strength

S_F : Allowable stress limit to the total stress corresponding to 9/10 of the specified minimum ultimate strength

(b) Stress Limits of Service Condition C

The principal stress produced in service conditions C shall satisfy the following limits of 1), 2) and 3).

1) $P_m + Q_m \leq 2 S_m$

2) $P_p + Q_p \leq 2 S_p$

3) $P_p + Q_p + F \leq S_F$

(c) Stress Limits of Service Condition D

The principal stress produced in service conditions D shall satisfy the following limits of 1), 2) and 3).

1) $P_m + Q_m \leq 2.4 S_m$

2) $P_p + Q_p \leq 2.4 S_p$

3) $P_p + Q_p + F \leq 1.1 S_F$

3.2.2.2 Fatigue limits

The principal stress produced in each operational condition shall satisfy the following limits of 1), 2), and 3).

1) Limits of Service Conditions A and B

The cumulative fatigue life usage fraction including service conditions A and B shall satisfy the following limit

$$\sum_i \frac{n_i}{N_i} \leq \frac{1}{3}$$

where

n_i : The number of repetition times for various kinds of stress cycle considered in a design during the lifetime of component

N_i : The number of allowable repetition times evaluated from the design fatigue curve for the sets of maximum stress (σ_{max}) and minimum stress (σ_{min}) for various stress cycle.

2) Limits of Service Conditions A, B and C

The cumulative fatigue life usage fraction including service conditions A, B and C shall satisfy the following limit.

$$\sum_i \frac{n_i}{N_i} \leq \frac{2}{3}$$

(3) **Limits of Service Conditions A, B, C and D**

The cumulative fatigue life usage fraction including service conditions A, B, C and D shall satisfy the following limit.

$$\sum_i \frac{n_i}{N_i} \leq 1$$

4. REVIEW OF GRAPHITE CORE COMPONENTS

4.1 Candidate Graphite Grade Options for HTGR\NGNP Program

The stress analysis code has to be developed using the material properties of a representative graphite grade selected for NGNP program. A detailed review of the candidate graphite grades for NGNP program can be found in an Idaho National Laboratory report.³⁰ The grades presently being considered within the NGNP Advanced Graphite Development Program is given in Table 9. Mechanical properties for some of the graphite grades are currently being investigated and not yet available.

Table 9. Possible graphite grade for HTGR\NGNP program.³⁰

Grade	Supplier	Forming Method	Coke Type	Application
Recommended grades				
NBG-17	SGL Carbon	Vibration molded	Pitch coke	Prismatic fuel & reflector
NBG-18*	SGL Carbon	Vibration molded	Pitch coke	Pebbel bed reflector
PCEA*	Graitech	Extruded	Petroleum coke	Prismatic fuel & reflector
PGX	Graitech	Extruded	Petroleum coke	Prismatic permanent reflector
2020	Carbon Mersel	Isostatically-molded	Petroleum coke	Prismatic fuel & core supports
2114	Carbon Lorraine	Isostatically-molded	Pitch coke	Core support
IG-430	Toyo Tanso	Isostatically-molded	Pitch coke	Prismatic fuel & core supports
Other grades considered				
H-451(Historical grade)	Great Lakes	Extruded	Petroleum coke	Provides a basis for
IG-110	Toyo Transo	Isostatically-molded	Petroleum coke	HTTR (Japan),
NBG-10	SGL Carbon	Extruded	Pitch coke	Replaced by NBG-18
NBG-25	SGL Carbon	Isostatically-molded	Petroleum coke	Core support
HLM	SGL Carbon	Extruded	Petroleum coke	FSV (US) permanent

* Major grades; primary reference for pebble bed (NBG-18) and prismatic (PCEA) reactors.

Table 9. Possible graphite grade for HTGR\INGNP program. ³⁰

Grade	Supplier	Forming Method	Coke Type	Application
PPEA	Graftech	Extruded	Pitch coke	Pebble bed reflector
PCIB	Graftech	Isostatically-molded	Pitch coke	Core support

4.2. Ideal Requirements for HTGR Graphite Grade

Before selecting a graphite grade for HTGR core components, it is necessary to determine the limits for critical graphite properties. Table 10 shows the material properties limits most relevant for ideal nuclear reflector graphite. These requirements are based on previous experience gained in the manufacture and application of nuclear grade graphites for reactor core internals, as well as more recent developments in nuclear graphite technology. ³⁰

Table 10. Ideal graphite grade requirements for HTGR\INGNP program. ³⁰

Property	Required Range	Reason	Performance attributes
Density	1.7 - 1.9 g/cm ³	High density is indicative of lower porosity, provides for more effective neutron moderation/reflection per unit volume, and in general, also indicates higher strength	Neutron efficiency Structural integrity
Neutron absorption cross-section	< 5 mbarn	Required for neutron efficiency of the core. The limiting neutron absorber is that of pure carbon (~3.5 mbarn)	Neutron efficiency
Thermal conductivity at room temperature	> 100 W/m-K	Indicative of a high degree of graphitization and typically the level required for effective heat transfer in HTGR applications	Heat transport
Purity (total ash content)	< 300 ppm	Required to minimize and reduce susceptibility to catalytic oxidation.	Component activity levels during replacement and/or disposal. Graphite Oxidation under normal and accident conditions

Table 10. Ideal graphite grade requirements for HTGR\INGNP program.³⁰

Property	Required Range	Reason	Performance attributes
Tensile strength	> 15 MPa (tensile)	Adequate strength is required for structural component integrity. The strength reserves offered by the material must exceed the allowable operating component stresses. Higher strengths are achievable with isostatic-molded, fine grain graphite, but these typically possess lower fracture toughness. This is a trade-off that must be taken into account in the design.	Structural integrity
CTE (20 to 500°C)	3.5 to 5.5 $\times 10^{-6} K^{-1}$	A higher value is indicative of the coke isotropy and hence isotropy of the graphite. This implies that the graphite will have better dimensional stability when subjected to fast neutron irradiation. However, lower CTE can be beneficial in terms of thermal stress.	Structural integrity
CTE isotropy ratio	< 1.10	Indicative of the bulk graphite isotropy.	Structural integrity
Dynamic elastic modulus	8 to 15 GPa	Higher modulus is typically associated with a higher strength material, but increased sensitivity to thermal stresses. Thus, values at the lower end tend to be more beneficial.	Structural integrity
Dimensional changes with irradiation	Minimal shrinkage over the applicable fluence range and minimal differences in the with-grain and against-grain directions	This is mainly a function of temperature and fluence, but is strongly dependent on the graphite grade. Dimensional changes strongly influence the level of internal stresses generated in core components when subjected to fast neutron irradiation and are critical in determining their useful life.	Structural integrity

4.3 Typical Graphite Core Geometry and Dimensions

To develop the graphite core stress analysis code it is necessary to choose a representative geometry. The present section briefly describes GT-MHR reactor core and typical reflector and

fuel block dimensions.³¹ The graphite core of the GT-MHR is a circular cylinder composed of 102 columns each containing 10 blocks. The cylinder is arranged in 11 circular rings as shown in Fig. 4. The inner reflector uses the first five rings; the active core uses rings 6, 7, and 8; the outer reflector is composed of rings 9 and 10; and ring 11 is the permanent outer reflector.

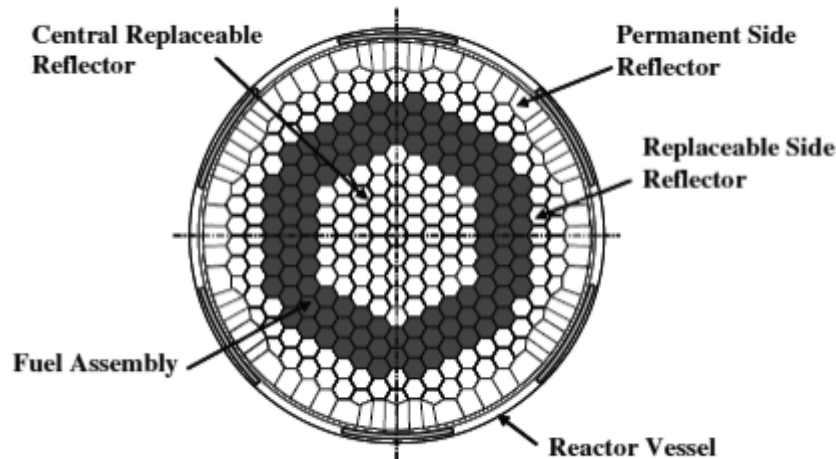


Figure 4. Core arrangement of GT-MHR. ²³

Each block has four dowel pins protruding from the top and each block has four dowel pinholes in the bottom. These dowel pins lock the column together. The thermal expansion and flow induced motion in each block creates shear stresses on the pins and reactive stresses in the dowel pinholes. A standard block is hexagonal in shape with a dimension of 0.36 m across the flat and height of 0.8 m. The dimension of a typical reflector and fuel block can be seen from Figs. 5 and 6, respectively.

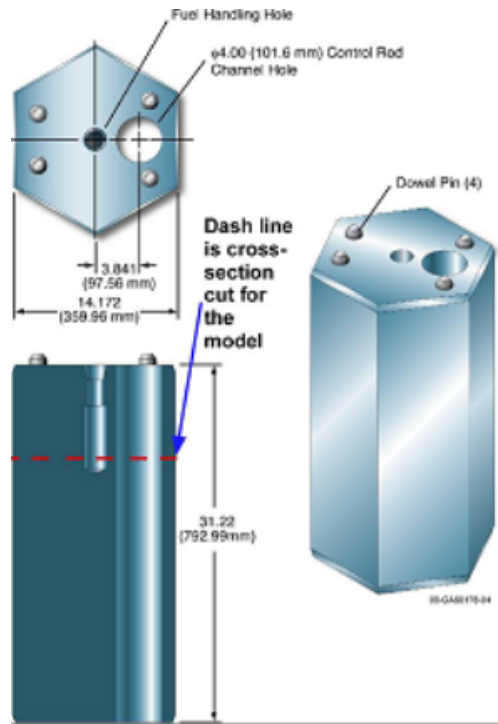


Figure 5. Dimensions of a typical outer reflector block.²³

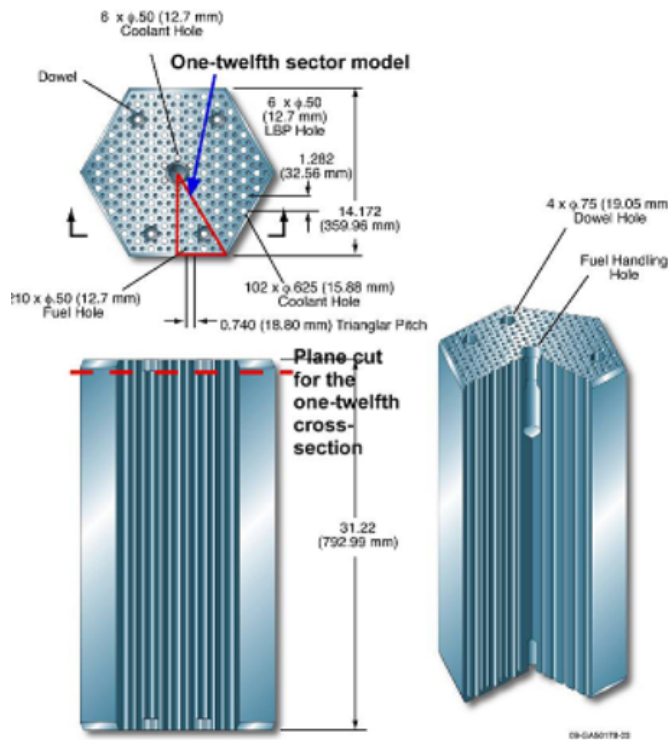


Figure 6. Typical prismatic fuel element dimensions.²³

4.4 Preliminary Neutronics Information for Stress Analysis

In order to conduct HTGR graphite core component stress analysis, we need the fast neutron (> 0.1-0.2 MeV) fluence- and temperature-dependent material properties obtained from experimental results. The available literature experimental data have to be compiled. Typically, the source data are incomplete; either full data are available for only low fluences and temperatures or only few material properties data are available for high fluences and temperatures. To avoid inconsistencies, it is useful to know the fluence distribution inside a typical HTGR core and then decide which portion of the core can be analyzed with the available graphite material properties. The present section presents the preliminary fluence information inside a typical GT-MHR core. Figure 7 shows 1/6th of the core section. As seen in Fig. 7, there are different rings that contains either reflector blocks or fuel blocks. Using the reported³² neutronics information, the fluence at different rings can be estimated. This fluence information with respect to number of years can be used as a field variable in the stress analysis code. Figure 8 shows the overlapping plot of neutron flux with respect to neutron energy at various rings. The reported ³² neutron energy flux spectra, calculated for the initial core with the fuel at a uniform temperature of 1100 °C and the graphite at 927 °C, represent only a small portion of the core and reflector volume. These temperature conditions would be typical at full-power conditions near or just below the core mid-plane. Actual graphite irradiation temperatures may vary from ~260°C near the top to ~1100°C near the bottom. Figure 9 shows the spatial distribution of fast neutron flux magnitudes near the core midplane for neutrons of energy >0.18 MeV. Based on the neutron flux information and assuming a linear variation with time, the fluence values at different rings are estimated for 45 years. Figure 10 shows the estimated fluence values at different rings for around 45 years. Based on this fluence distribution information and available material properties the stress analysis model will be developed.

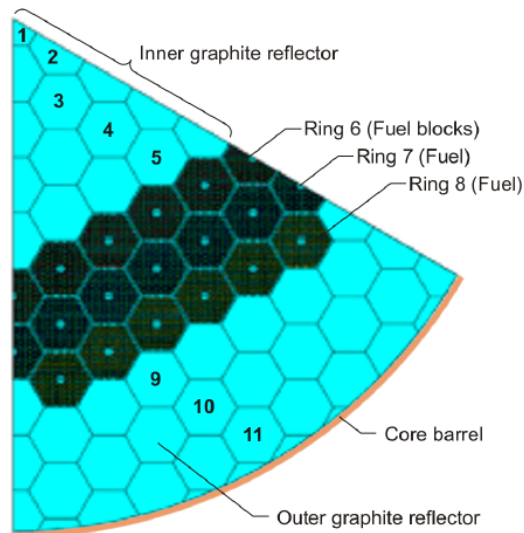


Figure 7. 1/6th of core section³²

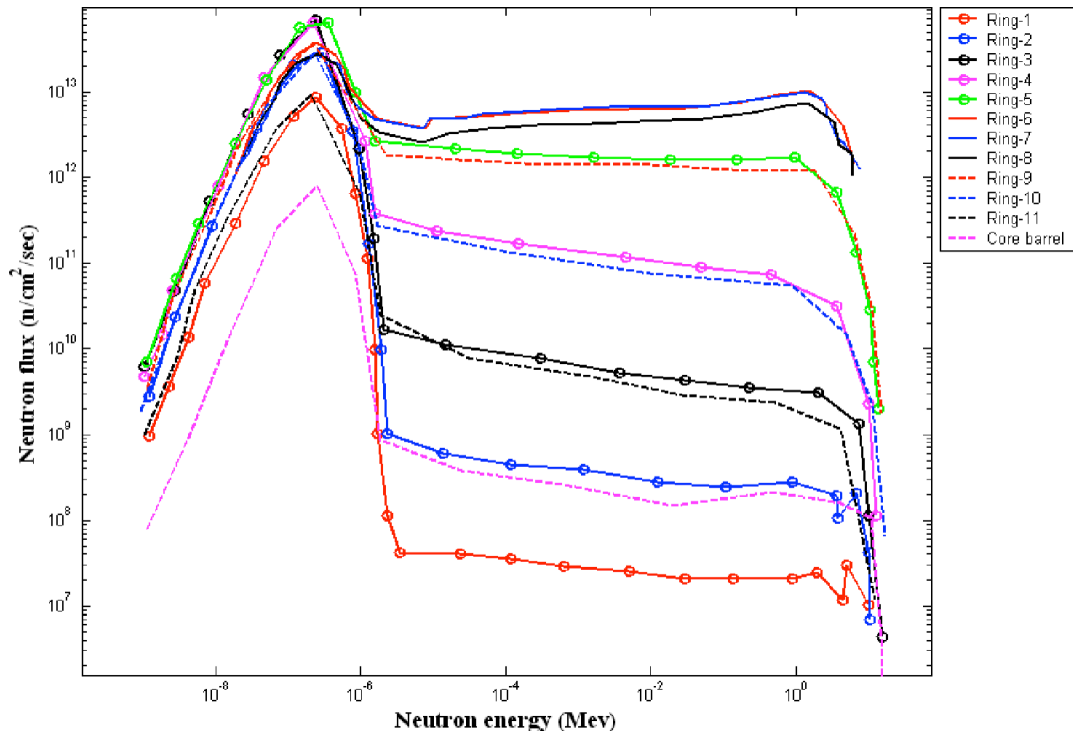


Figure 8. Fast neutron flux near core mid plane or maximum core fluxes.³²

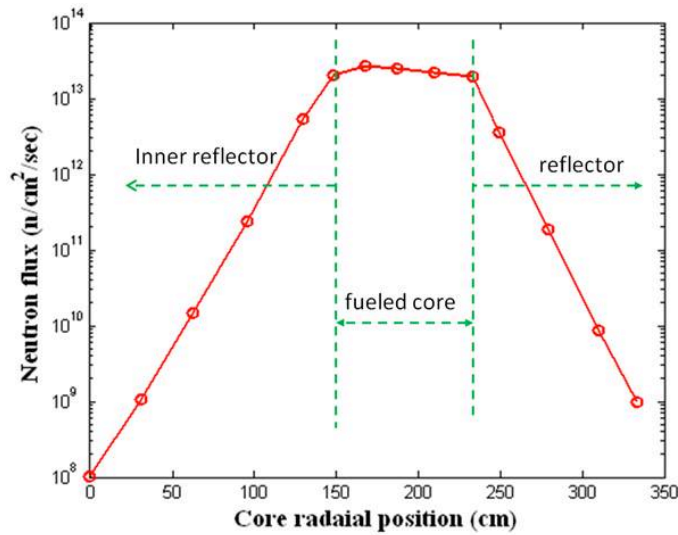


Figure 9. Fast neutron flux near core mid plane for neutrons of energy >0.18 MeV.³²

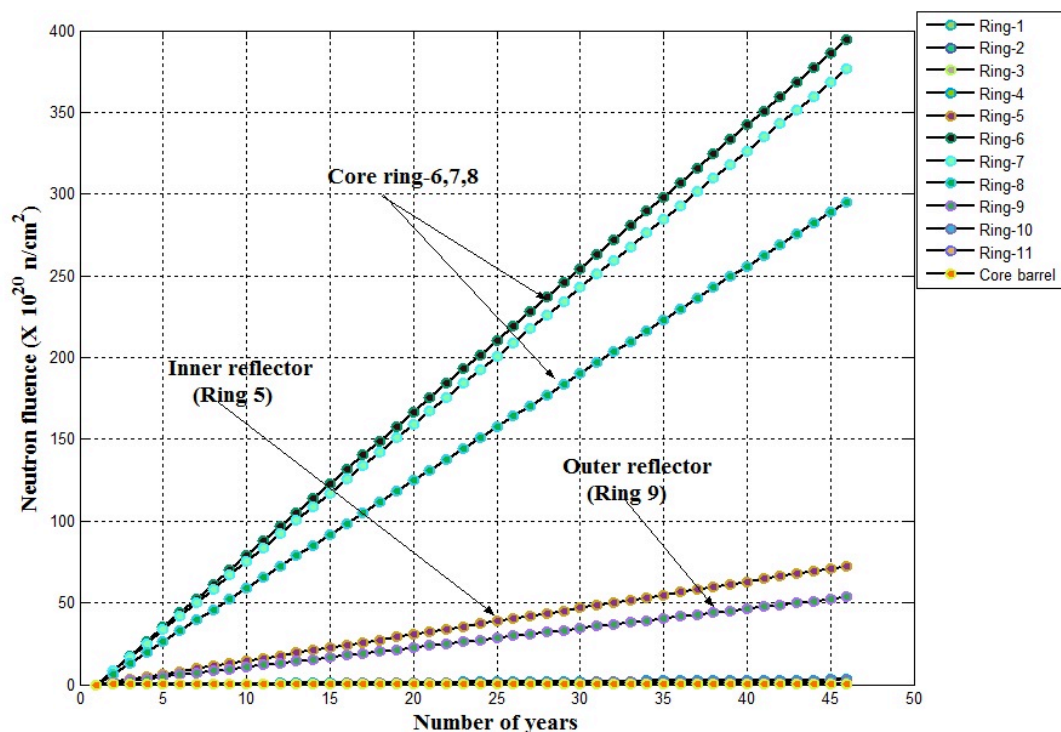


Figure 10. Neutron fluence at different rings with respect to operating years

4.5 Thermal Hydraulics Input for Stress Analysis

To carry out stress analysis, it is necessary to know the temperature and pressure distribution inside the core in addition to the neutronics information. This information can be obtained from thermal-fluid analysis of the core. The General Atomics GT-MHR design has an 850 °C average outlet temperature with a variation between the hottest and coolest flow channels of about 300 °C (i.e. a hot channel outlet temperature of about 1000 °C). It is noted that General Atomics is expected to modify the GT-MHR design to achieve the required NGNP average outlet temperature of 900 to 950 °C (and a hot channel temperature of about 1050 to 1000 °C). The temperature and pressure distribution can be found by performing a standard thermal fluid analysis and/or by either using a stand-alone computational fluid dynamics (CFD) analysis code^{31,33} or by using a general purpose multiphysics code²³. Coupling between CFD and stress analysis may become necessary if there is a significant change in the flow path geometry during the design lifetime. A series of uncoupled analyses based on estimated geometry at various stages of the operating life may be acceptable if the geometry changes are relatively small.

4.6 Irradiation damage mechanics in graphite

To develop a suitable material model, it is necessary to understand how neutron irradiation changes the underlying graphite microstructure of the core component, and the mechanisms which cause irradiation induced dimensional change and creep. The following subsections elaborate on this technical topic in more detail.

4.6.1 Graphite Microstructure

Nuclear graphite is polycrystalline and has a layered structure. In each layer, the carbon atoms are arranged in a hexagonal lattice with a separation of 0.142 nm, and the distance between the lattice planes is 0.335 nm.³⁴ Each layer consists of a honeycomb-like hexagonal lattice and forms plane called basal plane. Figure 11 shows a schematic of a typical graphite basal plane.

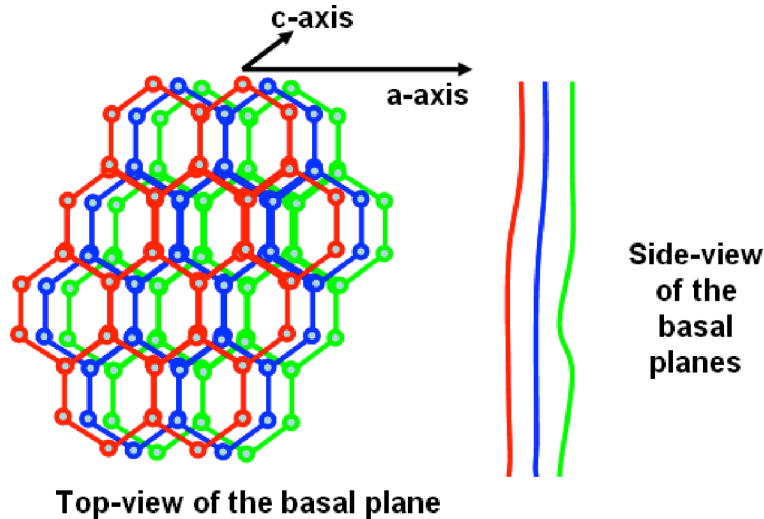


Figure 11. Schematic of graphite microstructure. Each basal plane consists of honeycomb-like hexagonal lattice. The axis parallel to basal plane is referred as a-axis, and perpendicular to basal plane is referred as c-axis.

Graphite is typically manufactured from petroleum cokes and using a suitable binder, using moulding or extrusion for billet fabrication. Pores and cracks are inherent to the microstructure and develop during thermal treatments (baking and graphitization) due to gas evolution and/or anisotropic thermal shrinkage during cooling from high temperature graphitization. The final microstructure of the manufactured graphite depends on the structure of the coke, binder, and the manufacturing process.

The manufacturing process leads to a product with approximately 20% porosity either as gas evolution pores in the binder or within the crystallite longitudinal cracks of various widths often referred to as Mrozowski cracks.²⁴ At the crystallite level, the graphite has strong hexagonal basal planes with much weaker bonding between the planes. The “Mrozowski” cracks can appear in the weaker ‘c’ direction during cooling from the graphitization temperature ~3000 C. This is due to the large difference in the coefficient of thermal expansion in the two crystallographic directions. The cracks in the ‘c’ direction give graphite good thermal shock resistance and allow large crystal expansion in the ‘c’ direction without leading to inter-crystalline cracking. In addition to the pores on the ‘a’ and ‘c’ direction the Mrozowski cracks in the ‘c’ direction provides accommodation spaces that can be taken up by irradiation-induced crystal growth. The above microstructural phenomenon often plays an important role in irradiation-induced crystal growth and in determining changes in component properties during reactor operation.

4.6.2 Mechanism of Irradiation Induced Dimensional Change in Nuclear Graphite

In HTGRs, fast neutrons with an energy range of 1eV to ~10MeV impinge on the graphite components resulting in radiation-induced damage.³⁶ These impingements on the crystal lattice cause the carbon atoms to be displaced from their equilibrium positions – creating lattice vacancies and interstitial carbon atoms. The displaced carbon atoms recoil through the lattice and produce other carbon atom displacements in a cascade effect. Due to these cascade effects, two types of microstructural phenomena occur; first, cluster of displaced interstitial atoms and second, vacancy defects along the basal plane. The cascaded carbon atoms tend to be clustered in small groups of 5–10 atoms. The interstitial atoms are pushed in the weaker ‘c’ direction and cluster forms in between two graphite layers or basal planes. Portion of the displaced carbon atoms are lost to the boundary layers by diffusing into lattice vacancies. Other displaced atoms coalesce to form linear molecules, which in turn may form the nucleus of an interstitial loop – essentially a new graphite plane. A schematic of the formation of interstitial loops is depicted in Fig. 12. Interstitial clusters, on further irradiation, may be destroyed by impinging neutrons or displaced energetic carbon atoms (irradiation annealing).

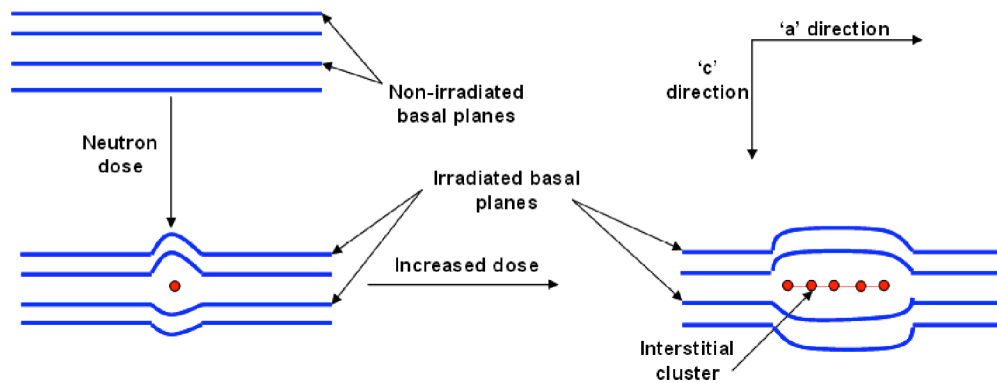


Figure 12. Schematic showing interstitial defects (swelling along ‘c’ direction).

Along with interstitial cluster formation and resulting ‘c’ direction swelling, the energetic neutrons form vacancies along the basal planes by pushing out the carbon atoms. Due to the cascading effect, multiple vacancy sites are formed in the neighborhood of a single vacancy. Like the interstitial cluster, the vacant sites may eventually join together to form a small vacancy loop which may eventually lead to the collapse of the layer parallel to the basal plane (or along ‘a’ direction). This results in shrinkage along the ‘a’ direction. The vacancy defect process is schematically illustrated in Fig. 13.

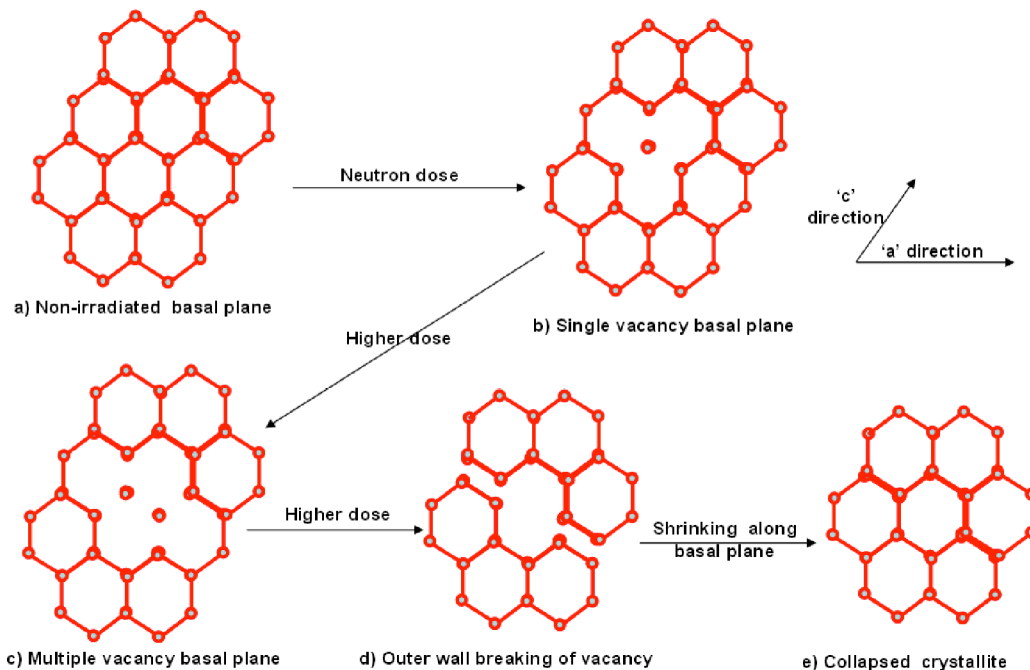


Figure 13. Schematic showing vacancy defects (shrinkage along 'a' direction).

In polycrystalline graphite, thermal shrinkage cracks (formed during manufacture) that are preferentially aligned in the crystallographic a-direction initially accommodate the c-direction expansion, so overall a-direction contraction is observed and the graphite undergoes net volume shrinkage. With increasing neutron dose, the incompatibility of crystallite dimensional changes leads to the generation of new pores, and the volume shrinkage rate falls, eventually reaching zero. The graphite then begins to swell at an increasing rate with increasing neutron dose because of the combined effect of c-axis growth and generation of new pores. The graphite thus undergoes a volume change "turnaround", eventually into net growth which continues until the generation of cracks and pores in the graphite, due to differential crystal strain, eventually causes total disintegration of the graphite.

4.6.3 Effects of Grain Orientation and Irradiation Temperature on Dimensional Change

The irradiation dimension change rate is highly dependent on the grain orientation in graphite components. For example, in case of an extruded component (or a component machined from an extruded billet) the crystallographic a-axis will be preferentially oriented along the direction parallel to the extrusion direction. As discussed above, since the shrinkage rate in the 'a' direction will be higher than that in the perpendicular 'c' direction, dimensional change rate along the extrusion direction will be higher than that in the direction perpendicular to the extrusion direction. Burchell and Snead³⁶ verified this behavior for H-451 graphite at different temperatures. Similarly, the irradiation temperature has a large effect on the dimension change rate. At higher temperatures, the turnaround occurs at lower neutron dose compared to the behavior at lower temperatures.^{18, 36}

4.7 Oxidation of Graphite

Graphite is used in a variety of nuclear reactor types; principally for moderator, reflector, fuel sleeve and fuel tube material. Since it is a form of carbon, like coal and charcoal, its oxidation behavior might be expected to be of concern to the graphite chemist. However, unlike coal and charcoal, which contain fuel in them in the form of volatile hydrocarbons, hydrogen, and oxygen as constituents, graphite contains only carbon. Thus, while it is not in itself combustible, right conditions containing continuous supply of oxygen and high temperature can promote oxidative weight loss and material consumption. The oxidizing environments of particular interest are air (oxygen), carbon dioxide and steam (water).

4.7.1 Reactions and Thermodynamics

The oxidation of graphite has been discussed in details by Blanchard³⁷.

4.7.1.1 Reactions with Oxygen



Where ΔH is the standard enthalpy of formation at 298°C.

The above reactions are exothermic and favored thermodynamically. Despite this fact, pure dense nuclear graphites do not readily react with air, so kinetic factors are obviously of importance.

4.7.1.2 Reactions with CO₂

The overall reaction is



4.7.1.3 Reactions with Steam



The hydrogen produced can then react with carbon to give the reactions



This is the water gas shift reaction which takes place in the gas phase. In many practical cases, products from the above reactions are free to escape, such that thermodynamic equilibrium is not reached. The enthalpy changes are of importance, however since they give a measure of the heat produced in exothermic reactions.

4.7.1.4 Catalytic Oxidation by Fission Product Impurities

Stolz and Werner³⁸ and Pointud et al.³⁹ have reported on the catalysis by different metals of the corrosion of graphite in presence of water vapor, carbon dioxide or oxygen. Laboratory testing has shown that steam reactions with graphite can be greatly accelerated by fission products strontium and barium. Graphite with 0.05% strontium and barium, respectively, showed 130 times and 1000 times faster reaction rates at 850° C compared to normal graphite. The diffusion of strontium and barium in graphite is very low. The main contribution to catalysis is from Ba-137, a decay product of Cs-137 (half-life 30 years), which has a high diffusion constant. When using the values measured, this isotope alone increases the reaction rate by a factor of approximately 5.

Additional corrosion is caused by radiolysis of H₂O and CO₂ resulting in oxygen that more readily reacts with graphite. The reactions of steam and carbon dioxide with graphite are generally not reversible on graphite because the reactions are too slow. Only by catalysis with certain metals, especially iron, cobalt, and nickel, do the reactions run in reverse even at the 500°C temperatures that are typical of steam generators.

4.7.2 Oxidation Mechanisms

In design stress analysis, oxidation effects are not accounted for directly but are included as a loss of thickness, if necessary. Also, influence of oxidation on changes in relevant mechanical properties need to be taken into account if they are significant. This section, which is a review of the details of oxidation mechanisms, is included for the sake of completeness.

The oxidation/steam oxidation mechanism of graphite consists of sequential physical and chemical reaction steps.

- (1) Transport of oxidant to the graphite surface
- (2) Adsorption of oxidant onto the graphite surface (physisorption)
- (3) Formation of carbon-oxygen bond (chemisorption)
- (4) Formation of carbon-hydrogen bonds – Reaction Eq. 15 (reduction)
- (5) Breaking the carbon-carbon bonds
- (6) Desorption of CO or other products
- (7) Transport of reaction product from the graphite surface

Any of the above steps may be rate-controlling; i.e., develop the major reactant concentration gradient. The controlling factors are as follows:

- (8) The rate at which the oxidant is supplied to the surface
- (9) The partial pressure of oxygen

- (10) The reactive surface area available to the oxidant at the surface
- (11) The amount and distribution of catalytic impurities in the graphite
- (12) Temperature
- (13) The rate at which reaction products are removed
- (14) The fast neutron damage to the graphite
- (15) The amount of pre-oxidation (radiolytic or thermal burn off)
- (16) The quantity of in-pore deposits
- (17) The effective diffusion coefficient

4.7.3 Oxidation Regimes and Kinetics

Regime 1: This chemical regime (typically at low temperatures) is characterized by the intrinsic reactivity of the graphite (steps 2 to 6 above). Reaction between air and nuclear graphite is generally not measurable below 350 °C and only becomes significant at > 400 °C.

The units for oxidation rate imply a rate law of the form

$$\frac{dm}{dt} = km, \quad (17)$$

where,

m = graphite mass (kg);

t = time (s); and,

k = a (rate) constant (s^{-1}).

However, for a solid reacting body, rate laws of the form shown below would be expected for reaction at the superficial surface

$$\frac{dm}{dt} = k \text{ for slabs}; \quad (18a)$$

$$\frac{dm}{dt} = km^{1/2} \text{ for cylinders}; \text{ and,} \quad (18b)$$

$$\frac{dm}{dt} = km^{2/3} \text{ for spheres}. \quad (18c)$$

The variation of reaction rate with temperature is very important and follows typical Arrhenius type:

$$K = A \exp(-E/RT), \quad (19)$$

where,

A is a pre-exponential factor (s^{-1});

E is the apparent activation energy ($J.mol^{-1}$) (typically $170 kJ.mol^{-1}$); and

R is the gas constant ($J.mol^{-1}.K^{-1}$).

Reaction of H_2O with graphite is important for HTGRs because of the possible small leakage from the steam side into the gas circuit, where it can react with the hot graphite fuel cans. Since the partial pressure of water vapor is variable, rate equations of the form:

$$r = AP^n \quad (20)$$

are applied, where,

r = specific reaction rate ($kg.kg^{-1}s^{-1}$);

A = a rate constant ($s^{-1}.(N.m^{-2})^{-1}$); and,

P = partial pressure of water vapor ($N.m^{-2}$).

The reaction with water vapor is generally not significant below $800\text{ }^\circ\text{C}$ and approximately obeys Eq. 20 with $n = 0.5$ over a temperature range $1000\text{-}1200\text{ }^\circ\text{C}$.

Regime 2: In this regime, the reaction rate is high enough for access of the gas to the in-pore structure to be significantly limited by diffusion control (steps 1 and 7 above). The reaction rate at the superficial surface of the graphite is so high that most of the oxidant is consumed there, the oxidant concentration gradient developing across the laminar sub-layer. The reaction rate is now expressed in terms of the superficial surface area of the graphite ($kg.m^{-2}s^{-1}$), together with any oxidant partial pressure dependence.

Grade H-451 Graphite

Steam-Graphite Reaction Rate

The Langmuir-Hinshelwood equation is used to predict the chemical, kinetically-limited steam-graphite oxidation rates for the H-451 graphite.⁴⁰

$$Rate = \frac{K_1 P_{H_2O} F_b F_c}{1 + K_2 (P_{H_2})^n + K_3 P_{H_2O}} \quad (21)$$

Where,

Rate = local graphite mass fraction reacting per second;

P_{H_2}, P_{H_2O} = local partial pressures of hydrogen and steam, respectively;

F_b, F_c = modifiers for the effects of mass loss due to the oxidation reaction and presence of catalysts, respectively

$$F_b = 0.447 + 0.8094b - 0.3221b^2 - 0.0681b^3 - 0.00613b^4 + 12.32 \times 10^{-6}b^5 + 2.89 \times 10^{-5}b^6 - 1.15 \times 10^{-6}b^7$$

$0 \leq b \leq 13$, for higher mass loss, F_b value at 13% mass loss should be used;

Where, b = per cent graphite mass loss. F_b is normalized to 1.0 at 1% mass loss

$$F_c = 1 + (C_{Ba} + 0.2C_{Sr})\exp(12.153 - 4.264 \times 10^{-3}T);$$

where, C_{Ba} and C_{Sr} = concentration of barium and strontium catalyst (mg/g graphite);

T is temperature in K.

$$n = 0.75$$

$$K_j = k_j \exp(E_j/RT) \quad (22)$$

$j = 1, 2, 3$

$$k_1 = 900 \text{ (s.Pa)}^{-1}, k_2 = 110 \text{ (Pa}^{-0.75}), k_3 = 30 \text{ (Pa}^{-1});$$

$$E_1 = -274,000 \text{ J/mol}, E_2 = -74660 \text{ J/mol}, E_3 = -95850 \text{ J/mol};$$

$$R = 8.314 \text{ J/mol-K}$$

Air-Graphite Reaction Rate⁴⁰

The rate of oxidation of graphite in air is given by:

$$\text{Rate} = K \exp(-E / RT) P_{O_2} \quad (23)$$

Where,

Rate = local graphite mass fraction reacting per second;

P_{O_2} = local oxygen partial pressure;

$K = 0.79 \text{ (s.Pa)}^{-1}$, and, $E = 1.7 \times 10^5 \text{ J/mol}$.

Effect of Radiolysis on Oxidation Rate

Eto et al. ⁴¹ have shown that the contribution of radiolytic effects on the reaction rates is negligible above 777 °C and neutron irradiation does not affect the reaction rates except at the initial stage of irradiation. For design analysis purposes, the radiolytic effect on oxidation rate can be neglected.

5. GRAPHITE MATERIAL PROPERTIES AND MATERIAL MODELS

To develop the stress analysis code for graphite core components, it is necessary to know the non-irradiated and irradiated graphite material properties and the corresponding material models, which describe the effects of irradiation damage over time. The present chapter discusses some of these material properties and the corresponding material models. Non-irradiated material properties for many graphite grades can be found in open literature. However, irradiated material properties are available only for few graphite grades in the open literature. For example, most of the literature on HTGR graphite core refers only two data sets. First, the data set available through General Atomics irradiation test on H-451 graphite and second, the data set available through JAERI irradiation test on IG-110 graphite grades. The IG-110 grade is currently being used in the Japanese HTTR core. Keeping in mind that H-451 and IG-110 grades are the most cited graphite grades in HTGR related literature, the present chapter only presents the non-irradiated and irradiated material properties of H-451 and IG-110 graphite grades. We also note that irradiation is still ongoing at the Advanced Test Reactor (ATR) at Idaho national Laboratory with newer nuclear grade graphites intended for use in the NGNP reactor, and the preliminary data may become available during 2012.

Although graphite is known to be anisotropic, modern reactors use graphites with semi-isotropic properties. Tensile/compression stress-strain curves of virgin graphite at room temperature are non-linear displaying a “permanent set” after unloading. The permanent set is not due to classical plasticity (graphite is brittle) because it can be removed and linearity recovered by subjecting it to either a high temperature annealing treatment⁴² or neutron irradiation.⁴³ Under reactor environment, graphite experiences irradiation-induced creep. Unlike thermally driven high temperature creep, irradiation-induced creep is driven by neutron flux. The stress exponent for thermally driven creep is generally >1 ; for neutron flux driven irradiation creep, the stress exponent for graphite is $=1$, i.e., it is linear viscoelastic. Thermally induced creep in graphite is negligible at HTGR-relevant temperatures. Although ABAQUS has built-in material models for handling linear viscoelastic materials, the inclusion of irradiation-interaction thermal and dimensional change strains would require their incorporation through the use of a user-defined subroutine called UMAT.

5.1 Non-irradiated H-451 & IG-110 Graphite Material Properties

The non-irradiated material properties of H-451 and IG-110 graphites are given in Tables 11 and 12, respectively.

Table 11. Non-irradiated properties of H-451 graphite (Virgil’ev and Kalyagina, 2003)⁴⁴.

Property	Unit	H-451 graphite
Bulk density	(Mg/m ³)	1.76
Mean tensile strength	(MPa)	16(WG) 14(AG)

Table 11. Non-irradiated properties of H-451 graphite (Virgil'ev and Kalyagina, 2003)⁴⁴

Property	Unit	H-451 graphite
Mean compressive strength	(MPa)	56(WG) 54(AG)
Flexural strength	(MPa)	28(WG) 26(AG)
Elastic modulus	(GPa)	9(WG) 8(AG)
Coefficient of thermal expansion in the range of 20-500 °C	($\times 10^{-6} \text{ K}^{-1}$)	3.6(WG) 4.6(AG)
Thermal conductivity at room temperature	(W/m-K)	135 (WG) 125(AG)
Critical stress intensity factor, K_{IC}	($\text{MPa}\cdot\text{m}^{1/2}$)	28(WG) 26(AG)
Ash content	(wt ppm)	-
Grain size	(μm)	500
Isotropy	-	Anisotropic or nearly Isotropic
Coke type		Petroleum coke
Forming method		Extruded
Country of origin	-	USA

Table 12. Non-irradiated material properties for IG-110 graphite (JAERI report, 2009)²⁹.

Property	Unit	IG-110 graphite
Bulk density	(Mg/m^3)	1.78
Mean tensile strength	(MPa)	25.3
Mean compressive strength	(MPa)	76.8
Elastic modulus ($\pm 1/3$ Su gradient)	(GPa)	7.9
Elastic modulus (Starting point gradient)	(GPa)	9.9

Table 12. Non-irradiated material properties for IG-110 graphite (JAERI report, 2009)²⁹

Property	Unit	IG-110 graphite
Mean coefficient of thermal expansion (Room temperature ~ 400 °C)	($10^{-6}/^{\circ}\text{C}$)	4.06
Thermal conductivity (400 °C)	(W/(m-K))	81.4
Ash content	(wt ppm)	≤ 100
Maximum grain size	(μm)	20
Isotropy	-	Isotropic
Coke type		Petroleum coke
Forming method		Isostatically molded
Country of origin	-	Japan

5.1.1 Non-irradiated Stress-Strain Curve

Non-irradiated tensile and compressive stress-strain curves of graphite IG-110 were presented in a INL report⁴⁵ and reproduced in Fig. 14. The curves are terminated at failure. Note that the curves are nonlinear, although the tensile and compressive curves overlap. At low strains (0.001 for tensile; 0.0035 for compression) typical of design application, a linear approximation is acceptable. However, it is considered that graphite exhibits non-linear elastic response because of microcracking during loading and the contribution due to the presence of inherent Mroowzki microcracks formed during cool down from graphitization process.

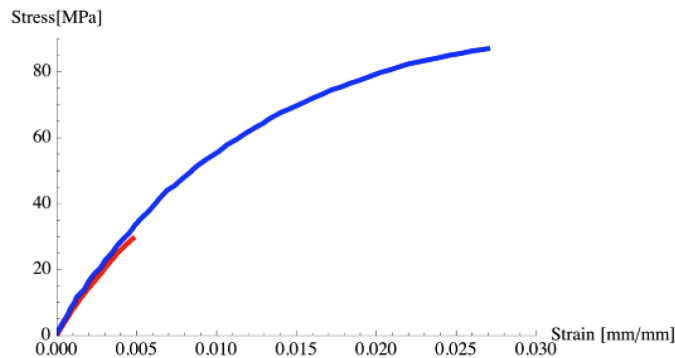


Figure 14. Uniaxial stress-strain curves of IG-110 at room temperature in tension (red) and compression (blue).

Two relationships have been reported for the non-linear stress-strain response of graphite in the literature.

Ramberg-Osgood Equation⁴⁵

$$\varepsilon = \frac{\sigma}{E} + \varepsilon_o \left(\frac{\sigma}{\sigma_o} \right)^n \quad (24)$$

where E is Young's modulus and ε_o , σ_o and n are parameters determined from the stress-strain curve.

Jenkin's Equation⁴⁶

$$\varepsilon = \frac{\sigma}{E} + \left(\frac{\sigma}{A} \right)^2 \quad (25)$$

Fits of both equations to the IG-110 stress-strain curves (Fig. 14) are shown in Figs. 15a-b for tensile and compressive curves, respectively. Both equations give excellent fits to the tensile stress-strain curve. The Jenkin's equation gives a better fit for the compressive curve at low strains, but the Ramberg-Osgood equation fits the compressive curve better at large strains.

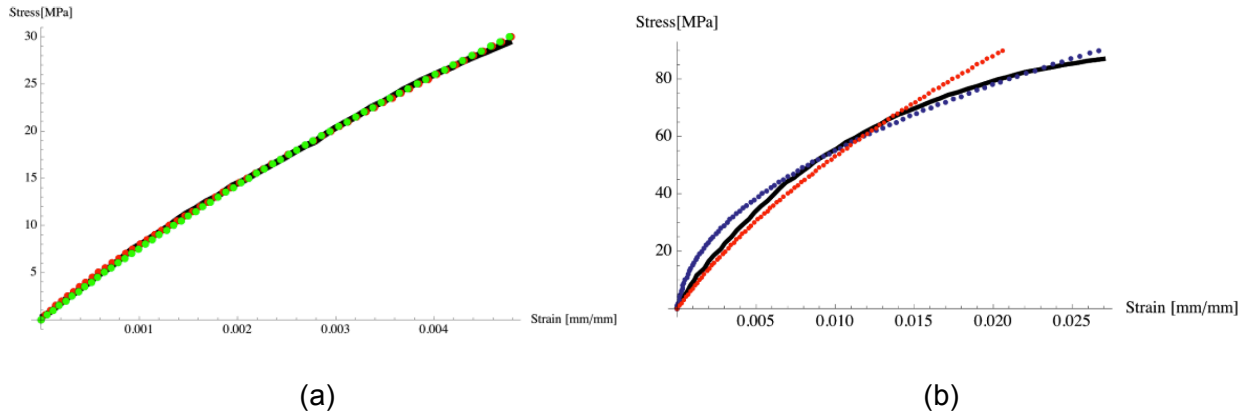


Figure 15. (a) Tensile and (b) compressive stress-strain curves (black lines) of IG-110 and the Ramberg-Osgood equation fits (blue lines) and Jenkin's equation fits (red lines).

5.1.2 Effect of Oxidation on Material Properties

It is well known that graphite can oxidize and suffer mass loss in an oxidative environment at temperature in excess of 450 °C. However, the (impure) helium HTGR atmosphere is expected to result in negligible mass loss during reactor operation. But, under air-ingress accidents, the oxidation of the core graphite materials will have an adverse influence on the structural integrity of HTGR core components. Therefore, the loss in properties of graphite due to oxidation must be considered in structural integrity assessments of graphite core components

Grade H-451 Graphite

The reduction in tensile strength (S) and elastic modulus (E) of uniformly oxidized H-451 graphite can be represented by the following relationship⁴⁰:

$$S/S_o = \exp(-5x); \quad (26)$$

and,

$$E/E_0 = \exp(-6x); \quad (27)$$

Where,

x = fractional weight loss due to oxidation;

S, E = tensile strength and Young's modulus of oxidized graphite;

S₀, E₀ = tensile strength and Young's modulus of non-oxidized graphite.

Equations 26 and 27 are valid for uniformly oxidized H-451 graphite with mass loss of up to 20%.

IG-110 Graphite

Tensile and compressive strength changes of IG-110 graphite due to oxidation, as given in the JAERI design handbook²⁹, are plotted in Fig. 16.

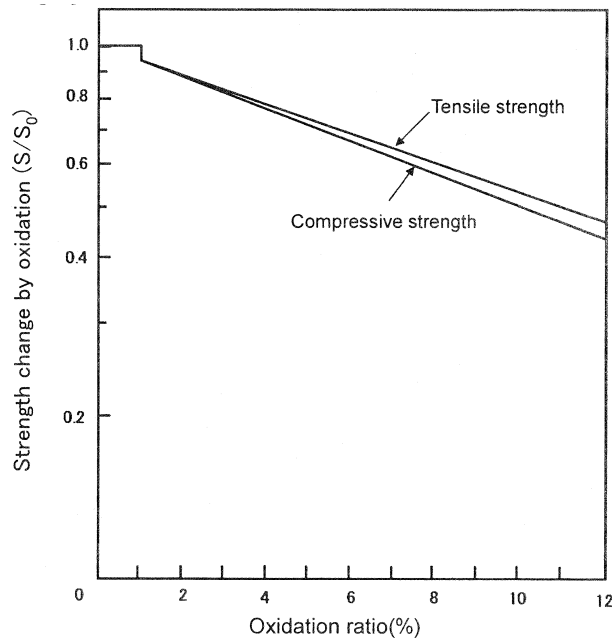


Figure 16. Strength change of IG-110 graphite due to oxidation

5.2 Irradiated Material Properties and Material Models

Irradiated material properties as a function of temperature and fluence (or irradiation dose) are necessary for developing the stress analysis code for graphite core components. The following irradiated material properties are required for stress analysis.

- a) Dimensional change;

- b) Coefficient of thermal expansion (CTE);
- c) Strength;
- d) Young's modulus;
- e) Thermal conductivity; and,
- f) Elasticity Poisson's ratio.

From a literature survey it was found that very few test data are available on the dependence of elastic Poisson ratio on irradiation fluence and temperature. Also, majority of the available literature on HTGR design refers to the irradiated test results on two grades of graphite - H-451 and IG-110. The details of the test results on H-451 graphite can be found in Price and Beavan.⁴⁷⁻⁴⁹ Similarly, detailed irradiated material properties of IG-110 can be found in a JAERI report. The temperature and fluence dependence of the material properties can be written in functional form as:

$$P = f(\gamma(t, \Omega), \theta(t, \Omega)), \quad (28)$$

where, P represents the above mentioned irradiated material properties, $\gamma(t, \Omega)$ represents the time t and location Ω dependent fluence; similarly, $\theta(t, \Omega)$ represents the time t and location Ω dependent temperature. For developing a constitutive relation, which will be used in the stress analysis code, it is necessary to know the functional relation of the material properties given by Eq. 28. The functional form of the Eq. 28 can be determined by any of the following three ways:

- a) Physics-based mechanistic relation;
- b) Semi-empirical relation; and,
- c) Empirical-relation.

For physics-based mechanistic relation, it is necessary to understand the damage growth mechanics from the graphite microstructure, temperature, dose, applied load, and internal stress. A rigorous consideration of these aspects involves high levels of modeling and computational complexity, with difficulty in validation and verification, both analytically and experimentally. Thus, no literature is available on this subject. The semi-empirical relation is based on both physics-based damage growth mechanism and test data. The few investigations that have adopted this approach are reviewed in this section. In most irradiation induced stress analysis work, the pure empirical approach has been used. The present section also reviews the empirical approach of material model for H-451 graphite as reported in the General Atomics graphite design hand book⁴⁰ and for IG-110 graphite as reported in the JAERI report. The following subsections describe the individual irradiated material properties and material models in details.

5.2.1 Irradiation-induced Dimension Change Material Data and Material Models

H-451 Graphite

The dimensional change data for H-451 graphite grade, as reported in the General Atomics Graphite Handbook⁴⁰, is plotted in Fig. 17. The same data in tabular form is given in Appendix A.

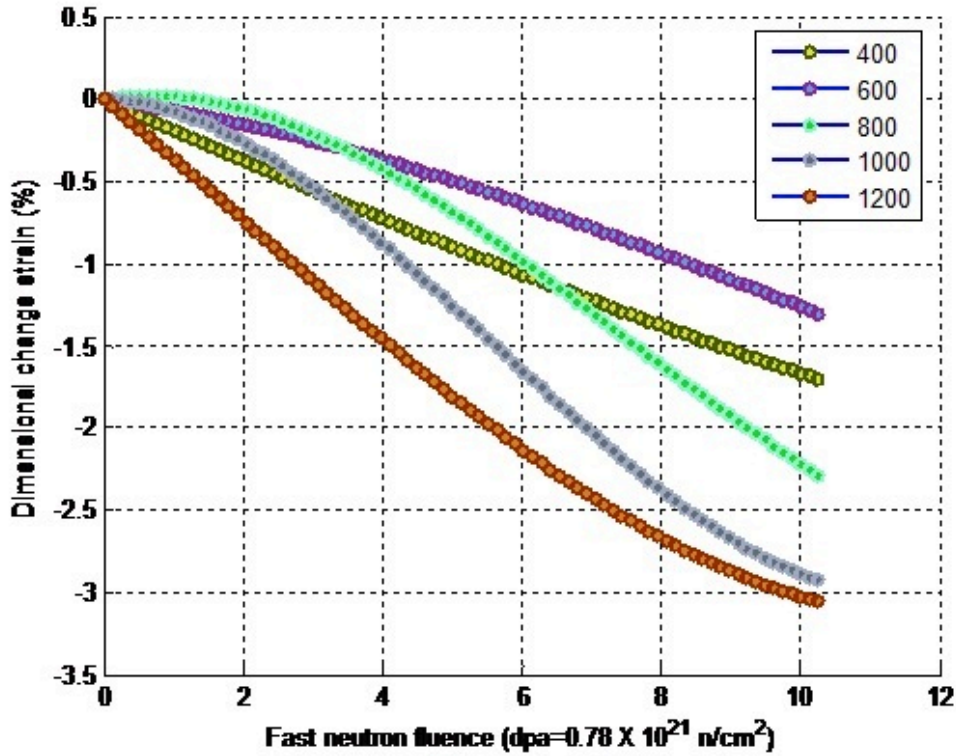


Figure 17. Rescaled H-451 dimensional change data taken from General Atomics Report.⁴⁰

The empirical material model for dimensional change strain of H-451 graphite is given in a General Atomics report.⁴⁰ The empirical relationship is given in Eq. 29.

$$\begin{aligned}
 \varepsilon^{dim} &= f(\gamma(t, \Omega), \theta(t, \Omega)) \\
 &= (C_1 + C_2\theta + C_3\theta^2 + C_4\theta^3 + C_5\theta^4)\gamma + (C_6 + C_7\theta + C_8\theta^2 + C_9\theta^3 + C_{10}\theta^4 + C_{16}\theta^5)\gamma^2 \\
 &\quad + (C_{11} + C_{12}\theta + C_{13}\theta^2 + C_{14}\theta^3 + C_{15}\theta^4 + C_{17}\theta^5 + C_{18}\theta^6)\gamma^3 \\
 &\quad ; \text{ for } 350 \leq \theta \leq 1300 \text{ } ^\circ\text{C} \text{ \& } \gamma \leq 10 ; \gamma \text{ is in } \times 10^{25} \text{ n/m}^2 \text{ unit}
 \end{aligned} \tag{29}$$

The value of the different coefficients can be found from Table 13. Using Eq. 29, the dimensional change strains for H-451 can be calculated for different temperatures and fluence conditions (Fig. 18).

Table 13 Polynomial coefficients for dimensional change strain of H-451 graphite.⁴⁰

Coefficient	Axial	Radial
C ₁	1.11617	1.15132
C ₂	-0.92197 x 10 ⁻²	-0.82968 x 10 ⁻²
C ₃	+0.20463 x 10 ⁻⁴	+0.17060 x 10 ⁻⁴
C ₄	-0.16458 x 10 ⁻⁷	-0.12645 x 10 ⁻⁷
C ₅	+0.40809 x 10 ⁻¹¹	+0.27657 x 10 ⁻¹¹
C ₆	+0.64947	+0.39177
C ₇	-0.56929 x 10 ⁻²	-0.36540 x 10 ⁻²
C ₈	+0.18972 x 10 ⁻⁴	+0.12750 x 10 ⁻⁴
C ₉	-0.29277 x 10 ⁻⁷	-0.20230 x 10 ⁻⁷
C ₁₀	+0.20435 x 10 ⁻¹⁰	+0.14233 x 10 ⁻¹⁰
C ₁₁	-0.59274 x 10 ⁻²	+0.13110 x 10 ⁻¹
C ₁₂	-0.65404 x 10 ⁻⁵	-0.18768 x 10 ⁻³
C ₁₃	+0.32751 x 10 ⁻⁶	+0.10199 x 10 ⁻⁵
C ₁₄	-0.13449 x 10 ⁻⁸	-0.27004 x 10 ⁻⁸
C ₁₅	+0.22245 x 10 ⁻¹¹	+0.36498 x 10 ⁻¹¹
C ₁₆	-0.51973 x 10 ⁻¹⁴	-0.35768 x 10 ⁻¹⁴
C ₁₇	-0.16038 x 10 ⁻¹⁴	-0.23579 x 10 ⁻¹⁴
C ₁₈	+0.41756 x 10 ⁻¹⁸	+0.57329 x 10 ⁻¹⁸

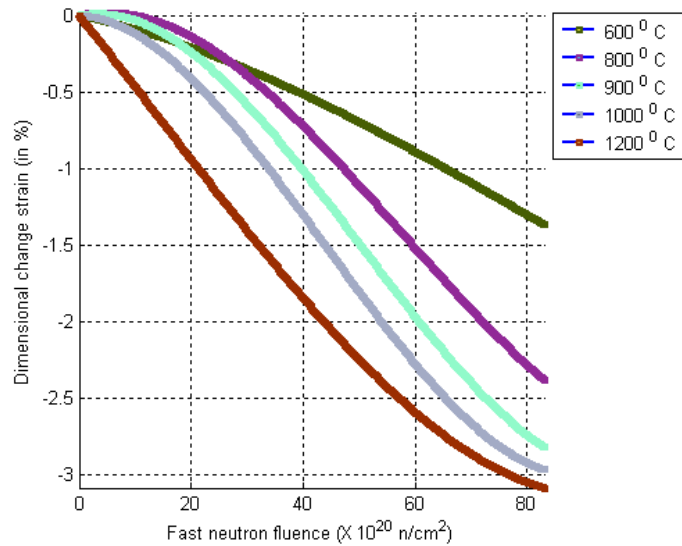


Figure 18. Calculated values of dimensional change strain in H-451 graphite.

IG-110 Graphite

The dimensional change data for IG-110 graphite grade as reported in the JAERI report is plotted in Fig. 19. The same data in tabular form is given in Appendix B.

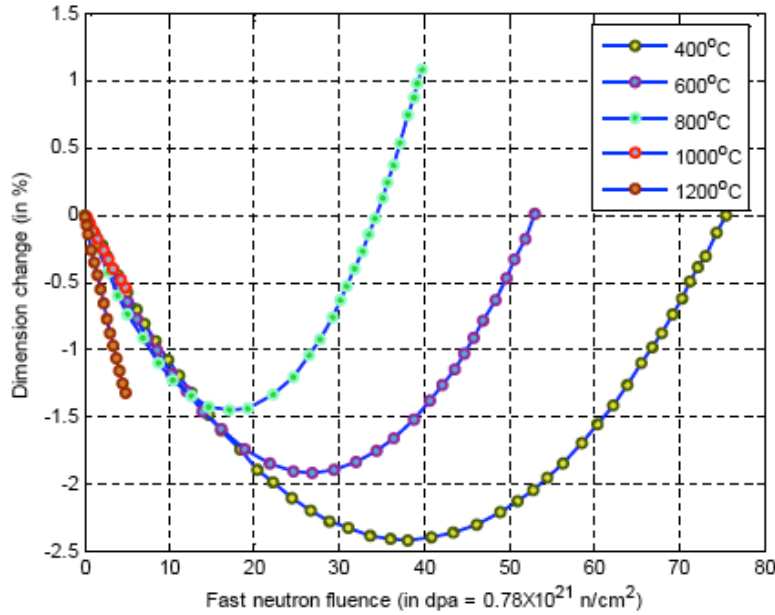


Figure 19. Rescaled IG-110 dimensional change data taken from JAERI report.²⁹

The empirical material model for dimensional change strain for IG-110 graphite is given in the JAERI report.²⁹ The empirical relation is as given below.

$$\begin{aligned}\varepsilon^{dim} &= f(\gamma(t, \Omega), a_{j=1,2}) \\ &= a_1 \gamma^2 + a_2 \gamma\end{aligned}\quad (30)$$

where, $a_{i=1,2}$ are two temperature-dependent empirical constants as given below.

Table 14 Polynomial coefficients for dimensional change strain material model of IG-110 graphite.²⁹

Grade	IG-110	
	a_1	a_2
Irradiation temperature (°C)		
400	2.79×10^{-1}	-1.64
600	4.50×10^{-1}	-1.86
800	8.21×10^{-1}	-2.19

5.2.2 Irradiated coefficient of thermal expansion (CTE) change material data and model

The thermal expansion, and the coefficient of thermal expansion of graphite change during neutron irradiation. It depends not only on neutron fluence but also on irradiation temperature. Applied load may also influence thermal expansion; however, experimental data are not available for this effect. In this section, design curves for H-451 and IG-110 graphite grades are presented. The design curves are reproduced, respectively, from the General Atomics Handbook⁴⁰ and JAERI report²⁹. The fluence for both dataset are rescaled to dpa unit. The original figures and the corresponding extracted numerical data can be found in Appendices A and B.

H-451 Graphite

A plot of the change in thermal expansion coefficient with neutron fluence for various temperatures is given in Fig. 20. The empirical material model for the H-451 graphite CTE change as given in General Atomics Handbook⁴⁰ is reproduced in Eq. 31.

$$\frac{(\alpha_i - \alpha_0)}{\alpha_0} = f(\gamma(t, \Omega), \theta(t, \Omega))$$

$$= (0.27830 - 4.2734 \times 10^{-4} \theta + 1.7815 \times 10^{-7} \theta^2) \gamma - 2.0664 \times 10^{-2} \gamma^2 + 1.3601 \times 10^{-3} \gamma^3 \quad (31)$$

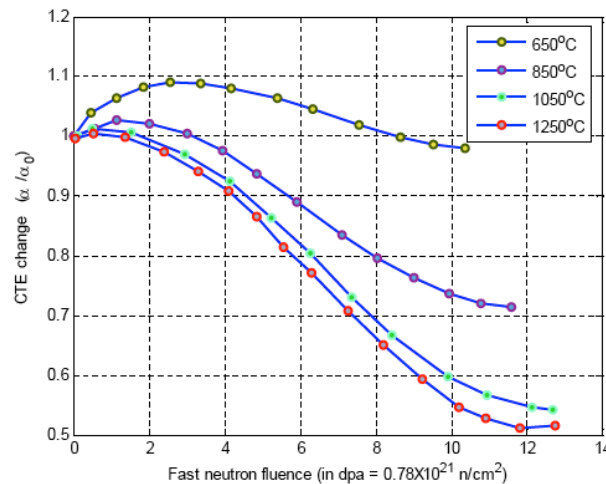


Figure 20. Rescaled CTE change data for H-451 graphite (original data taken from General Atomics graphite handbook.⁴⁰

IG-110 Graphite

A plot of the change in thermal expansion coefficient with neutron fluence for various temperatures is given in Fig. 20.

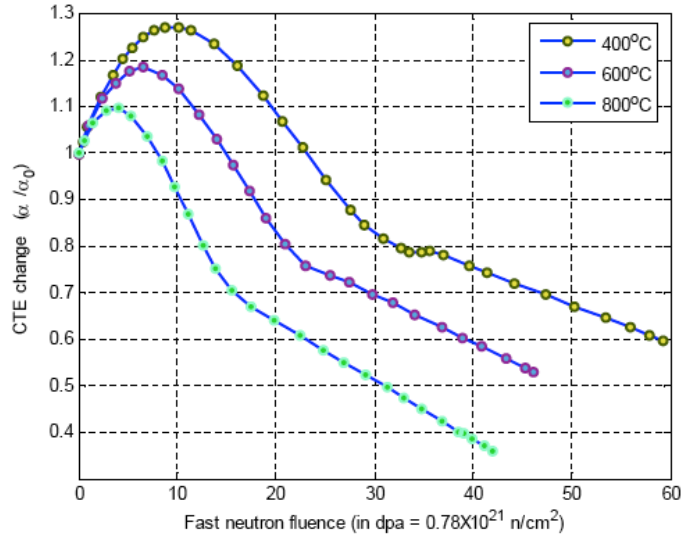


Figure 21. Rescaled CTE change data for IH-110 graphite (original data taken from JAERI Graphite Handbook.²⁹

The empirical material model for CTE change of IG-110 graphite as given in the JAERI report²⁹ is in Eq. 32.

$$\begin{aligned}
 \frac{\alpha_i}{\alpha_0} &= f(\gamma(t, \Omega), a, b, c, d, e) \\
 &= a\gamma^3 + b\gamma^2 + c\gamma + 1 \quad (\gamma \leq \gamma_{TA}) \\
 &= d\gamma + e \quad (\gamma > \gamma_{TA})
 \end{aligned} \tag{32}$$

where,

α_0 = Average coefficient of thermal expansion between 20°C and prospective irradiation temperature before irradiation;

α_1 = Average coefficient of thermal expansion between 20°C and irradiation temperature after irradiation;

γ = Fast neutron fluence ($\times 10^{26}$ n/m², E > 0.1 MeV);

γ_{TA} = Fast neutron fluence at turn around ($\times 10^{26}$ n/m², E > 0.1 MeV); and

a, b, c, d, e = empirical constants given in Table 15.

Table 15. Polynomial coefficients for CTE change material model of IG-110 graphite²⁹

Grade	IG-110				
	Irradiation Temperature (°C)	a	b	c	d
400	1.33×10^{-1}	-6.83×10^{-1}	8.00×10^{-1}	-1.03×10^{-1}	1.07
600	2.64×10^{-1}	-9.93×10^{-1}	7.96×10^{-1}	-1.34×10^{-1}	1.01
800	6.28×10^{-1}	-1.57	7.38×10^{-1}	-1.64×10^{-1}	8.96×10^{-1}

5.2.3 Irradiated elastic modulus change material data

The elastic modulus of graphite changes during neutron irradiation. It also depends on irradiation temperature. In this section, design curves for elastic moduli of grade H-451 and IG-110 graphites are presented. The design data for H-451 and IG-110 are obtained from General Atomics report⁴⁰, and JAERI repor²⁹. The fluence for both dataset are converted to dpa unit. The original figures and the corresponding extracted numerical data can be found in Appendices A and B.

H-451 Graphite

The variation of normalized Young's modulus of H-451 with fluence at various temperatures is plotted in Fig. 22.

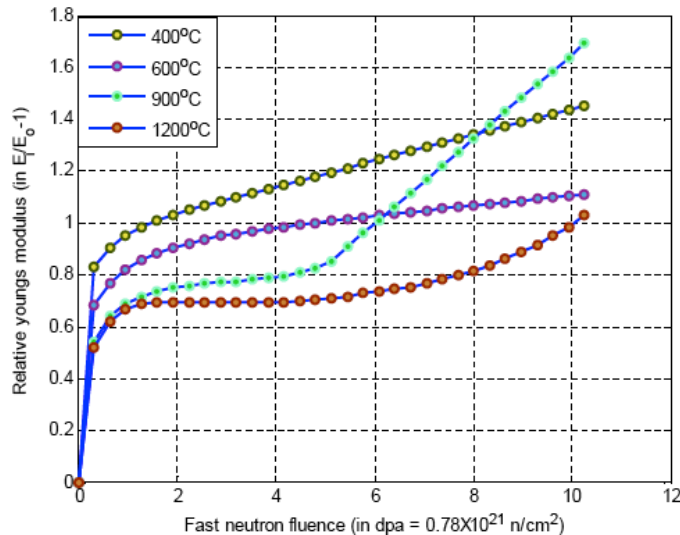


Figure 22. Rescaled Young's modulus change data for H-451 graphite (original data taken from the General Atomics handbook⁴⁰).

The Young's modulus data⁴⁰ can be fitted with a 4th order polynomial of temperature and a 5th order polynomial of fluence as shown in Eq. 33.

$$E_d = f(\gamma(t, \Omega), \theta(t, \Omega))$$

$$= (A_{00} + A_{01}\theta + A_{02}\theta^2 + A_{03}\theta^3 + A_{04}\theta^4) + (A_{10} + A_{11}\theta + A_{12}\theta^2 + A_{13}\theta^3 + A_{14}\theta^4)\gamma$$

$$+ (A_{20} + A_{21}\theta + A_{22}\theta^2 + A_{23}\theta^3 + A_{24}\theta^4)\gamma^2 + (A_{30} + A_{31}\theta + A_{32}\theta^2 + A_{33}\theta^3 + A_{34}\theta^4)\gamma^3 \quad (33)$$

$$+ (A_{40} + A_{41}\theta + A_{42}\theta^2 + A_{43}\theta^3 + A_{44}\theta^4)\gamma^4 + (A_{50} + A_{51}\theta + A_{52}\theta^2 + A_{53}\theta^3 + A_{54}\theta^4)\gamma^5$$

; for $400 \leq \theta \leq 1200$ °C & $\gamma \leq 10$; γ is in dpa

The values of the coefficients are listed in Table 16. The fitted data are compared with the original data in Fig. 23.

Table 16. Polynomial coefficients for dynamic Young's modulus of H-451 graphite.

$A_{i0}; i = 0, 2 \dots 5$	$A_{i1}; i = 0, 2 \dots 5$	$A_{i2}; i = 0, 2 \dots 5$	$A_{i3}; i = 0, 2 \dots 5$	$A_{i4}; i = 0, 2 \dots 5$
3.5784e-005	0.0058555	-1.4208e-005	1.2429e-008	-3.6589e-012
1.1435e-005	0.0018712	-5.6365e-006	7.4696e-009	-3.2456e-012
-5.9181e-006	-0.00096838	3.6218e-006	-5.1585e-009	2.2765e-012
1.4422e-006	0.000236	-9.3085e-007	1.32e-009	-5.7642e-013
-1.3133e-007	-2.1491e-005	8.454e-008	-1.185e-010	5.1231e-014
4.199e-009	6.8709e-007	-2.6527e-009	3.6598e-012	-1.5619e-015

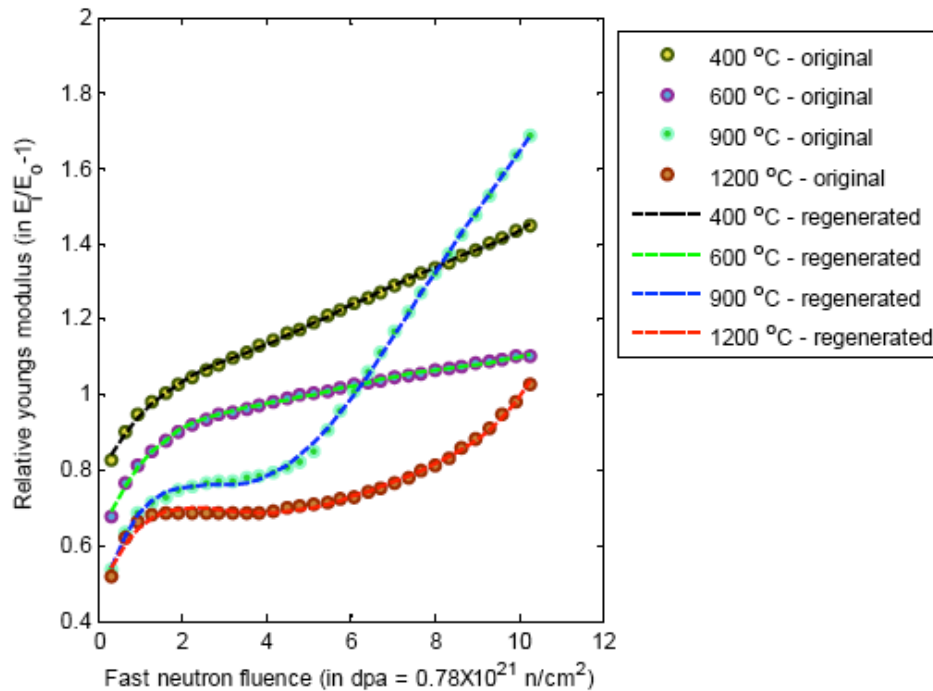


Figure 23. Original vs. fitted (regenerated) dynamic Young's modulus of H-451.

IG-110 Graphite

The variation of normalized Young's modulus of IG-110 with fluence at various temperatures is plotted in Fig. 24.

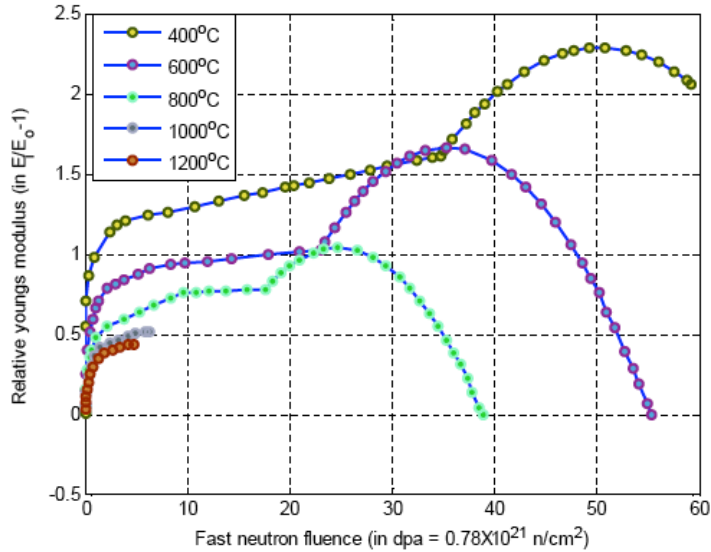


Figure 24. Rescaled elastic modulus change data for IG-110 graphite (original data taken from JAERI report²⁹).

The empirical material model for elastic modulus of IG-110 graphite as reproduced from JAERI report, is given in Eq. 34.

$$\begin{aligned} \frac{E_d}{E_o} - 1 &= f(\gamma(t, \Omega), a, b, c, d, e) \\ &= a\gamma + b \quad ; \text{for } \gamma \leq \gamma_c \\ &= c(\gamma + d)^2 + e \quad ; \text{for } \gamma > \gamma_c \end{aligned} \quad (34)$$

where,

γ = Fast neutron fluence ($\times 10^{26}$ n/m², $E > 0.1$ MeV);

γ_c = Fast neutron fluence at the beginning of high fluence region ($\times 10^{26}$ n/m², $E > 0.1$ MeV);
and,

a, b, c, d, e are temperature dependent constants given in Table 17.

Table 17. Polynomial coefficients for elastic modulus change material model.

Grade	IG-110				
Irradiatin Temperature(°C)	a	b	c	d	e
400	-1.69×10^{-1}	1.16	-4.56×10^{-1}	-3.92	2.29
600	-7.45×10^{-2}	8.89×10^{-1}	-6.84×10^{-1}	-2.75	1.66
800	-4.03×10^{-2}	7.26×10^{-1}	-8.45×10^{-1}	-1.93	1.04

5.2.4 Irradiated Strength Change Material Data

The values of both ultimate tensile and compressive strengths, (UTS and UCS) are required in stress analysis to evaluate the structural integrity of a core graphite component. The design stress limits for reactor normal operation and accident condition are set with reference to the ultimate strengths. Under irradiation, both ultimate strengths vary with neutron fluence and irradiation temperature. The present section reviews the ultimate strengths of H-451 and IG-110 grade graphites from a General Atomics Report⁴⁷ and a JAERI report²⁹. The fluence values for both dataset are converted to dpa unit. The original figures and the corresponding extracted numerical data can be found in appendices A and B.

Grade H-451 Graphite

A plot of the change in UTS with neutron fluence at various temperatures is given in Fig. 25.

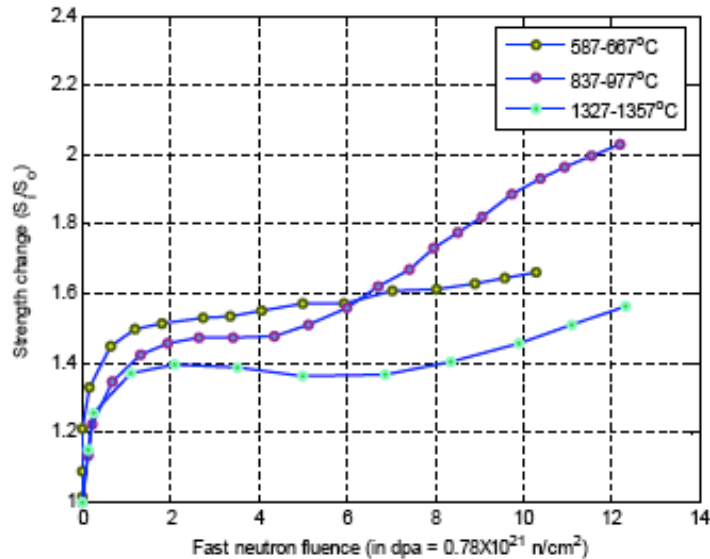


Figure 25. Rescaled UTS change data for H-451 graphite (original data taken from a General Atomics report⁴⁷).

As reported in General Atomics reports^{47,40}, the change in UTS due to neutron irradiation is related to the irradiation-induced change in modulus and for H-451 graphite grade and is given by Eq. 35.

$$\frac{S_i}{S_o} = \left(\frac{E_i}{E_o} \right)^{0.64} ; \quad (35)$$

where,

S_o = UTS of non-irradiated graphite;

S_i = UTS of irradiated graphite;

E_o = Young's modulus of non-irradiated graphite; and,

E_i = Young's modulus of irradiated graphite.

For compressive ultimate strength, since UCS of H-451 is almost four times its UTS, only UTS is needed in calculating the stress limits.

IG-110 Graphite

A plot of the change in UTS with neutron fluence at various temperatures is given in Fig. 26.

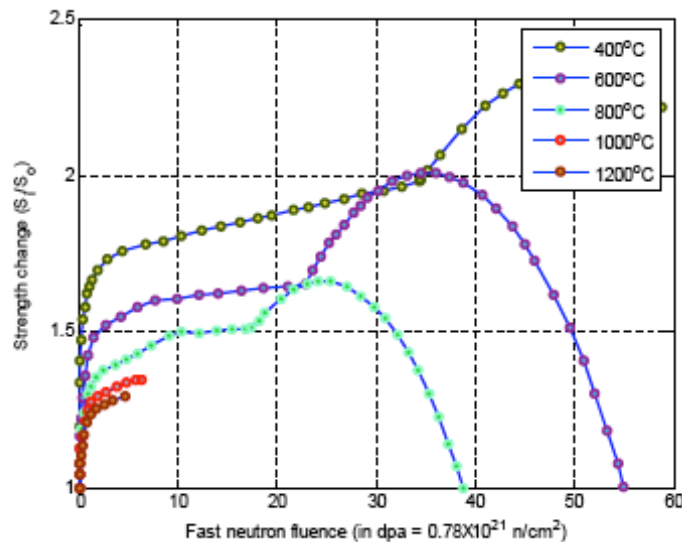


Figure 26. Rescaled UTS change data for IG-110 graphite (original data taken from JAERI report²⁹).

The empirical material model for strength change of IG-110 graphite as reproduced from JAERI report²⁹, is given in Eq. 36.

$$\frac{S_i}{S_o} = \left(\frac{E_i}{E_o} \right)^k \quad \text{or} \quad (36)$$

$$= (a\gamma + b)^k \quad ; \text{ for } \gamma \leq \gamma_c \quad ;$$

$$= [c(\gamma + d)^2 + e]^k \quad ; \text{ for } \gamma > \gamma_c$$

where,

γ = Fast neutron fluence ($\times 10^{26}$ n/m², E > 0.1 MeV);

γ_c = Fast neutron fluence at the beginning of high fluence region for the longitudinal Young's modulus ($\times 10^{26}$ n/m², E > 0.1 MeV) ;

k = constant 0.712;

S_o = UTS of non-irradiated graphite;

S_i = UTS of irradiated graphite;

E_o = Young's modulus of non-irradiated graphite;

E_i = Young's modulus of irradiated graphite;

$a\gamma + b$ = Longitudinal Young's modulus in the low fluence region (Table 17); and,

$c(\gamma + d)^2 + e$ = Longitudinal Young's modulus in the high fluence region (Table 17).

5.2.5 Irradiated Thermal Conductivity Change Material Data and Model

This property determines the temperature distribution in the graphite components. Irradiation rapidly reduces the thermal conductivity to a saturation level, which increases with increasing irradiation temperature. In this section, design curves for graphite grades H-451 and IG-110 are presented. The design curves are reproduced respectively from General Atomics Report⁴⁰ and JAERI report²⁹.

Grade H-451 Graphite

A plot of the change in thermal conductivity with neutron fluence at various temperatures is given in Fig. 27.

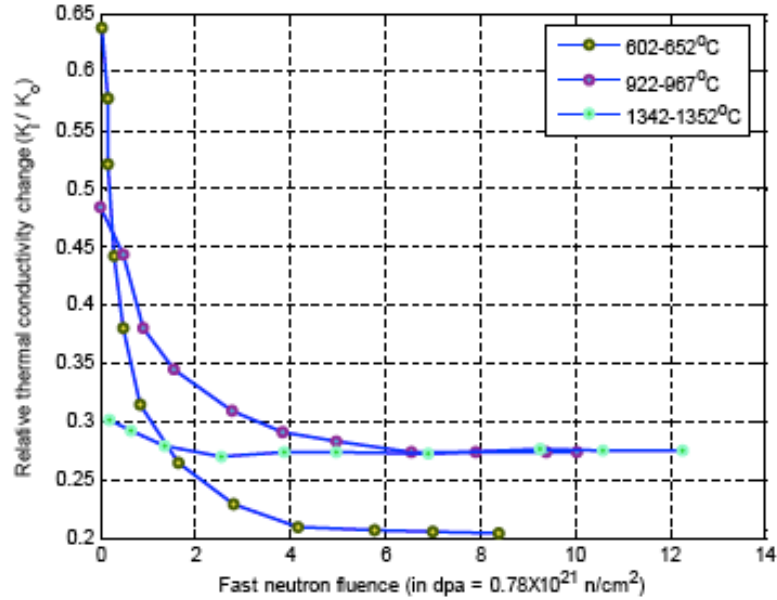


Figure 27. Rescaled thermal conductivity change data for H-451 graphite (original data taken from a General Atomics Handbook⁴⁰). Note: the thermal conductivity at non-irradiated condition (i.e. K_o) considered average of the against-grain (AG) and with-grain (WG) non-irradiated thermal conductivity as given in Table 11.

As reported in General Atomics reports^{47,40}, the change in thermal conductivity of H-451 graphite due to neutron irradiation is related to the neutron fluence by an equation of the form (Eq. 37).

$$\frac{K_i}{K_o} = f(\gamma(t, \Omega), \theta(t, \Omega)); \quad (37)$$

where:

K_o = Thermal conductivity of non-irradiated graphite;

K_i = Thermal conductivity of irradiated graphite;

$\gamma(t, \Omega)$ = time t and location Ω dependent fluence; and

$\theta(t, \Omega)$ = time t and location Ω dependent temperature.

The thermal conductivity data (Fig. 27) can be fitted with a 2nd order temperature and 7th order fluence polynomial as shown in Eq. 38.

$$\frac{K_i}{K_o} = f(\gamma(t, \Omega), \theta(t, \Omega))$$

$$= (A_{00} + A_{01}\theta + A_{02}\theta^2) + (A_{10} + A_{11}\theta + A_{12}\theta^2)\gamma$$

$$+ (A_{20} + A_{21}\theta + A_{22}\theta^2)\gamma^2 + (A_{30} + A_{31}\theta + A_{32}\theta^2)\gamma^3$$

$$+ (A_{40} + A_{41}\theta + A_{42}\theta^2)\gamma^4 + (A_{50} + A_{51}\theta + A_{52}\theta^2)\gamma^5$$

$$+ (A_{60} + A_{61}\theta + A_{62}\theta^2)\gamma^6 + (A_{70} + A_{71}\theta + A_{72}\theta^2)\gamma^7$$

; for $400 \leq \theta \leq 1350^\circ C$ & $\gamma \leq 12$; γ is in dpa unit

The values of the coefficients are tabulated in Table 18.

Table 18 Polynomial coefficients of relative thermal conductivity data on H-451.

$A_{i0}; i = 0, 2 \dots 7$	$A_{i1}; i = 0, 2 \dots 7$	$A_{i2}; i = 0, 2 \dots 7$
1.2319	-0.0010278	2.5195e-007
-4.9059	0.0084993	-3.6156e-006
5.6871	-0.010296	4.5042e-006
-3.1073	0.0056856	-2.5038e-006
0.89985	-0.00165	7.2777e-007
-0.14183	0.00025986	-1.1459e-007
0.011482	-2.1e-005	9.2519e-009
-0.00037346	6.8158e-007	-2.9994e-010

A comparison of the original data and the fitted data is shown in Fig. 28.

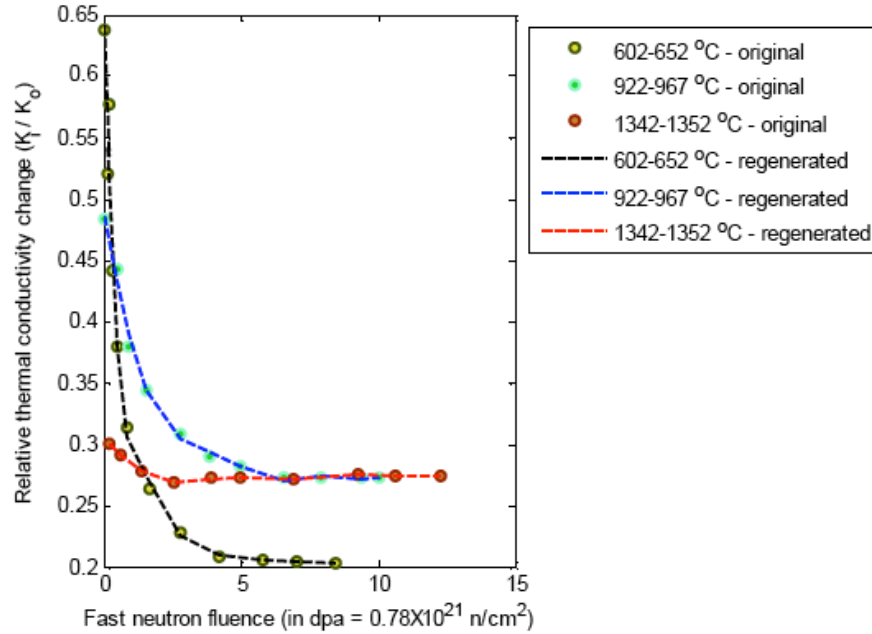


Figure 28. Original ~ fitted thermal conductivity change data for H-451.

IG-110 Graphite

A plot of the change in thermal conductivity with neutron fluence at various temperatures is given in Fig. 29. Note that the thermal conductivity initially reaches a plateau at low fluences, but decreases further at higher fluences.

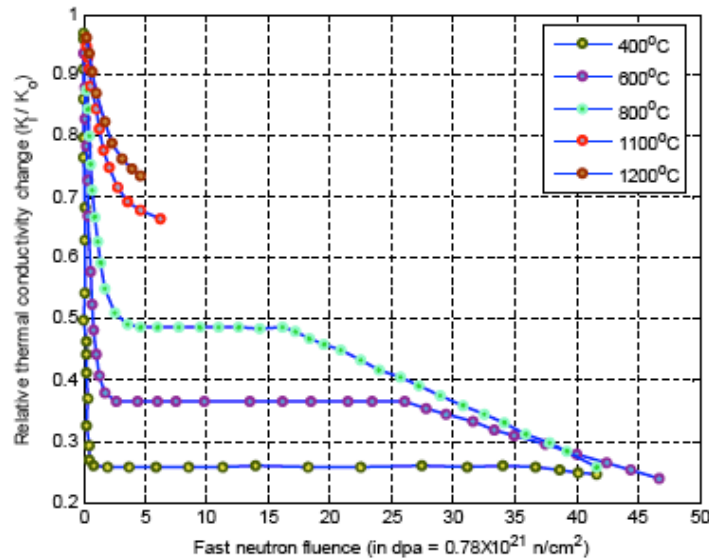


Figure 29. Rescaled thermal conductivity change data for IG-110 graphite (original data taken from JAERI report²⁹).

The empirical material model for thermal conductivity change of IG-110 graphite as reproduced from JAERI report²⁹, is given in Eq. 39.

$$\begin{aligned} \frac{K_i}{K_o} &= f(\gamma(t,\Omega),\theta(t,\Omega)) \\ &= \frac{K_s}{K_o} + \left(1 - \frac{K_s}{K_o}\right) \exp\left(\frac{-\gamma\theta}{\tau}\right) \quad ; \text{ for } \gamma \leq \gamma_{TA} ; \\ &= a_1\gamma + a_2 \quad ; \text{ for } \gamma > \gamma_{TA} \end{aligned} \tag{39}$$

where:

γ = Fast neutron fluence ($\times 10^{26}$ n/m², E > 0.1 MeV);

γ_{TA} = Fast neutron fluence at turn around point;

K_0 = Thermal conductivity before irradiation (W/m-K);

K_i = Thermal conductivity after irradiation (W/m-K);

τ = Constant (n/m²-°C); and,

a_1, a_2 = Temperature-dependent constants (Table 19).

Table 19. Polynomial coefficients a_1 and a_2 for thermal conductivity change material model as given in Eq. 39.

Grade	IG-110	
	a_1	a_2
Irradiatin Temperature (°C)		
400	-2.93×10^{-2}	3.75×10^{-1}
600	-7.94×10^{-2}	5.27×10^{-1}
800	-1.15×10^{-1}	6.34×10^{-1}

5.2.6 Effect of Water Vapor Oxidation on Irradiated Material Properties

Effect of irradiation on the changes in properties such as length, volume, bulk density, thermal conductivity, thermal expansion, electrical resistivity, and Young's modulus was studied for H-451 and IG-110 nuclear graphites, which were thermally oxidized by water vapor prior to irradiation.⁵⁰ The samples were irradiated at 800 – 1020 °C to a neutron fluence of 6.6×10^{24} n/m² (E > 29 fJ). The experimental results have shown that the irradiation-induced percentage changes of the properties were the same for both thermally oxidized and non-oxidized samples.

5.3 Semi-Empirical Material Models

Semi-empirical material models are more physics-based compared to pure empirical material models. The present section reviews a few semi-empirical material models that are available in open literature. Eason et.al. presented a material model based on Gilsocarbon graphite.⁵¹ They proposed an empirical model for Young's modulus of Gilsocarbon graphite when irradiated in an inert environment. As reported, the model can be used for graphite component stress analyses up to a fast neutron dose of 200×10^{20} n/cm² equivalent DIDO nickel dose (EDND) in the temperature range 300 – 650 °C. The proposed semi-empirical relation is given in Eq. 40.

$$\frac{E}{E_0} = P + A \left(\frac{DR}{B} \right)^{C-1} \exp \left\{ - \left(\frac{DR}{B} \right)^C \right\}. \quad (40)$$

In Eq. 40, E, E₀ respectively represent irradiated and non-irradiated Young's modulus, while P, A, B and C are functions of irradiation temperature, T_{irr} . Also dimensionless dose ratio (DR) is defined as the actual dose (EDND, n/cm² units) divided by the turnaround dose EDND_m.

In addition to semi-empirical type material model based on experimental data, few researchers have also proposed that finite element analysis can be used to generate data, which can be equivalent of experimental data. Once the required data are generated, an estimated parametric material model can be generated. For example, based on a simulated microstructure, Hall et al. presented a finite-element-based approach to simulate the Young's modulus and dimensional change material data for different irradiation dose and temperature.⁵² They assumed that the filler material behavior change was primarily responsible for the change in the polycrystalline material behavior. Thus, the filler particle was assigned irradiation dependent properties of highly annealed pyrolytic graphite (HAPG), but the binder was assigned non-irradiated properties of an isotropic graphite, such as Glisocarbon. The model was then subjected to loading conditions representative of those found in a thermal reactor.

6. IRRADIATED CREEP MATERIAL MODELS

The creep material properties data and models for H-451 and IG-110 graphite grades are discussed in this chapter. Note that although the theoretical structure for the multiaxial creep constitutive relations are well established, most of the material constants and parameters needed to carry out design analyses are based on limited uniaxial test data, which necessarily requires making ad hoc assumptions for their full determination. Extensive irradiation test programs will be needed to determine them to satisfy ASME Code or regulatory requirements.

6.1 H-451 Graphite

Price^{14,53} has reviewed all published irradiation induced creep data for graphites. Since then, Oak Ridge National Laboratory (ORNL) has published results from compressive creep tests at 600 and 900 °C at applied compressive stresses of 2,000 and 300 psi. Ho et al. have also reported results from tensile creep tests on H-451.⁵⁴ A set of irradiation creep parameters are presented in the General Atomics reports, which were estimated based on the creep data of all available graphite grades.^{14,55} Because of a lack of adequate documentation, it is difficult to reproduce the original data as given in the General Atomics reports. However, the creep equation derived for H-451 graphite is described below.

The total creep strain can be written as the sum of primary and secondary creep strain.

$$\varepsilon^c = \varepsilon^{pc} + \varepsilon^{sc}. \quad (41)$$

The primary creep strain rate $\dot{\varepsilon}^{pc}$ is given by

$$\begin{aligned} \dot{\varepsilon}^{pc} &= M^{pc} (\sigma - E^{pc} \varepsilon^{pc}) \\ &= M^{pc} \sigma - \frac{\varepsilon^{pc}}{\Psi_R^{pc}}. \end{aligned} \quad (42)$$

where, the primary creep matrix, M^{pc} , can be expressed in terms of the primary creep elastic modulus matrix, E^{pc} , as follows:

$$M^{pc} = \frac{1}{\Psi_R^{pc}} E^{pc-1}. \quad (43)$$

In Eqs. 41 - 43, for the transversely isotropic case, $(E^{pc})^{-1}$ is a symmetric matrix that is a function of the elastic moduli $E_x^{pc} (= E_y^{pc})$, E_z^{pc} and G_{xz}^{pc} at the time of loading or unloading.

$$\left(E^{pc}\right)^{-1} = \begin{bmatrix} \frac{1}{E_x^{pc}} & -\frac{\nu_{xy}^{pc}}{E_x^{pc}} & -\frac{\nu_{zx}^{pc}}{E_z^{pc}} & 0 & 0 & 0 \\ & \frac{1}{E_x^{pc}} & -\frac{\nu_{zx}^{pc}}{E_z^{pc}} & 0 & 0 & 0 \\ & & \frac{1}{E_z^{pc}} & 0 & 0 & 0 \\ & & & \frac{2(1+\nu_{xy}^{pc})}{E_x^{pc}} & 0 & 0 \\ & & & & \frac{1}{G_{xz}^{pc}} & 0 \\ & & & & & \frac{1}{G_{xz}^{pc}} \end{bmatrix} \quad (44)$$

Ψ_R^{pc} is the relaxation time, which for H-451 is given in Eq. 45.

$$\Psi_R^{pc} = 4 \times 10^{19} \text{ n/cm}^2 \text{ (Electron energy } > 0.18 \text{ Mev, HTGR).} \quad (45)$$

According to the graphite handbook, the primary creep Poisson's ratios are zero

$$\nu_{xy}^{pc} = \nu_{xz}^{pc} = \nu_{yz}^{pc} = 0. \quad (46)$$

For one-dimensional cases, M^{pc} , can be expressed as:

$$\begin{aligned} M^{pc} &= \frac{1}{\Psi_R^{pc}} E_o^{-1} \\ &= \frac{b}{E_o} ; \quad b = 2.5 \text{ for H-451 graphite} \end{aligned} \quad (47)$$

It is to be noted that originally Tsang and Marsden¹⁹ reported the primary creep strain equation as follows:

$$\epsilon^{pc} = a e^{-b\gamma} \int_0^{\gamma} \frac{\sigma}{E_o} e^{b\gamma'} d\gamma' ; \quad a = 1; \quad b = 4 \text{ for UK graphite} \quad (48)$$

The only difference between the UK grade graphite and H-451, is in the value of b.

In addition to the primary creep, the secondary creep equation for H-451 graphite can be found from the General Atomics reports⁴⁰.

$$\dot{\varepsilon}^{sc} = M^{sc} \sigma . \quad (49)$$

M^{sc} can be expressed in terms of the secondary creep elastic modulus matrix E^{sc} .

$$M^{sc} = \frac{1}{\Psi_R^{sc}} (E^{sc})^{-1} . \quad (50)$$

For the transversely isotropic case, $(E^{sc})^{-1}$ is a symmetric matrix, as given in Eq. 51.

$$(E^{sc})^{-1} = \begin{bmatrix} \frac{1}{E_x^{sc}} & -\frac{\nu_{xy}^{sc}}{E_x^{sc}} & -\frac{\nu_{zx}^{sc}}{E_z^{sc}} & 0 & 0 & 0 \\ & \frac{1}{E_x^{sc}} & -\frac{\nu_{zx}^{sc}}{E_z^{sc}} & 0 & 0 & 0 \\ & & \frac{1}{E_z^{sc}} & 0 & 0 & 0 \\ & & & \frac{2(1+\nu_{xy}^{sc})}{E_x^{sc}} & 0 & 0 \\ & & & & \frac{1}{G_{xz}^{sc}} & 0 \\ & & & & & \frac{1}{G_{xz}^{sc}} \end{bmatrix} ; \quad (51)$$

and,

$$\nu_{xy}^{sc} = \nu_{xz}^{sc} = \nu_{yz}^{sc} = 0.5 . \quad (52)$$

For one-dimensional tests, each conducted under constant stress and temperature,

$$\varepsilon^{sc} = \frac{\sigma}{E} (2.87128\gamma + 0.14853\gamma\theta - 2.48083\gamma^2 + 0.25992\gamma^2\theta + 0.44420\gamma^3 - 0.05671\gamma^3\theta) \quad (53)$$

for $\theta \geq 600^\circ\text{C}$ and $\gamma \leq 4.5$; γ is in $\times 10^{21} \text{ n / cm}^2$ unit

Tsang and Marsden¹⁹ used a linear secondary creep equation as follows:

$$\varepsilon^{sc} = k \int_0^\gamma \frac{\sigma}{E_c} d\gamma' ; k = 0.23, \quad \gamma \text{ is in } \times 10^{20} \text{ n / cm}^2 \text{ unit} . \quad (54)$$

In Eq. 54, the value of constant $k = 0.23$ possibly holds good for the particular graphite grade the UK group used. However, by comparing Eq. 53 with Eq. 54, the equivalent linear secondary creep equation for the H-451 graphite grade can be written as follows:

$$\varepsilon^{sc} = k \int_0^\gamma \frac{\sigma}{E_c} d\gamma' ; k = 0.287128, \quad \gamma \text{ is in } \times 10^{20} \text{ n / cm}^2 \text{ unit} . \quad (55)$$

The above creep model (Eq. 53) has been used to predict irradiation creep data for H-451 reported by Burchell⁵⁶, and the results are shown in Figs. 30 and 31. Figure 31 also shows data for radial creep. It appears that H-451 is nearly isotropic up to a fluence of 5×10^{21} n/cm².

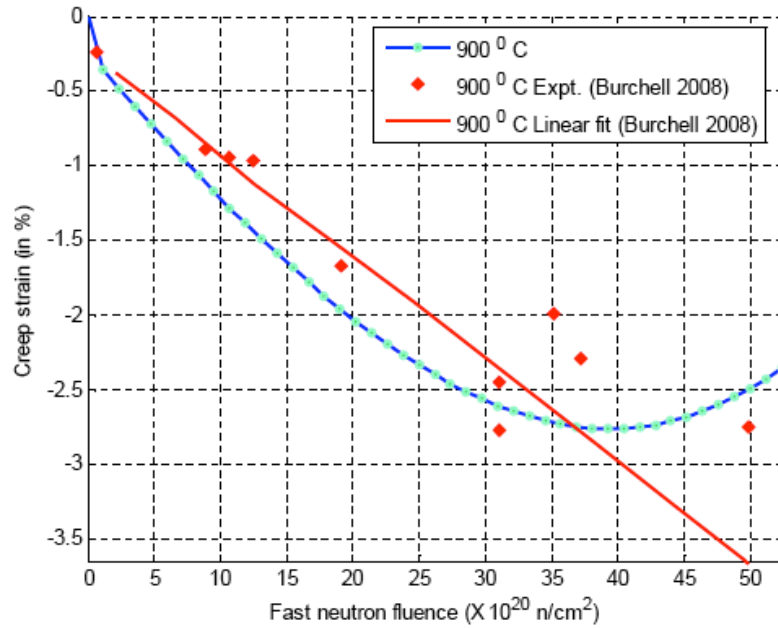


Figure 30. Axial creep strain for H-451 at 900 °C and 20.7 MPa compressive stress (Burchell⁵⁶).

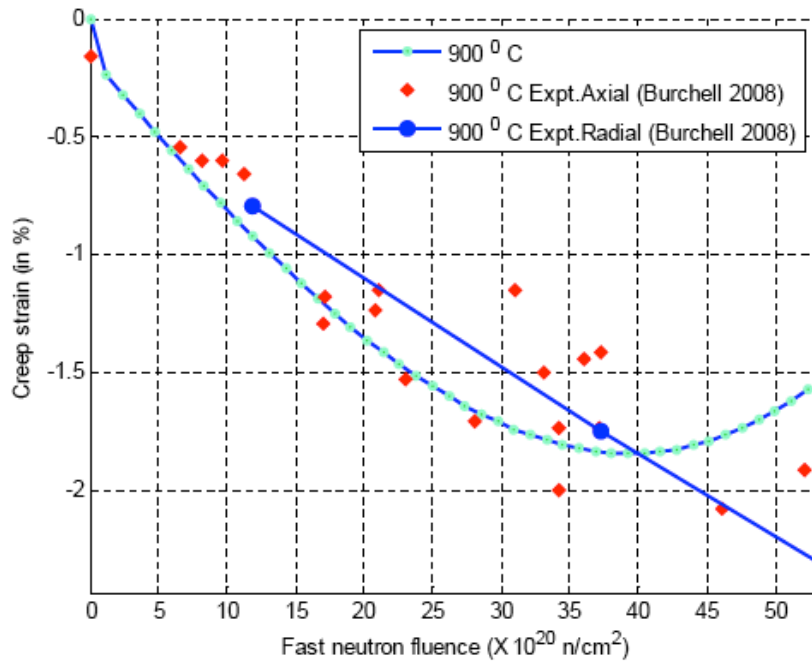


Figure 31. Axial and radial creep strains for H-451 at 900 °C and 13.8 MPa compressive stress (Burchell⁵⁶).

6.2 IG-110 Graphite

The JAERI report²⁹ includes a creep model for IG-110 graphite. According to the model, the total creep strain is given by

$$\begin{aligned}\varepsilon^c &= \varepsilon^{pc} + \varepsilon^{sc} \\ &= a \frac{\sigma}{E_0} [1 - e^{-b\gamma}] + K\sigma\gamma;\end{aligned}\tag{56}$$

where:

σ = Stress (MPa);

E_0 = Longitudinal Young's modulus (GPa) before irradiation;

γ = Fast neutron fluence ($\times 10^{26}$ n/m², $E > 0.1$ MeV);

a, b = Primary creep parameters; and,

K = Secondary creep coefficient ([MPa-n/m²]⁻¹).

Comparing the primary creep term in Eq. 56 with Eq. 42, it can be seen that the primary creep models reported in JAERI report and General Atomics report, 1988⁴⁰, have similar structure. However, comparing the secondary creep term in Eq. 56 with Eq. 53, it can be seen that unlike the nonlinear creep model given by the General Atomics report, the secondary creep model as reported in the JAERI report is a linear one. However, the secondary creep coefficient in Eq. 56 varies exponentially with temperature and for IG-110 grade is given as below:

$$K = 0.7163 e^{0.0012 \theta}.\tag{57}$$

The above temperature dependence of secondary creep coefficient was determined using the test results of IG-110 graphite (irradiation temperature of 600-1000 °C) along with the test results from other near-isotropic graphite grades. The data for creep coefficient are given in Appendix B.

6.3 Irradiated Creep Poisson's Ratio

Ideally the creep Poisson's ratio varies with the creep strain. Figure 6.3 shows the experimental data and curve fit showing the variation of Poisson's ratio with creep strain.

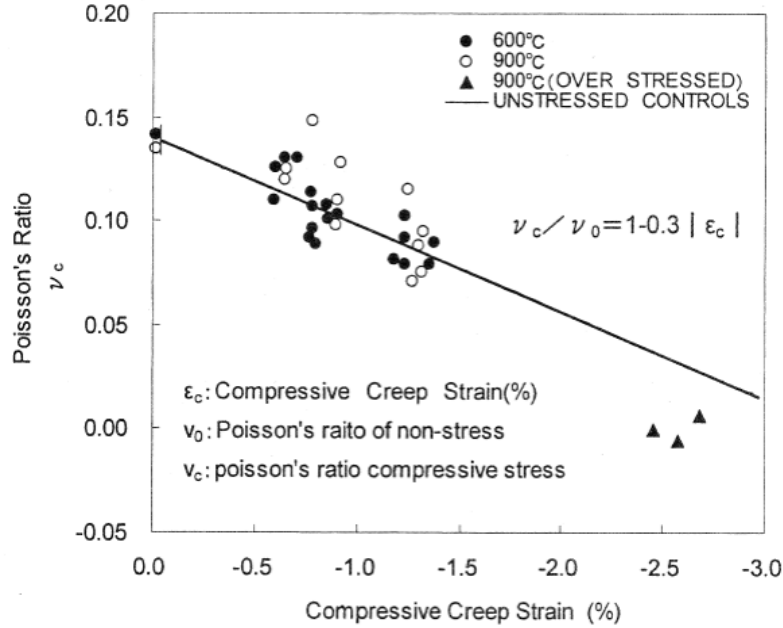


Figure 32. Dependency of Poisson's ratio of H-451 graphite on creep strain (by permission of JAERI²⁹).

In the JAERI report²⁹, it is not clear whether the given data (Refer Fig. 32) is along any particular direction of transversely isotropic H-451 graphite. However, the Graphite Handbook (General Atomics report)⁴⁰ assumes the creep coefficients along different directions are invariant and behave as isotropic material. This is due to two considerations. First, the creep data are insufficient to derive a set of values as a function of temperature and fluence in addition to direction. Secondly, and the more important one, is that the stress calculations are not sensitive to the creep Poisson's ratios. Based on the OC creep series, the following values are recommended in graphite handbook.

$$\begin{aligned}
 \text{Primary creep Poisson's ratio: } \nu_{xy}^{pc} &= \nu_{zx}^{pc} = \nu_{yz}^{pc} = 0 \\
 \text{Secondary creep Poisson's ratio: } \nu_{xy}^{sc} &= \nu_{zx}^{sc} = \nu_{yz}^{sc} = 0.5
 \end{aligned}
 \tag{58}$$

6.4 Irradiation Creep Interaction Effects

Recent mechanical and physical properties tests on irradiated and non-irradiated specimens, conducted in the U.K. appear to suggest that there is an interaction between irradiation induced creep strain and coefficient of thermal expansion and dimensional change strain.²⁴ For the present, we will assume that such an interaction effect between irradiation induced creep and thermal conductivity is negligible.

6.4.1 Effect of Creep Strain on Coefficient of Thermal Expansion

Creep strain of up to 4.5% does not significantly alter density, elastic modulus, defect size (hence sonic attenuation) and electrical resistivity of H-451 graphite.⁴⁰ Thermal expansion (CTE) is the only property known to be noticeably affected by a creep strain component.⁴⁰ The following relationship is obtained at 800 °C from axial specimens in a compression creep series:⁴⁰

$$\alpha_c = \alpha_i + \Delta\hat{\alpha}; \quad (59)$$

where:

$$\Delta\hat{\alpha} = \text{correction to CTE} = -0.504\varepsilon^c;$$

α_c = mean coefficient of thermal expansion a creep specimen with creep strain of ε_c ($10^{-6}/^\circ\text{C}$),

α_i = mean coefficient of thermal expansion of an unstressed control specimen irradiated under the same condition as the creep specimen ($10^{-6}/^\circ\text{C}$),

ε^c = creep strain, negative for compressive creep strain (%). The relationship is assumed to be applicable to compressive and tensile creep in the axial as well as radial directions.

For multiaxial cases, the correction to CTE is given by (assuming $T_{\text{Ref}}=20^\circ\text{C}$)¹⁹:

$$\Delta\hat{\alpha} = -0.504\varepsilon^{ec}. \quad (60)$$

where: ε^{ec} is the effective creep strain.

$$\varepsilon^{ec} = \begin{bmatrix} 1 & -0.5 & -0.5 \\ -0.5 & 1 & -0.5 \\ -0.5 & -0.5 & 1 \end{bmatrix} \begin{Bmatrix} \varepsilon_1^c \\ \varepsilon_2^c \\ \varepsilon_3^c \end{Bmatrix}. \quad (61)$$

The incremental interaction thermal strain is approximately given by:

$$\Delta\varepsilon^{i\theta} = \Delta\alpha_i(T - 20) + \Delta\hat{\alpha}\Delta T. \quad (62)$$

6.4.2 Effect of Creep Strain on Dimensional Change Strain

It has been shown that the CTE has influence on the dimensional change strain due to irradiation.^{24,40} Therefore, creep strain may be expected to modify the dimensional change. Kelly and Burchell⁵⁷ proposed an interaction dimensional change strain, defined as

$$\varepsilon^{idc} = \int_0^\gamma \left(\frac{\Delta \hat{\alpha}}{\alpha_{crystal}^c - \alpha_{crystal}^a} \right) \frac{dX_T}{d\gamma} d\gamma'. \quad (63)$$

$\alpha_{crystal}^c$ and $\alpha_{crystal}^a$ are the crystal CTEs in the crystal c and a direction, respectively. The function X_T is called the shape factor for the graphite crystallite, which is given by the difference in the crystallite dimensional change in the 'a' and 'c' directions and defined as:

$$X_T = \frac{\Delta X_c}{X_c} - \frac{\Delta X_a}{X_a}, \quad (64)$$

where, X_c is a function of irradiation temperature and fast neutron fluence and has been obtained from irradiation experiments on highly orientated pyrolytic graphite (HPOG). Hence the crystal shape term $dX_T/d\gamma$ can be found and the incremental equation for Eq. (63) can be calculated using:

$$\Delta \varepsilon^{idc} = \left(\frac{\Delta \hat{\alpha}}{\alpha_{crystal}^c - \alpha_{crystal}^a} \right) \frac{dX_T}{d\gamma} \Delta \gamma. \quad (65)$$

The parameter X_T has been evaluated for H-451 at irradiation temperatures of 600 °C and 900 °C from dimensional change and Young's modulus data⁵⁷.

The parameter X_T may be written as a quadratic function of neutron dose for irradiation temperatures 600 °C and 900 °C, as given in Eqs. 66 - 67, respectively.⁵⁶

$$X_T = 0.0431\gamma^2 + 0.0686\gamma; \quad (66)$$

and

$$X_T = 0.1315\gamma^2 + 0.2399\gamma, \quad (67)$$

where, γ is in units of 10^{22} n/cm² [E > 50 keV].

7. PROPOSED STRESS ANALYSIS CODE AND APPROACH

A general purpose finite element (FE) procedure will be developed for the stress analysis of HTGR graphite core components. The finite element model will be based on the ABAQUS commercial software. The temperature, irradiation fluence and irradiation creep dependant material properties of graphite, which are therefore time-dependent and location-dependent, will be incorporated into ABAQUS through the use of the user subroutines (UMAT).

However, to solve the problem of stress analysis of HTGR graphite core components rigorously, we would need to adopt a coupled fluid dynamics-structural analysis technique. Conducting such an analysis scheme involves complex multi-physics iterative and interactive calculations, which are time-consuming, and would require coupling ABAQUS with a computational fluid dynamics (CFD) code, like Fluent. Because of budget and time constraints, we have decided *a-priori* to decouple fluid dynamics/thermal hydraulics analysis from thermal conduction/stress analysis. In this approach, we will not take into account the interactive effect of deformation of the coolant channels due to stress/irradiation creep and thermal hydraulics during the course of the analysis time. Instead, we will consider several configurations of the core assembly geometry; one corresponding to the initial geometry, one corresponding to the end of design life geometry and possibly another corresponding to the geometry at midlife. We will obtain the thermal hydraulics analysis results for each of the three configurations and carry out the heat conduction and stress analyses assuming that the thermal hydraulics inputs (e.g., heat transfer coefficients and coolant temperature) do not change with time during the course of the analysis time. The results from each of the three analyses will have to be combined in order to ensure that ASME code requirements (limits on stress, strain and deformation) are satisfied at all times.

Also, we assume that results from a parallel analysis of oxidation of the HTGR core components will be available so that any degradation of mechanical properties can be taken into account.

7.1 Analysis Steps

Step 1: At time $t+\Delta t$, obtain from a neutronics analysis the neutron dose as a function of time and core location

$$\gamma_{t+\Delta t} = f_1(t + \Delta t, \Omega), \quad (68)$$

where, Ω denotes the core location. From a parallel thermal hydraulics analysis obtain the temperature field symbolically represented as follows:

$$\theta_{t+\Delta t} = f_2(\gamma_{t+\Delta t}, k_{t+\Delta t}), \quad (69)$$

where, k denotes the thermal conductivity (function of temperature and fluence).

Compute the average fluence and average temperature during the step and use them to determine the values of the physical and mechanical properties of graphite.

Step 2: At time $t+\Delta t$, estimate the incremental thermal strain given in functional form as follows:

$$\Delta \varepsilon_{t+\Delta t}^{\theta} = f_3(\alpha_{avg}, \theta_{avg}), \quad (70)$$

where, α_{avg} is the average coefficient of thermal expansion (CTE) during the time interval $t + \Delta t$ and is a function of the average temperature θ_{avg} and average dose γ_{avg} during the time step. Similarly, estimate the incremental dimensional change strain, which can be expressed in a functional form as follows:

$$\Delta \varepsilon_{t+\Delta t}^{dc} = f_4(\gamma_{avg}, A_0(\theta_{avg}), A_1(\theta_{avg}), A_3(\theta_{avg}), \dots), \quad (71)$$

where, $A_i(\theta_{avg})$; $i = 0, 1, 2, \dots$ are temperature-dependent parameters.

Step 3 (predictor): Estimate the incremental primary creep strain $\Delta \varepsilon_{t+\Delta t}^{pc}$, secondary creep strain $\Delta \varepsilon_{t+\Delta t}^{sc}$, elastic strain $\Delta \varepsilon_{t+\Delta t}^e$ and stress $\Delta \sigma_{t+\Delta t}$ by solving the following four equations ignoring the interaction strain terms,

$$\Delta \varepsilon_{t+\Delta t}^{pc} = (M_{avg}^{pc} \sigma_t - \frac{\varepsilon_t^{pc}}{\Psi_R}) \Delta \gamma_{t+\Delta t}; \quad (72)$$

$$\Delta \varepsilon_{t+\Delta t}^{sc} = M_{avg}^{sc} \sigma_t \Delta \gamma_{t+\Delta t}; \quad (73)$$

$$\Delta \varepsilon_{t+\Delta t}^{total} = \Delta \varepsilon_{t+\Delta t}^e + \Delta \varepsilon_{t+\Delta t}^{\theta} + \Delta \varepsilon_{t+\Delta t}^{pc} + \Delta \varepsilon_{t+\Delta t}^{sc} + \Delta \varepsilon_{t+\Delta t}^{dc}; \text{ and} \quad (74)$$

$$\Delta \sigma_{t+\Delta t} = D_{t+\Delta t}^{el} \Delta \varepsilon_{t+\Delta t}^e + \Delta D_{t+\Delta t}^{el} \varepsilon_{t+\Delta t}^e, \quad (75)$$

where, $M_{t+\Delta t}^{pc}$ and $M_{t+\Delta t}^{sc}$ are, respectively, the primary and secondary creep material matrices, $D_{t+\Delta t}^{el}$ is the elastic material matrix, all are functions of the creep related constants and the dynamic Young's modulus $E_{t+\Delta t}^d$, which is a function of the average temperature and average fluence. Once $\Delta \sigma_{t+\Delta t}$ and the other increments are determined, their values at time at time $t + \Delta t$ can be obtained from:

$$\sigma_{t+\Delta t} = \sigma_t + \Delta \sigma_{t+\Delta t}; \quad (76)$$

$$\varepsilon_{t+\Delta t}^e = \varepsilon_t^e + \Delta \varepsilon_{t+\Delta t}^e; \quad (77)$$

$$\varepsilon_{t+\Delta t}^c = \varepsilon_{t+\Delta t}^{pc} + \varepsilon_{t+\Delta t}^{sc} = (\varepsilon_t^{pc} + \Delta \varepsilon_{t+\Delta t}^{pc}) + (\varepsilon_t^{sc} + \Delta \varepsilon_{t+\Delta t}^{sc}); \quad (78)$$

$$\varepsilon_{t+\Delta t}^{\theta} = \varepsilon_t^{\theta} + \Delta \varepsilon_{t+\Delta t}^{\theta}; \text{ and,} \quad (79)$$

$$\varepsilon_{t+\Delta t}^{dc} = \varepsilon_t^{dc} + \Delta \varepsilon_{t+\Delta t}^{dc}. \quad (80)$$

Step 4 (corrector): The corrector step first calculates the incremental interaction thermal strain, $\Delta\varepsilon^{i\theta}$, and incremental interaction dimensional change strain, $\Delta\varepsilon^{idc}$, based on the calculated creep strains during the predictor step. Also, calculate the average stress, average elastic strain and average creep strain values during the time step. Calculate the next iterative values of the incremental primary creep strain $\Delta\varepsilon_{t+\Delta t}^{pc}$, secondary creep strain $\Delta\varepsilon_{t+\Delta t}^{sc}$, elastic strain $\Delta\varepsilon_{t+\Delta t}^e$ and stress $\Delta\sigma_{t+\Delta t}$ by solving the following four equations:

$$\Delta\varepsilon_{t+\Delta t}^{pc} = \left(M_{avg}^{pc} \sigma_{avg} - \frac{\varepsilon_{avg}^{pc}}{\Psi_R} \right) \Delta\gamma_{t+\Delta t}; \quad (81)$$

$$\Delta\varepsilon_{t+\Delta t}^{sc} = M_{avg}^{sc} \sigma_{avg} \Delta\gamma_{t+\Delta t}; \quad (82)$$

$$\Delta\varepsilon_{t+\Delta t}^{total} = \Delta\varepsilon_{t+\Delta t}^e + \Delta\varepsilon_{t+\Delta t}^\theta + \Delta\varepsilon_{t+\Delta t}^{pc} + \Delta\varepsilon_{t+\Delta t}^{sc} + \Delta\varepsilon_{t+\Delta t}^{dc} + \Delta\varepsilon^{i\theta} + \Delta\varepsilon^{idc}; \text{ and,} \quad (83)$$

$$\Delta\sigma_{t+\Delta t} = D_{avg}^{el} \Delta\varepsilon_{t+\Delta t}^e + \Delta D_{t+\Delta t}^{el} \varepsilon_{avg}^e. \quad (84)$$

Once $\Delta\sigma_{t+\Delta t}$ and the other increments are determined, their values at time at time $t + \Delta t$ can be obtained from:

$$\sigma_{t+\Delta t} = \sigma_t + \Delta\sigma_{t+\Delta t}; \quad (85)$$

$$\varepsilon_{t+\Delta t}^e = \varepsilon_t^e + \Delta\varepsilon_{t+\Delta t}^e; \quad (86)$$

$$\varepsilon_{t+\Delta t}^c = \varepsilon_{t+\Delta t}^{pc} + \varepsilon_{t+\Delta t}^{sc} = (\varepsilon_t^{pc} + \Delta\varepsilon_{t+\Delta t}^{pc}) + (\varepsilon_t^{sc} + \Delta\varepsilon_{t+\Delta t}^{sc}); \quad (87)$$

$$\varepsilon_{t+\Delta t}^\theta = \varepsilon_t^\theta + \Delta\varepsilon_{t+\Delta t}^\theta + \Delta\varepsilon^{i\theta}; \text{ and,} \quad (88)$$

$$\varepsilon_{t+\Delta t}^{dc} = \varepsilon_t^{dc} + \Delta\varepsilon_{t+\Delta t}^{dc} + \Delta\varepsilon^{idc}. \quad (89)$$

The process (step 4) is repeated until convergence is achieved.

7.2 Direct Matrix Inversion Method

If the interaction strain terms are ignored, a direct matrix inversion approach, instead of the iterative approach, can be implemented to compute $\Delta\sigma$, as follows:

$$\Delta\varepsilon = \Delta\varepsilon^e + \Delta\varepsilon^{sc} + \Delta\varepsilon^{pc} + \Delta\varepsilon^\theta + \Delta\varepsilon^{dc} \quad (90)$$

Using the expressions for various strain increments and using average values of material constants,

$$\Delta \varepsilon = M^{el} \Delta \sigma + M^{sc} (\sigma_t + \Delta \sigma / 2) \dot{\gamma} \Delta t + \Delta \varepsilon^\theta + \Delta \varepsilon^{dc} + \left[M^{pc} (\sigma_t + \Delta \sigma / 2) - \frac{1}{\psi_R^{pc}} \varepsilon^{pc} \right] \dot{\gamma} \Delta t \quad (91)$$

where, M^{el} is the inverse of the elasticity matrix D^{el} . Collecting terms multiplying $\Delta \sigma$ on one side and solving for $\Delta \sigma$,

$$\Delta \sigma = \left[M^{el} + M^{sc} \dot{\gamma} \Delta t + M^{pc} \dot{\gamma} \Delta t / 2 \right]^{-1} \left[\Delta \varepsilon - (M^{sc} + M^{pc}) \sigma_t \dot{\gamma} \Delta t - \Delta \varepsilon^\theta - \Delta \varepsilon^{dc} + \frac{1}{\psi_R^{pc}} \varepsilon^{pc} \dot{\gamma} \Delta t \right] \quad (92)$$

The incremental primary and secondary creep strains are

$$\Delta \varepsilon^{pc} = \left[M^{pc} (\sigma_t + \Delta \sigma / 2) - \frac{1}{\psi_R^{pc}} \varepsilon^{pc} \right] \dot{\gamma} \Delta t \quad (93)$$

and

$$\Delta \varepsilon^{sc} = M^{sc} (\sigma_t + \Delta \sigma / 2) \dot{\gamma} \Delta t \quad (94)$$

The Jacobian $\frac{\partial \sigma}{\partial \varepsilon}$, which is required to be passed to the subroutine UMAT, is given by

$$\frac{\partial \sigma}{\partial \varepsilon} = \left[M^{el} + M^{sc} \dot{\gamma} \Delta t + M^{pc} \dot{\gamma} \Delta t / 2 \right]^{-1} \quad (95)$$

8. CONCLUSIONS

We conducted review and evaluation of currently known information on the subject of HTGR graphite core stress analysis models and procedures, including input material data through established relationships for various graphite classes that are intended for use in NGNP HTGR graphite core components. The properties data search for finite-element analysis assessment included the followings:

- a) Non-irradiated Properties:
 - i. Young's modulus versus temperature
 - ii. Elastic Poisson's ratio
 - iii. Coefficient of thermal expansion (CTE) versus temperature
 - iv. Thermal conductivity versus temperature
- b) Irradiated properties as a function of temperature and irradiation dose
 - v. Dimensional Change
 - vi. CTE
 - vii. Young's modulus
 - viii. Elastic Poisson's ratio
 - ix. Thermal conductivity
- c) Irradiation creep as a function of temperature, dose, and stress
 - x. Creep law constants and variables
 - xi. Poisson ratio in creep
- d) Effect of oxidation on graphite mechanical properties
- e) Interaction between Irradiation creep and thermal expansion and dimensional change strains

Significant data were collected for graphite grades H-451 and IG-110. However, the grade of graphite chosen for NGNP is different and its properties are currently being measured and not yet available.

The finite element code ABAQUS was chosen for conducting the heat conduction and stress analyses of graphite core components. A procedure has been developed to incorporate the graphite properties into the ABAQUS code. A user defined subroutine UMAT is being implemented for taking into account the interactive thermal and dimensional change strains due to irradiation creep.

REFERENCES

1. McCullough, C. R.; Staff, Power Pile Division, "*Summary Report on Design and Development of High Temperature Gas-Cooled Power Pile*", Clinton Laboratories (now Oak Ridge National Laboratory), Oak Ridge, TN, USA 1947.
2. **GA-A14297**, Kohler, E.J., Steward, K. P., and Iacono, J.V., "Peach Bottom HTGR Decommissioning and Component Removal." P. 42 in Proceedings of the American Nuclear Society Reactor Operation Division Conference, Chattanooga, TN, American Nuclear Society, LaGrange Park, IL, July 1977.
3. **INEEL/EXT-03-00103**, Kingrey, K. I., "Fuel Summary for Peach Bottom Unit 1 High-Temperature Gas-Cooled Reactor Cores 1 and 2", Idaho National Engineering and Environmental Laboratory Bechtel BWXT, Idaho, 2003.
4. **NUREG-1769**, "Safety Evaluation Report Related to the License Renewal of Peach Bottom Atomic Power Station, Units 2 and 3", Nuclear Regulatory Commission, 2003.
5. Moses, D. L. and Lanning, W. D., "*Analysis and evaluation of recent operational experience from the Fort St. Vrain HTGR*", IAEA specialists' meeting on gas cooled reactors, Oak Ridge, TN, USA, 1985.
6. David L. Moses, "Lessons Learned from Supporting NRC Licensing and Regulatory Activities for Fort St. Vrain (FSV) and from Supporting the NRC Pre-Application Licensing Review of the Modular HTGR", High Temperature Gas-Cooled Reactor Knowledge Management White Paper, Oak Ridge National Laboratory, March 2006.
7. **GA-AI9152**, "MHTGR: New Production Reactor Summary of Experience Base", General Atomics Company CA, March, 1988.
8. Simon, R., "*The Primary Circuit of the Dragon High Temperature Reactor Experiment*", Proc. 18th International Conference on Structural Mechanics in Reactor Technology, August 2005.
9. **Report Jü l-4275**, Moormann, R., "A Safety Re-evaluation of the AVR Pebble Bed Reactor Operation and its Consequences for Future HTR Concepts", Jü lich Forschungszentrum, 2008.
10. <http://www.jaea.go.jp/jaeri/english/ff/ff43/randd01.html> (last cited 2010).
11. Zhang, Z., Wu, Z., Wang, D., Xu, Y., Sun, Y., Li, F. and Dong, Y., "*Current status and technical description of Chinese 2 x 250 MWth HTR-PM demonstration plant*", Journal of Nuclear Engineering and Design, vol. 239, no7, pp. 1212-1219, 2009.
12. **Generation IV International Forum Annual Report, 2007** (http://www.gen-4.org/PDFs/annual_report2007.pdf)

13. **INL/EXT-07-13165**, Windes, W., Burchell, T. and Bratton, R. "Graphite Technology Development Plan", Idaho National Laboratory, Idaho Falls, ID, 2007.
14. **GA-A16402**, Price, R.J., "Review of Irradiation-Induced Creep in Graphite: A Review," General Atomics Company, CA, 1981..
15. **GA-A-16978**, Smith, P.D.and Pelessone, D., "Consistent Linearization Method for Finite-Element Analysis of Viscoelastic Materials", General Atomics Company CA, 1983.
16. Iyoku, T., Ishihara M. and Shirai, H., "Development of Thermal/Irradiation Stress Analytical Code "VIENUS" for HTTR Graphite Block," Journal of Nuclear Science and Technology, Vol. 28, No. 10, pp. 921-931, 1991.
17. **AEAT-5726**, Slater, I.J., Jones, C.J., Davies, M.A., "ABAQUS User Material Subroutine (UMAT) for Isotropic Graphite. Version 6.0, User Guide", July, 1999.
18. Li, H., B. J. Marsden and Fok, S. L., "*Relationship between nuclear graphite moderator brick bore profile measurement and irradiation-induced dimensional change*", Nuclear Engineering and Design 232 237–247, 2004.
19. Tsang, D K L., and Marsden B J, "*The development of a stress analysis code for nuclear graphite components in gas-cooled reactors*", Journal of Nuclear Materials.; 350(3), March, 2006.
20. Lejeail, Y.and Cabrillat, M.T., "Calculation Of Thermal Stresses In Graphite Fuel Blocks",18th International Conference On Structural Mechanics In Reactor Technology (Smirt 18), Beijing, China, August 7-12, 2005, Smirt18-W101-3.
21. Verpeaux P., Charras T. et Millard A., 1988, CASTEM 2000 une approche moderne du calcul desstructures, in « Calcul des structures et intelligence artificielle », Fouet J.M., Ladevèze P., Ohayon R., Eds, Pluralis, pp. 261-271, 1988.
22. Wang H. and Yu, S.,"*Uncertainties of creep model in stress analysis and life prediction of graphite component*", Journal of Nuclear Engineering and Design, Vol. 238, No. 9, pp. 2256-2260, September 2008.
23. **INL/EXT-09-15868**, Bratton, R. L.,"Modeling Mechanical Behavior of a Prismatic Replaceable Reflector Block", Idaho National Laboratory, Idaho Falls, ID., April 2009.
24. Marsden, B.J., Fok, S. L., and Li H., "*Irradiation behavior and structural analysis of HTR/VHTR graphite core components*" 18th International Conference on Structural Mechanics in Reactor Technology (SMiRT 18) Beijing, China, August 7-12, 2005.
25. Li H, Fok S L, and Marsden B J., "*An analytical study on the irradiation-induced stresses in nuclear graphite moderator bricks*". Journal of Nuclear Materials. Vol. 372. No. 2-3 pp. 164-170, 2008.

26. **LA-2486**, J.C. Rowley and J. B. Payne, "Steady-State Temperature Solution for a Heat-generating Circular Cylinder Cooled by a Ring of Equal Holes," Los Alamos Scientific Laboratory, NM 1961.
27. **INL/EXT-05-00552**, Bratton, R. L., "Status of ASME Section III Task Group on Graphite Core Support Structures", Idaho National Laboratory, Idaho Falls, ID,, August 2005.
28. **ASME Boiler and Pressure Vessels Code, Section III, Division 5, Subsection HA, Subpart B and Subsection HH, 2011.**
29. **JAEA Research 2009-042**, Shibata, T., Eto, M., Kunimoto, E., Shiozawa, S., Sawa, K., Oku T., and Maruyama, T., "Draft Of Standard For Graphite Core Components In High Temperature Gas-Cooled Reactor", JAEA, 2009 (<http://jolissrch-inter.tokai-sc.jaea.go.jp/pdfdata/JAEA-Research-2009-042.pdf>).
30. **INL/EXT-09-17187**, "NGNP High Temperature Materials White Paper", Idaho National Laboratory, Idaho Falls, ID, June 2010.
31. Tak, N. I., Kim, M. H., Lee, W. J., "*Numerical investigation of a heat transfer within the prismatic fuel assembly of a very high temperature reactor*", Annals of Nuclear Energy Vol. 35, No. 10, pp.1892–1899, 2008.
32. Sterbentz, J. W., "*Calculated Neutron and Gamma-Ray Spectra Across the Prismatic Very High Temperature Reactor Core*", 13th International Symposium on Reactor Dosimetry, Amsterdam, Netherlands May 2008 (<http://www.inl.gov/technicalpublications/Documents/4192208.pdf>).
33. **INL/EXT-09-16882**, Johnson, R. W., Sato, H., and Schultz, R. R. "CFD Analysis of Core Bypass Phenomena", Idaho National Laboratory, Idaho Falls, ID, 2009.
34. *Graphite and Precursors*, Edited by Delhaes, P., Gordon and Beach Science Publishers, Amsterdam, Netherlands, 2001.
35. Burchell, T., Yahr, T. and Battiste, R., "*Modeling the multiaxial strength of nuclear graphite*" Carbon, Vol. 45, No. 13, pp. 2570-2583, November 2007.
36. Burchell, T. D., Snead, L. L., "*The effect of neutron irradiation damage on the properties of grade NBG-10 graphite*", Journal of Nuclear Materials, Vol. 371, No. 1-3, pp.18–27, 2007.
37. **WAGR/TC/P(78)21**, Blanchard A. and Fitzgerald B., "The Air Reactivity of WAGR Moderator and Sleeve Graphites", UKAEA Report, UK, 1978.
38. **EUR—3900, THTR—44**, Stolz, Von E. and Werner, F. L. ,"*Kohlenstofftransport in den Hoch-temperaturreaktoren THTR und AVR*," Brown Boveri/Krupp Reaktorbau Report pp. 99-103, G.m.b.H., Mannheim, Germany, January 1968. (http://www.osti.gov/energycitations/product.biblio.jsp?osti_id=4523300)

39. **D. P. Report 332**, Pointud, M. L., Karcher, W., Pollitt, N. and Lothe, J., "Catalytic Influence of Different Metals on Corrosion Rate of Graphite," Dragon Project Report, CONF-641031-8 April 15, 1965 Atomic Energy Establishment. Winfrith, UK (Presented at the Symposium on Basic Research at A.E.R.E. Harwell, Oct. 19-21, 1964). http://www.osti.gov/energycitations/product.biblio.jsp?osti_id=4119918
40. **DOE-HTGR-88111**, Graphite Design Handbook, General Atomics Company, CA, 1988.
41. **JAERI-M8848 and 9166**, Eto, M., Kurosawa, T., Imai, H., Nomura, S., and Oku, T., "Estimation Of Graphite Materials Corrosion with Water-Vapor in Coolant of the VHTR and Oxidation Effect on the Materials Properties," IAEA Specialists Meeting on Graphite Component Design, Sept. 8-11, 1986, Vienna, Austria.
42. Seldin, E. J., "Stress-Strain Properties of Polycrystalline Graphites in Tension and Compression at Room Temperature," Carbon, Vol. 4, pp. 177-191, 1966.
43. R. Taylor et al., "The Mechanical Properties of Graphite," Carbon, Vol. 5, pp. 519-531, 1967.
44. Virgil'ev, Y. S. and Kalyagina, I.P. "*Reactor graphite*", Inorganic Materials Journal, Vol. 39, No. 1, pp. S46-S58, 2003.
45. **INL/EXT-08-15087**, NGNP Monthly Report, Idaho National Laboratory, Idaho Falls, ID, July, 2009.
46. Jenkins, G. M., "*Analysis of the Stress-Strain Relationships in Reactor Grade Graphite*", British Journal of Applied Physics, Vol. 13, pp. 30-32, 1962.
47. **GA-AI3089**, Price, R. J. and Beavan, L. A., "Final Report on Graphite Irradiation Test OG-1," General Atomics Company, CA, 1974.
48. **GA-AI3556**, Price, R. J. and Beavan, L. A., "Final Report on Graphite Irradiation Test OG-2," General Atomics Company, CA, 1975.
49. **GA-AI4211**, Price, R. J. and Beavan, L. A., "Final Report on Graphite Irradiation Test OG-3," General Atomics Company, CA, 1977.
50. Matsuo, H., Fulli, K. and Hisashi, I, "*Irradiation-Induced Property Changes of Thermally Oxidized Nuclear Graphites*," Journal of Nuclear Materials 152, 283-288 North-Holland, Amsterdam, 1988.
51. Eason, E. D., Hall, G N, Marsden B J, Heys, G B., "*Development of a Youngs modulus model for Gilsocarbon graphites irradiated in inert environments*". Journal of Nuclear Materials. Vol. 381. No. 1-2. pp 145-151, 2008.
52. Hall, G., Marsden, B. J. and Fok, S. L., "*The microstructural modelling of nuclear grade graphite*", Journal of Nuclear Materials, Vol. 353, No. 1-2, pp. 12-18, July 2006.

53. **GA-A12332**, Price, R. J., "Review of Irradiation-Induced Creep in Graphite Under HTGR Conditions," General Atomics Company, CA, 1972.
54. **DOE-HTGR-88097/0**, Ho, F. H., "H-451 Irradiation Creep Design Model"; General Atomics Company, CA, 1988.
55. **GA-AL4690**, Engle, G. B., "Assessment of grade H-451 Graphite for replaceable fuel and reflector elements in HTGR," General Atomics Company, CA, 1977.
56. Burchell, T. D., "*Irradiation induced creep behavior of H-451 graphite*", Journal of Nuclear Materials, Vol. 381, No. 1-2, pp. 46–54, 2008.
57. Kelly, B.T. and Burchell, T.D., "The Analysis of Irradiation Creep Experiments on Nuclear Reactor Graphite ," Journal of Carbon Vol. 32, No. 1, pp. 119-125, 1994.

APPENDIX A GRADE H-451 GRAPHITE PROPERTIES DATA

A1 Dimensional Change Strain

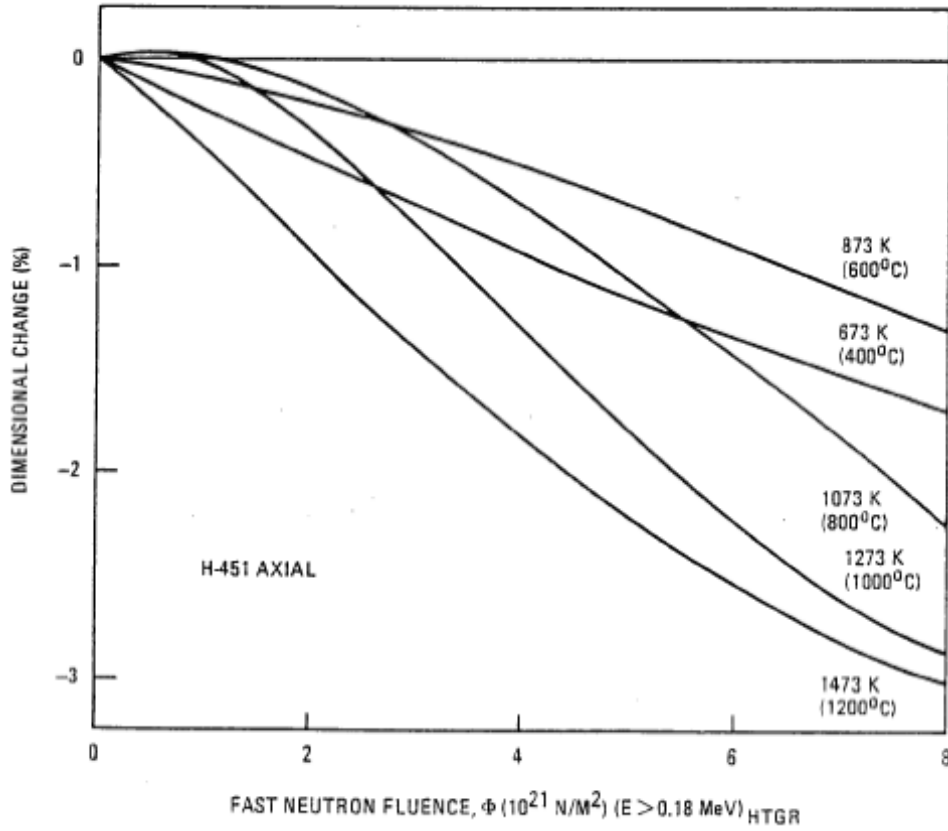


Figure A1 Design curves for dimensional change of H-451 graphite, axial orientation, as a function of irradiation conditions (General Atomics report⁴⁰)

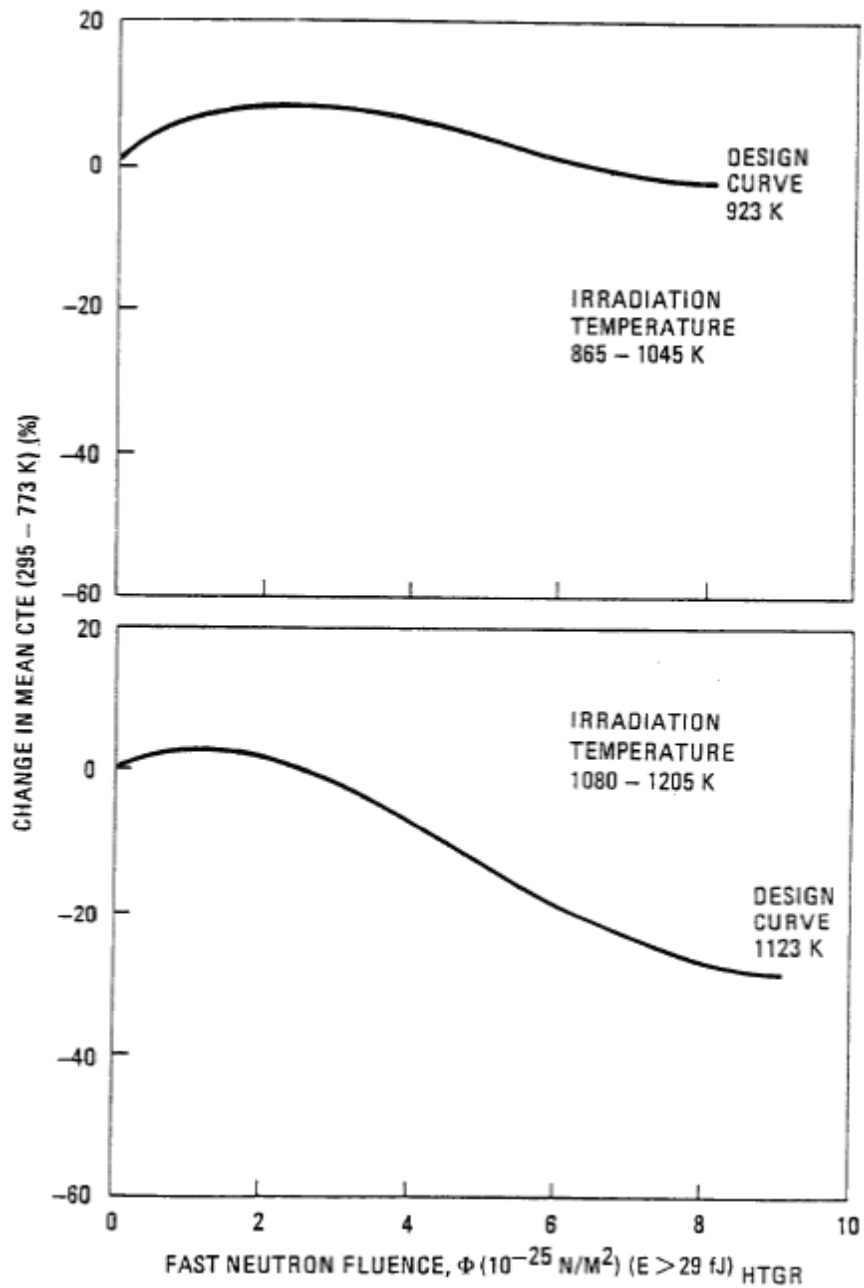
Table A1 H-451 graphite irradiation dimensional change data extracted from Fig. A1 using a data processing software (Fluence is in $\times 10^{21}$ n/m²).

Fluence at 400 °C irradiation temperature	Relative dimension change (in %) at 400 °C irradiation temperature	Fluence at 600 °C irradiation temperature	Relative dimension change (in %) at 600 °C irradiation temperature	Fluence at 800 °C irradiation temperature	Relative dimension change (in %) at 800 °C irradiation temperature
0	0	0	0	0	0
0.496264	-0.115903	0.494604	-0.028526	0.512499	0.0297482
1.16465	-0.289849	0.951573	-0.0765151	0.930357	0.039964
1.7943	-0.425007	1.6183	-0.163085	1.50208	-0.0467208
2.32894	-0.56028	2.38022	-0.259247	2.09316	-0.1528
2.88221	-0.676114	3.39009	-0.403653	2.58961	-0.278411
3.47385	-0.811318	4.15294	-0.548358	3.25837	-0.471774
4.19924	-0.985195	5.14473	-0.741329	3.81256	-0.63615
4.88645	-1.14941	5.79319	-0.866756	4.48206	-0.868347
5.61111	-1.28445	6.6326	-1.04049	5.0178	-1.06187
6.25902	-1.38075	7.47182	-1.20452	5.64929	-1.29411
7.13643	-1.55445	8.02509	-1.32036	6.29997	-1.53604
8.01328	-1.69901			6.87446	-1.76836
				7.33401	-1.95226
				8.0048	-2.25242

Table A1 H-451 graphite irradiation dimensional change data extracted from Fig. A1 using a data processing software (Fluence is in $\times 10^{21}$ n/m²).

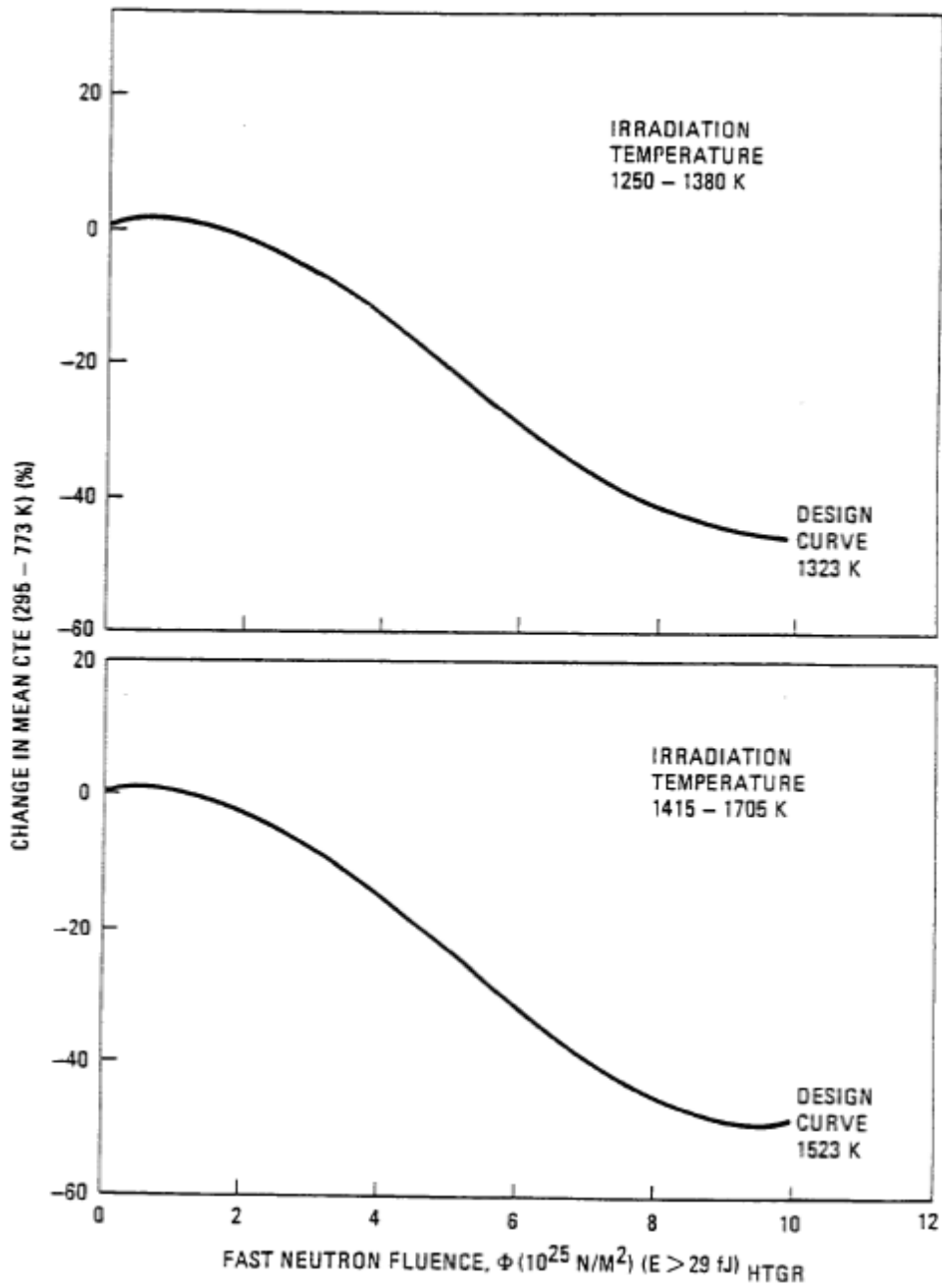
Fluence at 1000 °C irradiation temperature	Relative dimension change (in %) at 1000 °C irradiation temperature	Fluence at 1200 °C irradiation temperature	Relative dimension change (in %) at 1200 °C irradiation temperature
0	0	0	0
0.208468	0.0293792	0.306429	-0.125842
0.512314	0.0394567	0.555853	-0.251753
0.835347	0.0398487	1.03478	-0.455055
1.17904	-0.0471128	1.59118	-0.735933
1.52311	-0.153491	2.20496	-1.03616
1.90591	-0.298658	2.60788	-1.23955
2.25071	-0.44387	3.18273	-1.49128
2.59607	-0.618209	3.73822	-1.72362
2.9988	-0.811895	4.25533	-1.93658
3.55484	-1.07336	4.65732	-2.09144
4.01513	-1.2961	5.17406	-2.28498
4.49497	-1.54794	5.74744	-2.45904
5.01282	-1.79974	6.30182	-2.63313
5.5303	-2.03212	6.85583	-2.7878
5.99004	-2.22574	7.27571	-2.88437
6.50696	-2.429	7.82898	-3.00021
7.11908	-2.64185	8.03874	-3.03879
7.65409	-2.79654		
8.03579	-2.88345		

A2 Coefficient of Thermal Expansion (CTE)



(a)

Figure A2 Design curves for CTE change of H-451 graphite at (a) 650°C and 850°C and at (b) 1050°C and 1250°C, as a function of irradiation conditions (General Atomics report)⁴⁰



(b)

Figure A2 Design curves for CTE change of H-451 graphite at (a) 650°C and 850°C and at (b) 1050°C and 1250°C, as a function of irradiation conditions (General Atomics report)⁴⁰

Table A2 H-451 graphite irradiation CTE change data extracted from Figure A2a and A2b using a data processing software (Fluence is in $\times 10^{21}$ n/m²).

Fluence at 650 °C (923 K) irradiation temperature	Relative CTE change ($\alpha-\alpha_0$)/ α_0 (in %) at 650 C (923 K) irradiation temperature	Fluence at 850 °C (1123 K) irradiation temperature	Relative CTE change ($\alpha-\alpha_0$)/ α_0 (in %) at 850 C (1123 K) irradiation temperature	Fluence at 1050 °C (1323 K) irradiation temperature	Relative CTE change ($\alpha-\alpha_0$)/ α_0 (in %) at 1050 C (1323 K) irradiation temperature
0	0	0	0	0.0848958	0.0104039
0.374003	3.9858	0.432019	1.16995	0.395071	1.22489
0.885776	6.29699	0.890754	2.62326	1.18799	0.733822
1.45212	8.33263	1.56892	2.13857	2.29524	-2.95401
1.99328	8.95699	2.35699	0.544709	3.23353	-7.54491
2.61688	8.74556	3.09276	-2.45689	4.08832	-13.6166
3.26833	7.9739	3.77548	-6.30555	4.8865	-19.6953
4.21898	6.39087	4.62192	-10.977	5.7424	-26.9433
4.95325	4.50177	5.55079	-16.4803	6.56916	-33.3126
5.90543	1.79216	6.2877	-20.3229	7.73606	-40.2284
6.74808	-0.0847231	7.02385	-23.6048	8.53148	-43.3662
7.42739	-1.41663	7.75925	-26.3261	9.46727	-45.3104
8.07846	-1.90665	8.41184	-27.9351	9.89231	-45.8465
		9.03619	-28.7062		

Table A2 H-451 graphite irradiation CTE change data extracted from Figure A2b using a data processing software (Fluence is in $\times 10^{21}$ n/m²).

Fluence at 1250 (1523 K) irradiation temperature	Relative CTE change ($\alpha-\alpha_0$)/ α_0 (in %) at 1250 C (1523 K) irradiation temperature
0.0286429	-0.289905
0.425195	0.356646
1.07814	-0.135567
1.87486	-2.66546
2.58704	-5.79602
3.2144	-9.23318
3.78587	-13.5609
4.32953	-18.481
4.92937	-22.8045
5.67297	-29.1657
6.41602	-34.9388
7.2158	-40.7036
7.95773	-45.3003
8.52697	-47.2754
9.2094	-48.9398
9.94661	-48.5373

A3 Tensile Strength

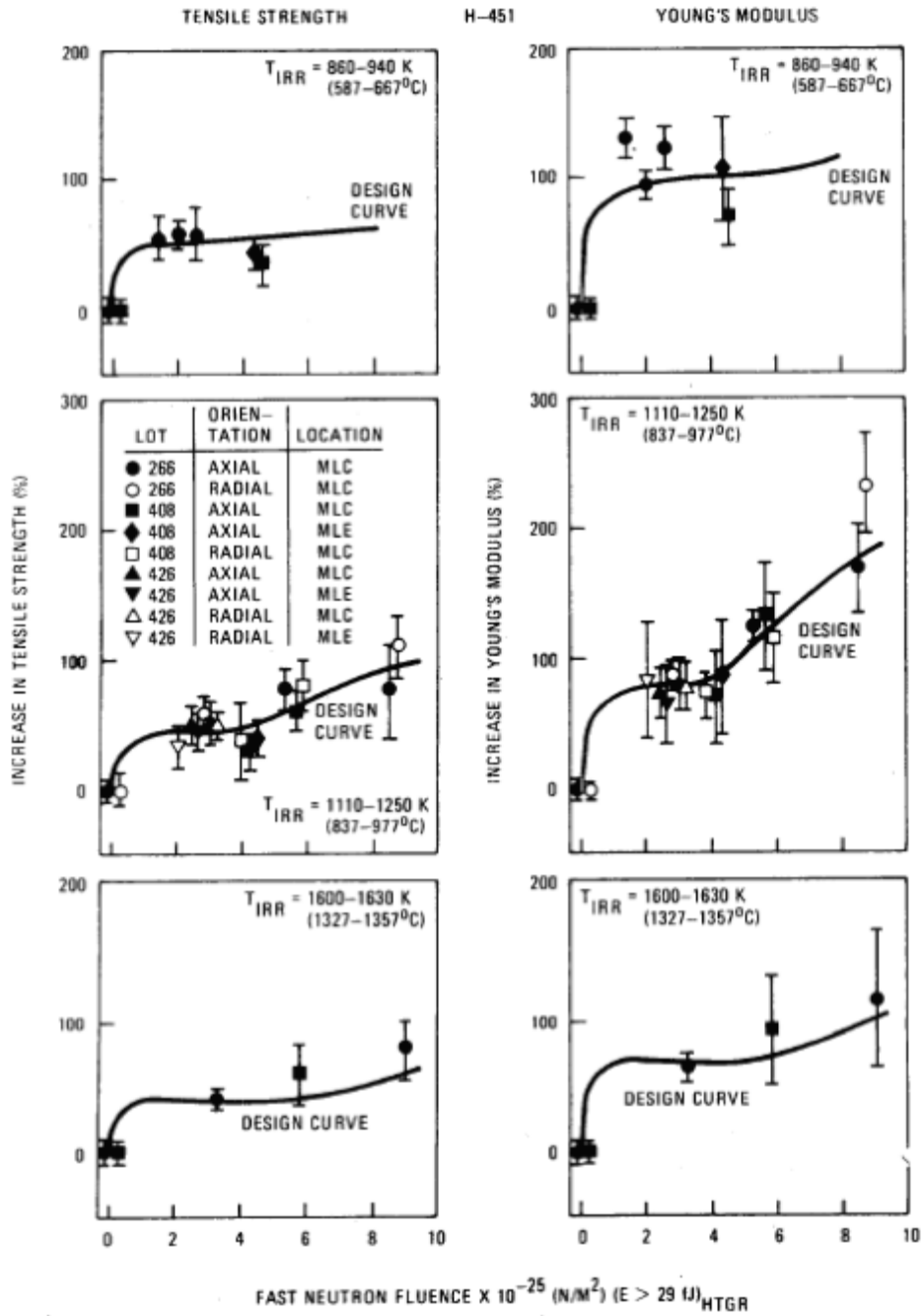


Figure A3 Design curves for UTS change of H-451 graphite, as a function of irradiation conditions (General Atomics report) ⁴⁰

Table A3 H-451 graphite irradiation UTS change data extracted from Fig. A3 using a data processing software (Fluence is in $\times 10^{25}$ n/m²).

Fluence at 587 -667 °C irradiation temperature	Increase in tensile strength (S_i-S₀)/ S₀ (%) at 587 - 667 °C irradiation temperature	Fluence at 837 - 977 °C irradiation temperature	Increase in tensile strength (S_i-S₀)/ S₀(%) at 837 – 977 °C irradiation temperature	Fluence at 1327 - 1357 °C irradiation temperature	Increase in tensile strength (S_i-S₀)/ S₀(%) at 1327 - 1357 °C irradiation temperature
0.00090481	1.49294	0	0	0	0
0.001	8.93051	0.121951	13.4874	0.103569	15.0731
0.0126674	20.9012	0.182927	22.47	0.212687	25.5964
0.141151	32.899	0.54878	34.5741	0.869244	37.2203
0.512125	45.0054	1.03659	42.2552	1.65896	39.6523
0.939197	49.6743	1.52439	45.4587	2.75754	38.82
1.42508	51.3844	2.07317	47.1969	3.91899	36.425
2.15346	53.203	2.68293	47.47	5.38191	36.8319
2.63844	53.4202	3.41463	47.7976	6.53597	40.5031
3.18494	55.1574	4.02439	51.0557	7.74921	45.6445
3.91332	56.9761	4.69512	55.8336	8.6573	51.0172
4.64079	57.3018	5.2439	62.0495	9.62641	56.3436
5.49131	60.6678	5.79268	66.7728		
6.27941	61.0206	6.21951	72.9341		
6.94716	62.8122	6.64634	77.6028		
7.49367	64.5494	7.07317	82.2716		
8.04017	66.2866	7.62195	88.4874		
		8.10976	93.1835		
		8.53659	96.3597		
		9.02439	99.5632		
		9.5122	102.767		

A4 Elastic Modulus

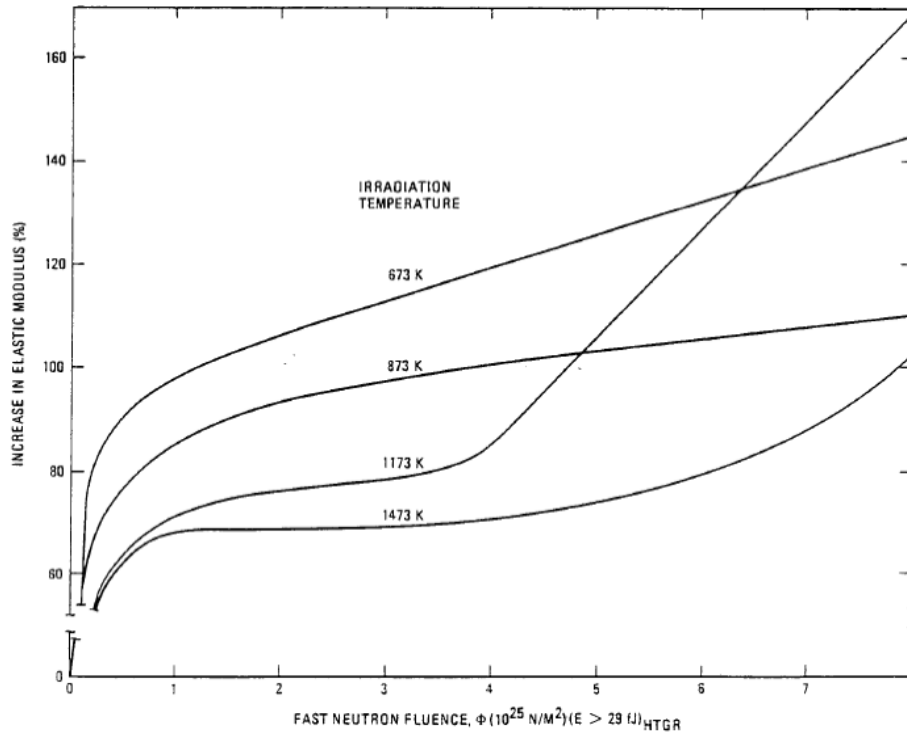


Figure A4 Design curves for elastic modulus change of H-451 graphite, as a function of irradiation conditions (General Atomics report)⁴⁰

Table A4 H-451 graphite irradiation elastic modulus change data extracted from Fig. A4 using a data processing software (Fluence is in $\times 10^{26}$ n/m²).

Fluence ($\times 10^{25}$ n/m ²) (E > 29 fJ HTGR)	Temperature			
	Percentage change in Young's modulus (E _i /E ₀ -1) ×100 at 400°C (673°K)	Percentage change in Young's modulus (E _i /E ₀ -1) ×100 at 600°C (873°K)	Percentage change in Young's modulus (E _i /E ₀ -1) ×100 at 900°C (1173°K)	Percentage change in Young's modulus (E _i /E ₀ -1) ×100 at 1200°C (1473°K)
0	0	0	0	0
0.25	83.0	68.0	54.0	52.0
0.50	90.5	76.8	63.8	62.0
0.75	95.0	81.6	68.6	66.6
1.00	98.1	85.3	71.4	68.5
1.25	100.8	88.0	73.2	69.0
1.50	102.8	90.4	75.0	69.0
1.75	104.8	92.0	75.7	69.0
2.00	106.5	93.5	76.7	69.0
2.25	108.0	94.8	77.0	69.0
2.50	109.8	95.5	77.3	69.0
2.75	111.3	96.5	78.0	69.0
3.00	113.0	97.5	78.7	69.0
3.25	114.5	98.4	79.3	69.2
3.50	116.3	99.0	80.8	70.0
3.75	117.4	100.0	82.3	70.5
4.00	119.3	100.8	85.2	71.0
4.25	121.0	101.2	90.6	71.5
4.50	122.8	102.0	95.9	72.7

Table A4 H-451 graphite irradiation elastic modulus change data extracted from Fig. A4 using a data processing software (Fluence is in $\times 10^{26}$ n/m²).

Fluence ($\times 10^{25}$ n/m ²) (E > 29 fJ HTGR)	Temperature			
	Percentage change in Young's modulus (E _i /E ₀ -1) $\times 100$ at 400°C (673°K)	Percentage change in Young's modulus (E _i /E ₀ -1) $\times 100$ at 600°C (873°K)	Percentage change in Young's modulus (E _i /E ₀ -1) $\times 100$ at 900°C (1173°K)	Percentage change in Young's modulus (E _i /E ₀ -1) $\times 100$ at 1200°C (1473°K)
4.75	124.3	102.8	101.0	73.2
5.00	126.0	103.4	106.0	74.3
5.25	127.4	104.0	111.3	75.2
5.50	129.0	104.7	116.8	76.7
5.75	130.6	105.3	122.0	78.1
6.00	132.2	105.9	127.2	79.8
6.25	133.8	106.5	132.4	81.5
6.50	135.4	107.1	137.6	83.4
6.75	137.0	107.8	142.8	85.9
7.00	138.6	108.4	148.0	88.5
7.25	140.2	109.0	153.2	91.2
7.50	141.8	109.6	158.4	94.8
7.75	143.4	110.2	163.6	98.4
8.00	145.2	110.6	169.0	103.0

A5 Thermal Conductivity

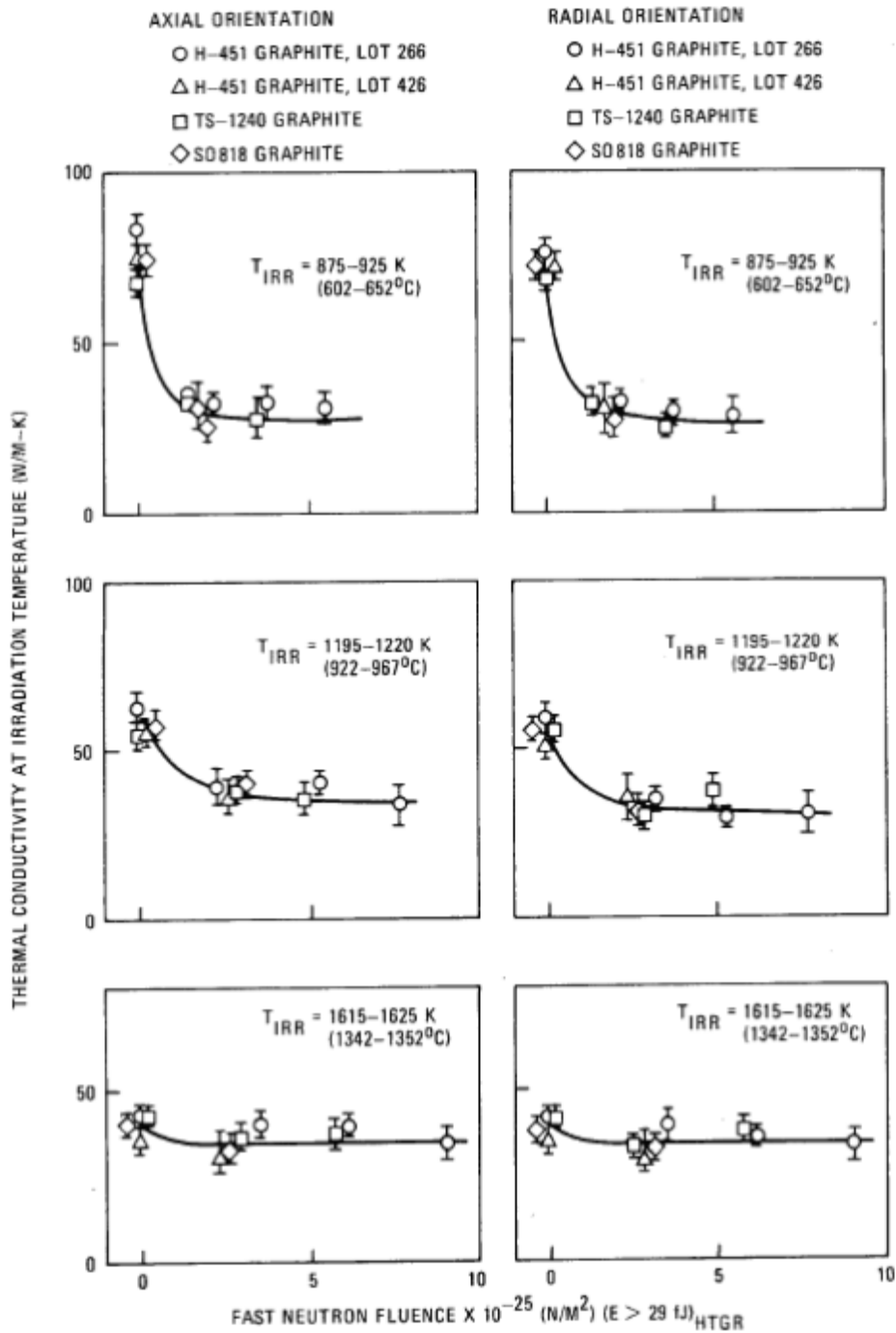


Figure A5 Design curves for thermal conductivity change of various near-isotropic graphite, as a function of irradiation conditions (General Atomics report)⁴⁰

Table A5 H-451 (axial direction) graphite irradiation thermal conductivity change data extracted from Fig. A5 using a data processing software (Fluence is in $\times 10^{25}$ n/m²).

Fluence at 602 -652 °C irradiation temperature	Thermal conductivity at 602 -652 °C irradiation temperature	Fluence at 922 - 967 °C irradiation temperature	Thermal conductivity at 922 – 967 °C irradiation temperature	Fluence at 1342 - 1352 °C irradiation temperature	Thermal conductivity at 1342 - 1352 °C irradiation temperature
0.0374387	82.946	0	62.7907	0.159852	39.0713
0.142009	74.9677	0.388889	57.5581	0.503336	37.9021
0.133617	67.5833	0.722222	49.4186	1.07603	36.1451
0.235605	57.3328	1.22222	44.7674	1.99419	34.9429
0.396979	49.3416	2.16667	40.1163	3.02926	35.4581
0.671314	40.7565	3	37.7907	3.89127	35.4085
1.28905	34.3661	3.88889	36.6279	5.38543	35.3227
2.19274	29.6153	5.11111	35.4651	7.22505	35.7917
3.26943	27.0979	6.16667	35.4651	8.25946	35.7322
4.51911	26.8138	7.33333	35.4651	9.58121	35.6563
5.48477	26.5944	7.83333	35.4651		
6.56403	26.3491				

APPENDIX B GRADE IG-110 GRAPHITE PROPERTIES DATA

B1 Dimensional Change Strain

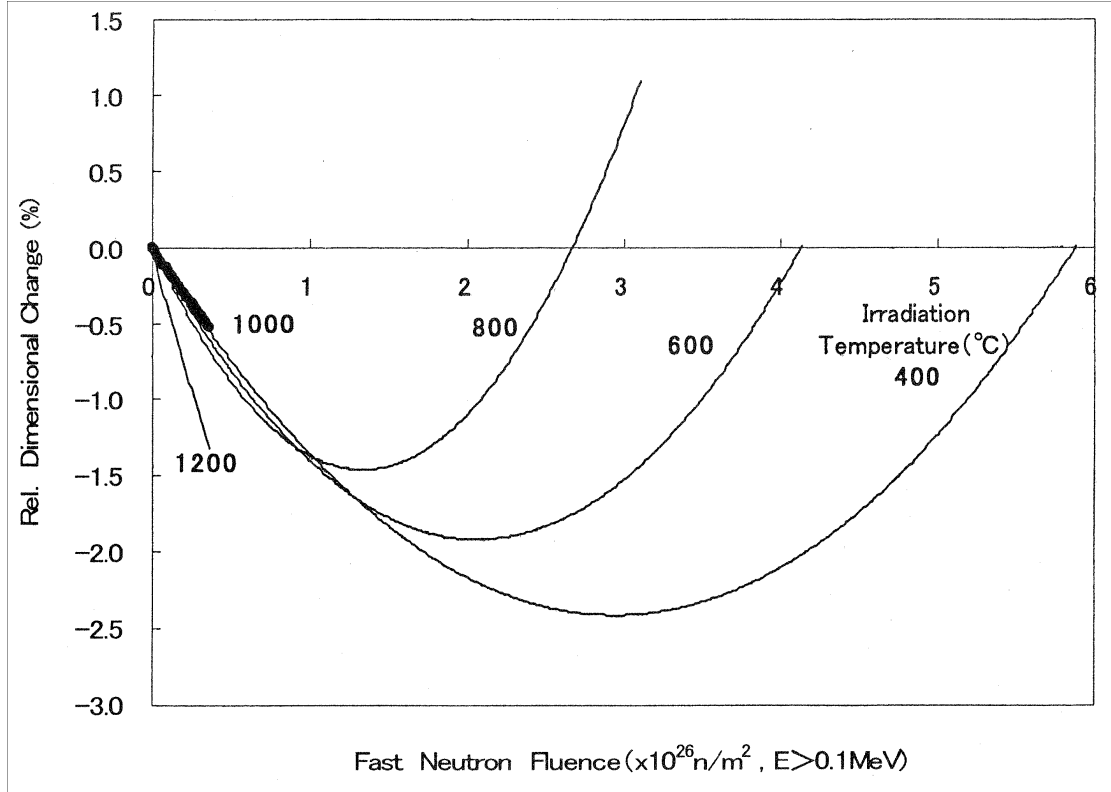


Figure B1 IG-110 graphite irradiation dimensional change data as reported in (by permission of JAERI)

Table B1 IG-110 graphite irradiation dimensional change data extracted from Fig. B1 using a data processing software (Fluence is in $\times 10^{26}$ n/m²).

Fluence at 400 °C irradiation temperature	Relative dimension change (in %) at 400 °C irradiation temperature	Fluence at 600 °C irradiation temperature	Relative dimension change (in %) at 600 °C irradiation temperature	Fluence at 800 °C irradiation temperature	Relative dimension change (in %) at 800 °C irradiation temperature
0.00497827	-0.0025561	0.0225665	-0.0280843	0.0530426	-0.104646
0.0477358	-0.0689263	0.0654756	-0.109761	0.126251	-0.245027
0.100349	-0.130204	0.151016	-0.245052	0.217199	-0.426242
0.163171	-0.222105	0.23413	-0.385443	0.310523	-0.597256
0.21356	-0.308891	0.3248	-0.538597	0.398615	-0.740203
0.311483	-0.444195	0.397731	-0.650916	0.53409	-0.916361
0.389518	-0.571826	0.485646	-0.776006	0.684524	-1.10274
0.487441	-0.70713	0.586172	-0.924068	0.812039	-1.22532
0.557793	-0.809243	0.663828	-1.01343	0.979152	-1.34539
0.658167	-0.941998	0.801678	-1.17939	1.14839	-1.42974
0.768523	-1.08242	0.936748	-1.31473	1.3245	-1.45798
0.873673	-1.19732	1.08188	-1.46539	1.49773	-1.44541
0.978899	-1.31988	1.25157	-1.59566	1.73936	-1.33851
1.14402	-1.48841	1.47844	-1.74896	1.92131	-1.20604
1.2616	-1.60843	1.69739	-1.85122	2.06833	-1.04803
1.42394	-1.74635	1.9233	-1.90757	2.1612	-0.923124
1.59378	-1.89193	2.08933	-1.91795	2.27843	-0.757427
1.73095	-1.98901	2.29968	-1.90286	2.34909	-0.640152
1.90546	-2.10654	2.49469	-1.83928	2.40994	-0.533071
2.08473	-2.20366	2.67469	-1.76038	2.48044	-0.40049
2.25139	-2.27781	2.83966	-1.66361	2.54604	-0.273006

Table B1 IG-110 graphite irradiation dimensional change data extracted from Fig. B1 using a data processing software (Fluence is in $\times 10^{26}$ n/m²).

Fluence at 400 °C irradiation temperature	Relative dimension change (in %) at 400 °C irradiation temperature	Fluence at 600 °C irradiation temperature	Relative dimension change (in %) at 600 °C irradiation temperature	Fluence at 800 °C irradiation temperature	Relative dimension change (in %) at 800 °C irradiation temperature
2.42282	-2.3341	3.02401	-1.52349	2.61159	-0.14042
2.62888	-2.38534	3.17616	-1.38334	2.66001	-0.0282245
2.81737	-2.41359	3.29139	-1.26611	2.73277	0.127314
2.96361	-2.42649	3.3992	-1.14888	2.77873	0.23696
3.18877	-2.40632	3.49212	-1.02907	2.83683	0.372105
3.39146	-2.36826	3.5727	-0.91436	2.89465	0.535312
3.60136	-2.30725	3.66307	-0.786901	2.9743	0.744414
3.81343	-2.21563	3.76799	-0.628845	3.02507	0.869362
3.97357	-2.13161	3.87039	-0.465684	3.0586	0.984124
4.1164	-2.05012	3.9532	-0.325462	3.09974	1.08102
4.25414	-1.95587	4.04089	-0.177593		
4.39917	-1.84633	4.1406	0.00597898		
4.56366	-1.70109				
4.7084	-1.56348				
4.85308	-1.41822				
4.98529	-1.26529				
5.11243	-1.0996				
5.21033	-0.982357				
5.29594	-0.875302				
5.39616	-0.742751				
5.48165	-0.62294				

Table B1 IG-110 graphite irradiation dimensional change data extracted from Fig. B1 using a data processing software (Fluence is in $\times 10^{26}$ n/m²).

Fluence at 400 °C irradiation temperature	Relative dimension change (in %) at 400 °C irradiation temperature	Fluence at 600 °C irradiation temperature	Relative dimension change (in %) at 600 °C irradiation temperature	Fluence at 800 °C irradiation temperature	Relative dimension change (in %) at 800 °C irradiation temperature
5.55966	-0.49802				
5.63535	-0.388403				
5.694	-0.309382				
5.80125	-0.136022				
5.88166	-0.00345067				
Fluence at 1000 °C irradiation temperature	Relative dimension change (in %) at 1000 °C irradiation temperature	Fluence at 1200 °C irradiation temperature	Relative dimension change (in %) at 1200 °C irradiation temperature		
0.0249671	-0.0204336	0.00505408	-0.0102092		
0.0526635	-0.0663803	0.0204943	-0.0688985		
0.0804104	-0.117429	0.0360861	-0.142894		
0.125594	-0.1787	0.0645153	-0.262821		
0.175932	-0.260384	0.0926918	-0.357237		
0.228621	-0.329315	0.118341	-0.446549		
0.271404	-0.398236	0.149121	-0.553724		
0.331623	-0.477379	0.177373	-0.655793		
0.38181	-0.543757	0.213257	-0.778279		
		0.236607	-0.885446		
		0.272112	-0.969665		
		0.297812	-1.06408		
		0.328515	-1.1636		

Table B1 IG-110 graphite irradiation dimensional change data extracted from Fig. B1 using a data processing software (Fluence is in $\times 10^{26}$ n/m²).

Fluence at 1000°C irradiation temperature	Relative dimension change (in %) at 1000°C irradiation temperature	Fluence at 1200°C irradiation temperature	Relative dimension change (in %) at 1200°C irradiation temperature
		0.356692	-1.25802
		0.377161	-1.32436

B2 CTE

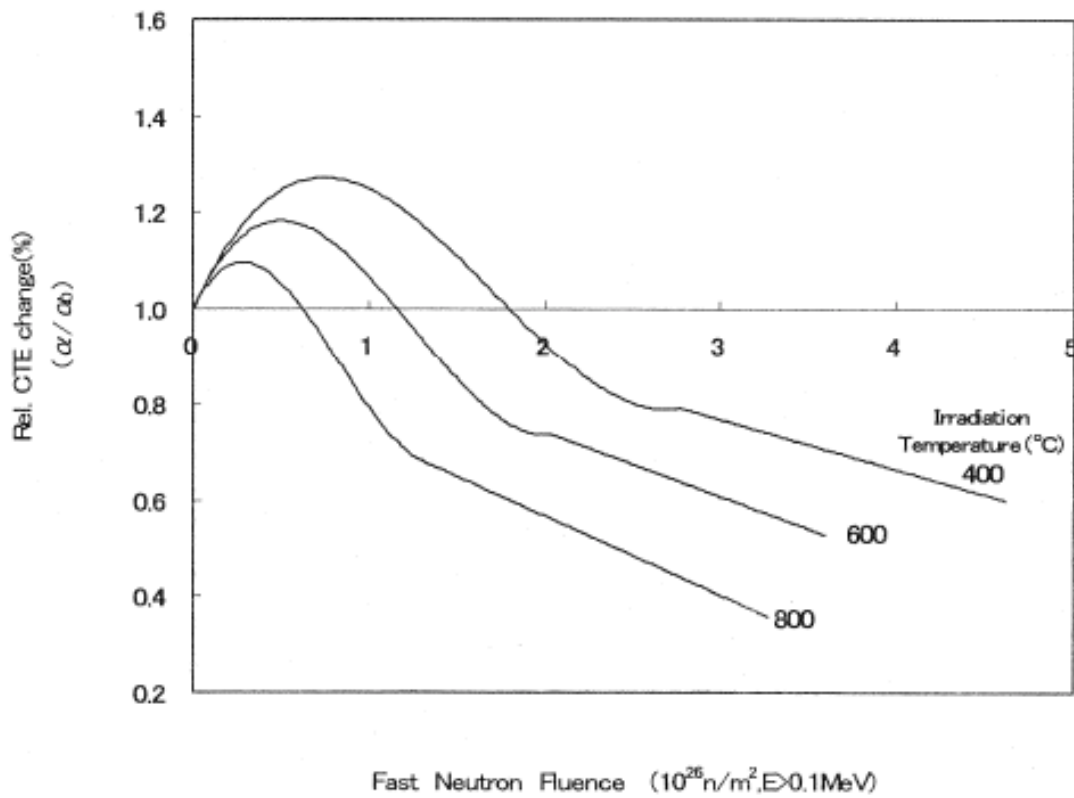


Figure B2 IG-110 graphite irradiation coefficient of thermal expansion data as reported in (by permission of JAERI)

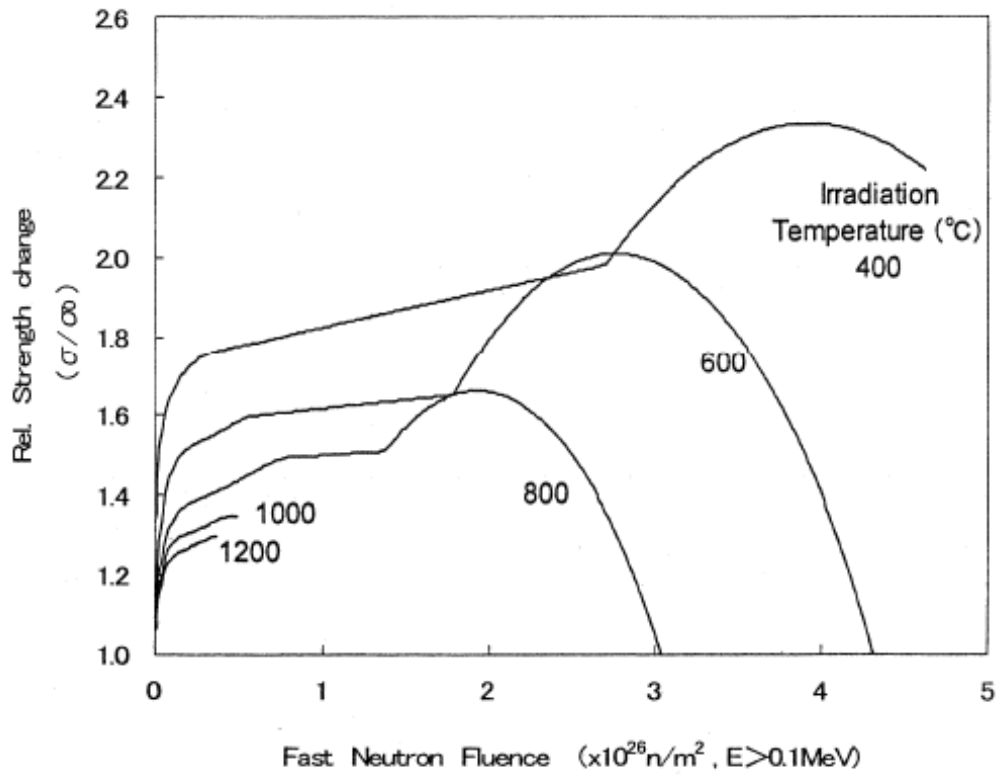
Table B2 IG-110 graphite irradiation CTE change data extracted from Fig. B2 using a data processing software (Fluence is in $\times 10^{26}$ n/m²).

Fluence at 400 °C irradiation temperature	Relative CTE change (α/α_0) at 400 C irradiation temperature	Fluence at 600 °C irradiation temperature	Relative CTE change (α/α_0) at 600 C irradiation temperature	Fluence at 800 °C irradiation temperature	Relative CTE change (α/α_0) at 800 C irradiation temperature
0.00655045	0.998406	0.0021951	0.998402	0.00869329	1.00161
0.0324038	1.02403	0.0842848	1.05928	0.0454438	1.02644
0.07344	1.05527	0.192542	1.11698	0.116898	1.06411
0.177254	1.12097	0.294527	1.15068	0.216775	1.09141
0.272558	1.16826	0.409673	1.17559	0.319082	1.09551
0.34842	1.20113	0.507582	1.18369	0.41726	1.0788
0.426537	1.22681	0.662389	1.16624	0.546205	1.03652
0.511232	1.24849	0.791185	1.13756	0.660045	0.981434
0.593827	1.26297	0.955103	1.08332	0.765166	0.927135
0.683033	1.27026	1.09942	1.02906	0.865967	0.869631
0.789739	1.27036	1.2198	0.973971	0.982115	0.802543
0.885635	1.26325	1.35107	0.917297	1.08501	0.752242
1.0776	1.23303	1.48672	0.859827	1.21184	0.704363
1.25666	1.18841	1.63321	0.805568	1.36901	0.670114
1.46425	1.12301	1.79052	0.758519	1.54355	0.640682
1.61294	1.06795	1.98458	0.736305	1.75079	0.607281
1.77034	1.0121	2.13716	0.722852	1.9384	0.577061
1.95621	0.941878	2.32472	0.697432	2.09984	0.550816
2.15509	0.876469	2.48827	0.677589	2.27218	0.522981
2.26431	0.846174	2.66276	0.652156	2.44232	0.497545
2.4149	0.815918	2.8721	0.625957	2.57543	0.472872
2.54579	0.794444	3.03134	0.60211	2.71722	0.450609

Table B2 IG-110 graphite irradiation CTE change data extracted from Fig. B2 using a data processing software (Fluence is in $\times 10^{26}$ n/m²).

Fluence at 400 °C irradiation temperature	Relative CTE change (α/α_0) at 400 C irradiation temperature	Fluence at 600 °C irradiation temperature	Relative CTE change (α/α_0) at 600 C irradiation temperature	Fluence at 800 °C irradiation temperature	Relative CTE change (α/α_0) at 800 C irradiation temperature
2.61119	0.788107	3.18397	0.583857	2.87429	0.425159
2.70919	0.788201	3.3759	0.557641	3.00303	0.402083
2.77669	0.789066	3.53509	0.536994	3.04227	0.398121
2.8835	0.779568	3.59399	0.52825	3.10992	0.385386
3.08626	0.758163			3.20808	0.37028
3.2258	0.742297			3.27353	0.359143
3.45034	0.720912				
3.68799	0.69474				
3.92344	0.670967				
4.16544	0.646399				
4.35947	0.626585				
4.51644	0.609936				
4.61675	0.597232				

B3 Tensile Strength



σ_0 : Tensile strength of unirradiated IG-110 graphite

σ : Tensile strength of irradiated IG-110 graphite

Figure B3 Design curves for UTS change of IG-110 graphite, as a function of irradiation conditions (by permission of JAERI)

Table B3 IG-110 graphite irradiation UTS change data extracted from Figure B3 using a data processing software (Fluence is in $\times 10^{26}$ n/m²).

Fluence at 400 °C irradiation temperature	Change in strength (S _i / S ₀) at 400 C irradiation temperature	Fluence at 600 °C irradiation temperature	Change in strength (S _i / S ₀) at 600 C irradiation temperature	Fluence at 800 °C irradiation temperature	Change in strength (S _i / S ₀) at 800 C irradiation temperature
0.00230415	1	0.00230415	1	0.00230415	1
0.00181438	1.04251	0.00181438	1.04251	0.00181438	1.04251
0.00141366	1.07729	0.00141366	1.07729	0.00141366	1.07729
0.00085709	1.1256	0.00085709	1.1256	0.00085709	1.1256
7.7918E-5	1.19324	0.00963957	1.16329	0.0139919	1.18551
0.00533182	1.3372	0.0112647	1.22222	0.0410405	1.23768
0.00682339	1.40773	0.0243216	1.28889	0.0656738	1.29952
0.0129789	1.47343	0.046595	1.35556	0.088437	1.32367
0.0283733	1.5372	0.0711614	1.42319	0.131882	1.35266
0.0463612	1.57585	0.116599	1.47923	0.193838	1.37488
0.0642824	1.62029	0.205993	1.51981	0.2904	1.39324
0.0847748	1.64155	0.325519	1.54493	0.368552	1.40966
0.105267	1.6628	0.463401	1.57681	0.460496	1.42899
0.141755	1.69565	0.60372	1.5971	0.568512	1.45314
0.219695	1.73043	0.774138	1.60483	0.704112	1.48309
0.339188	1.75845	0.939925	1.61449	0.800741	1.49565
0.523297	1.77778	1.08963	1.62029	0.939001	1.49469
0.661424	1.78841	1.28078	1.62802	1.08407	1.50242
0.808711	1.80386	1.45119	1.63671	1.19924	1.50628
0.969812	1.82029	1.64465	1.64444	1.30754	1.50531
1.11481	1.83478	1.78514	1.65024	1.35128	1.50918
1.26441	1.84928	1.83529	1.69662	1.42242	1.5343

Table B3 IG-110 graphite irradiation UTS change data extracted from Figure B3 using a data processing software (Fluence is in $\times 10^{26}$ n/m²).

Fluence at 400 °C irradiation temperature	Change in strength (S _i / S ₀) at 400 °C irradiation temperature	Fluence at 600 °C irradiation temperature	Change in strength (S _i / S ₀) at 600 °C irradiation temperature	Fluence at 800 °C irradiation temperature	Change in strength (S _i / S ₀) at 800 °C irradiation temperature
1.40484	1.8599	1.90163	1.73816	1.46591	1.55942
1.51532	1.87053	1.97253	1.78454	1.58751	1.60386
1.68333	1.88696	2.02292	1.81063	1.68855	1.63382
1.80534	1.89662	2.08249	1.83961	1.79201	1.65314
1.93652	1.91014	2.1627	1.87729	1.88179	1.66087
2.08612	1.92464	2.21081	1.90145	1.9832	1.65797
2.2242	1.93913	2.27503	1.92754	2.11012	1.64155
2.39457	1.95169	2.3554	1.95169	2.21874	1.61353
2.53958	1.96425	2.46798	1.97971	2.32283	1.57874
2.67765	1.97971	2.58067	1.99807	2.41083	1.5401
2.6937	1.98647	2.69576	2.00773	2.50817	1.49082
2.74639	2.01353	2.80407	2.00676	2.59638	1.43382
2.83796	2.06473	2.91481	1.9942	2.6662	1.37391
3.01445	2.14589	3.02792	1.97681	2.74998	1.30145
3.19562	2.22029	3.17123	1.9372	2.82918	1.22705
3.33569	2.26184	3.28462	1.89469	2.90392	1.1401
3.4644	2.28986	3.41204	1.83478	2.96694	1.06957
3.62308	2.31691	3.51405	1.78068	3.02765	1
3.78419	2.33237	3.5884	1.72657		
3.98465	2.33237	3.74177	1.61449		
4.16224	2.31787	3.86736	1.51304		
4.33077	2.28889	3.97457	1.40773		
4.47173	2.25411	4.06335	1.30145		

Table B3 IG-110 graphite irradiation UTS change data extracted from Figure B3 using a data processing software (Fluence is in $\times 10^{26}$ n/m²).

Fluence at 400 °C irradiation temperature	Change in strength (S_i/ S₀) at 400 C irradiation temperature	Fluence at 600 °C irradiation temperature	Change in strength (S_i/ S₀) at 600 C irradiation temperature
4.59198	2.21643	4.16151	1.18068
		4.23874	1.07729
		4.28799	1.0029
Fluence at 1000 °C irradiation temperature	Change in strength (S_i/ S₀) at 1000 C irradiation temperature	Fluence at 1200 °C irradiation temperature	Change in strength (S_i/ S₀) at 1200 C irradiation temperature
0.00230415	1	0.00230415	1
0.00181438	1.04251	0.00181438	1.04251
0.00141366	1.07729	0.00141366	1.07729
0.0100626	1.12657	0.0149269	1.10435
0.0234533	1.16425	0.0237984	1.1343
0.0436564	1.21063	0.0372114	1.17005
0.0662749	1.24734	0.0644271	1.20773
0.0959282	1.27343	0.087168	1.23382
0.144093	1.29275	0.137637	1.25314
0.213061	1.30628	0.197389	1.26667
0.300452	1.32077	0.259445	1.28019
0.369398	1.33623	0.362976	1.29372
0.447639	1.34493		
0.486821	1.34396		

B4 Elastic Modulus

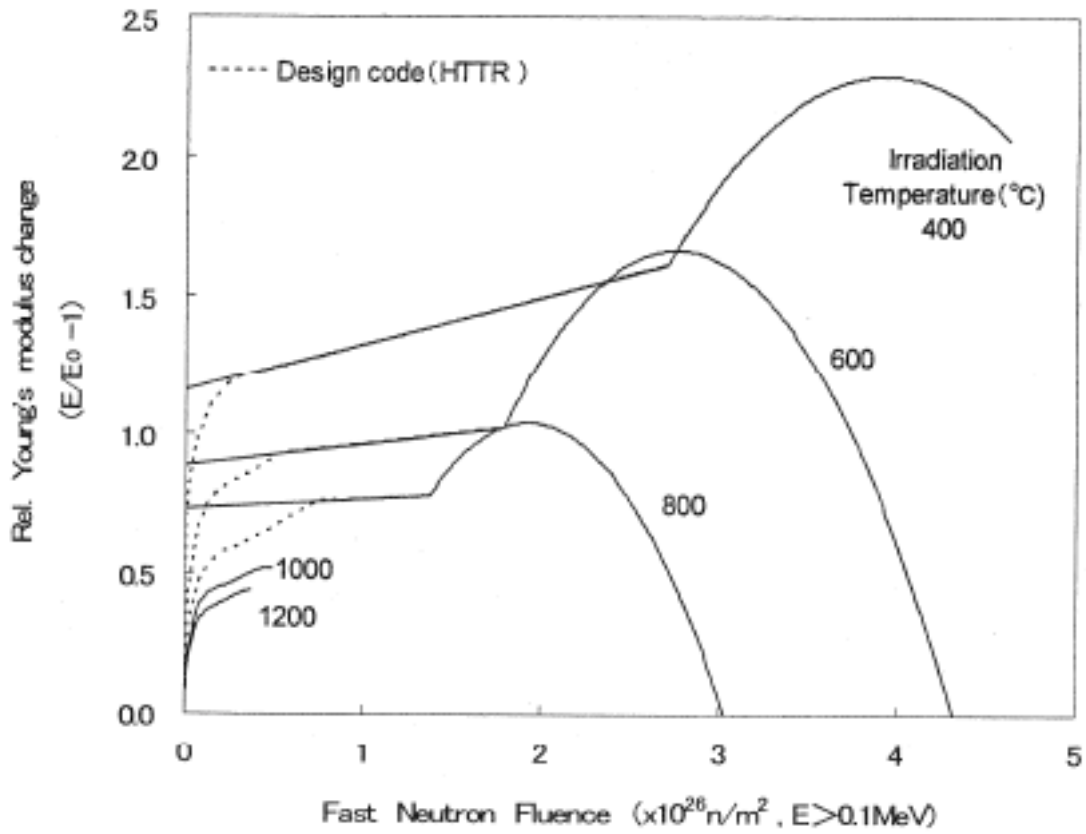


Figure B4 Design curves for elastic modulus change of IG-110 graphite, as a function of irradiation conditions (by permission of JAERI)

Table B4 IH-110 graphite irradiation elastic modulus change data extracted from Fig. B4 using a data processing software (Fluence is in $\times 10^{26}$ n/m²).

Fluence at 400°C irradiation temperature	Relative Young's modulus (E_i/E₀-1) at 400°C irradiation temperature	Fluence at 600°C irradiation temperature	Relative Young's modulus (E_i/E₀-1) at 600°C irradiation temperature	Fluence at 800°C irradiation temperature	Relative Young's modulus (E_i/E₀-1) at 800°C irradiation temperature
0.002317	0.00148	0.00175514	0.0533142	0.00413992	0.0488816
0.005067	0.15112	0.00312281	0.142165	0.00529771	0.156981
0.006917	0.55261	0.0043129	0.247303	0.0180081	0.276974
0.009572	0.70966	0.014364	0.3969	0.038228	0.351093
0.030936	0.86528	0.0387723	0.515459	0.0493446	0.402965
0.066833	0.98096	0.0589598	0.59254	0.0812301	0.478613
0.186363	1.13395	0.0768595	0.66517	0.164596	0.547067
0.246499	1.18156	0.10678	0.706753	0.294898	0.596462
0.309218	1.20992	0.164381	0.781025	0.4136	0.638407
0.481727	1.24012	0.2341	0.815366	0.527645	0.678851
0.630987	1.26136	0.292315	0.833372	0.653339	0.722305
0.840802	1.29762	0.408697	0.873826	0.748742	0.758232
1.01563	1.32931	0.487777	0.906725	0.846869	0.758631
1.20915	1.36107	0.653351	0.935533	0.940242	0.766415
1.35136	1.38525	0.763078	0.943384	1.07338	0.769919
1.52856	1.41398	0.931198	0.952953	1.23222	0.773527
1.58919	1.42308	1.11791	0.971482	1.37701	0.78004
1.71041	1.44422	1.39573	0.991863	1.42791	0.82615
1.85728	1.46989	1.63851	1.01062	1.49276	0.878241
2.02048	1.49711	1.79262	1.02013	1.55299	0.92587

Table B4 IH-110 graphite irradiation elastic modulus change data extracted from Fig. B4 using a data processing software (Fluence is in $\times 10^{26}$ n/m²).

Fluence at 400°C irradiation temperature	Relative Young's modulus (E_i/E₀-1) at 400°C irradiation temperature	Fluence at 600°C irradiation temperature	Relative Young's modulus (E_i/E₀-1) at 600°C irradiation temperature	Fluence at 800°C irradiation temperature	Relative Young's modulus (E_i/E₀-1) at 800°C irradiation temperature
2.17665	1.52577	1.82943	1.07211	1.62967	0.964682
2.29792	1.54396	1.90323	1.16125	1.74139	1.00364
2.52407	1.58175	1.99328	1.25935	1.82057	1.02765
2.64998	1.60143	2.05795	1.32773	1.93023	1.04142
2.70826	1.61199	2.12036	1.39017	2.07066	1.01978
2.73118	1.64614	2.19916	1.44824	2.1973	0.975877
2.8027	1.71749	2.28957	1.51377	2.296	0.924453
2.90658	1.81561	2.37548	1.56298	2.39955	0.85528
2.97117	1.87953	2.47775	1.61226	2.47506	0.787472
3.04286	1.93755	2.59189	1.64382	2.5554	0.704878
3.14235	2.01344	2.75058	1.66076	2.62868	0.626696
3.21419	2.0596	2.89323	1.64949	2.69031	0.545506
3.35336	2.13859	3.10192	1.58075	2.75904	0.456941
3.50201	2.20723	3.25003	1.49695	2.80657	0.383097
3.63697	2.25064	3.36073	1.41596	2.86347	0.30781
3.72786	2.26872	3.47404	1.3098	2.91347	0.22213
3.84448	2.28393	3.58741	1.19773	2.95417	0.13197
3.9636	2.28729	3.70107	1.059	3.00422	0.0418484
4.1227	2.27004	3.79109	0.945349	3.03272	-0.00097732
4.24459	2.23933	3.85524	0.84788		

Table B4 IH-110 graphite irradiation elastic modulus change data extracted from Fig. B4 using a data processing software (Fluence is in $\times 10^{26}$ n/m²).

Fluence at 400°C irradiation temperature	Relative Young's modulus (E_i/E₀-1) at 400°C irradiation temperature	Fluence at 600°C irradiation temperature	Relative Young's modulus (E_i/E₀-1) at 600°C irradiation temperature	Fluence at 800°C irradiation temperature	Relative Young's modulus (E_i/E₀-1) at 800°C irradiation temperature
4.36895	2.19827	3.91934	0.754854		
4.48653	2.1394	3.97902	0.638118		
4.58306	2.08194	4.03855	0.536189		
4.62075	2.05837	4.11721	0.392876		
		4.17445	0.286495		
		4.22696	0.184537		
		4.28903	0.0633685		
		4.31778	-0.0016675		
Fluence at 1000°C irradiation temperature	Relative Young's modulus (E_i/E₀-1) at 1000°C irradiation temperature	Fluence at 1200°C irradiation temperature	Relative Young's modulus (E_i/E₀-1) at 1200°C irradiation temperature		
0.00185201	0.04443	0.0020296	0.0281425		
0.00792466	0.130338	0.00388161	0.0725726		
0.0254692	0.235543	0.00811839	0.11257		
0.0481222	0.300788	0.0123552	0.152568		
0.068439	0.366024	0.0235203	0.199997		
0.112297	0.415067	0.0416621	0.250416		

Table B4 IH-110 graphite irradiation elastic modulus change data extracted from Fig. B4 using a data processing software (Fluence is in $\times 10^{26}$ n/m²).

Fluence at 1000 °C irradiation temperature	Relative Young's modulus (E_i/E_0-1) at 1000 °C irradiation temperature	Fluence at 1200 °C irradiation temperature	Relative Young's modulus (E_i/E_0-1) at 1200 °C irradiation temperature
0.184384	0.446457	0.0598524	0.296394
0.256634	0.463039	0.101358	0.346908
0.324162	0.484045	0.150082	0.378202
0.380024	0.503522	0.210633	0.396218
0.456978	0.517162	0.266512	0.414215
0.489703	0.515814	0.327063	0.43223
		0.366732	0.436834
0.00185201	0.04443	0.0020296	0.0281425
0.00792466	0.130338	0.00388161	0.0725726
0.0254692	0.235543	0.00811839	0.11257
0.0481222	0.300788	0.0123552	0.152568
0.068439	0.366024	0.0235203	0.199997
0.112297	0.415067	0.0416621	0.250416
0.184384	0.446457	0.0598524	0.296394
0.256634	0.463039	0.101358	0.346908
0.324162	0.484045	0.150082	0.378202
0.380024	0.503522	0.210633	0.396218
0.456978	0.517162	0.266512	0.414215
0.489703	0.515814	0.327063	0.43223
		0.366732	0.436834

B5 Thermal Conductivity

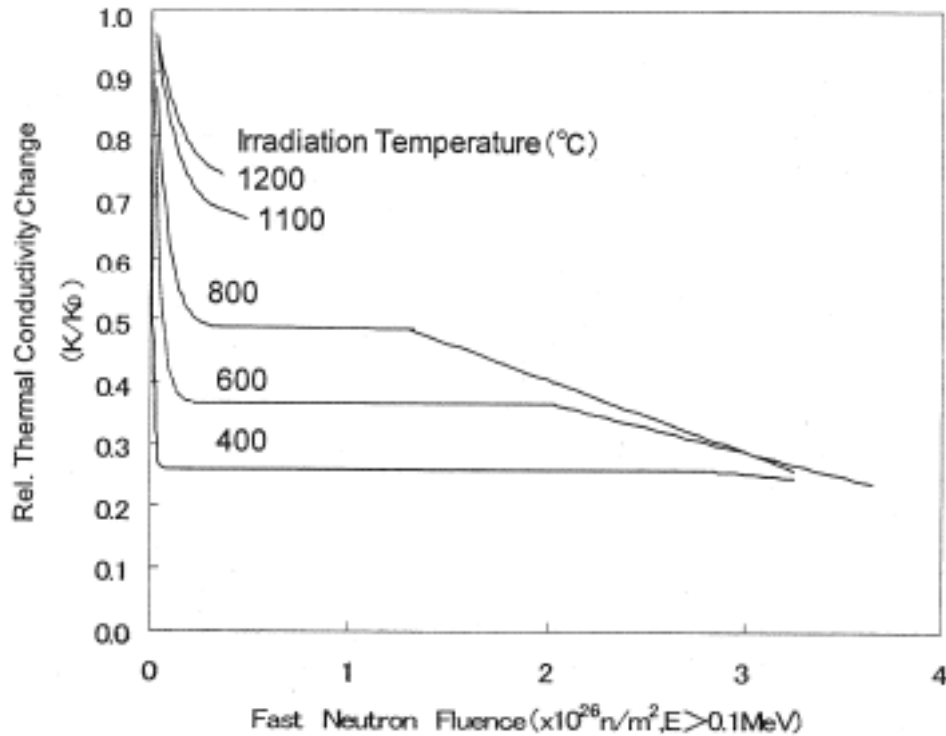


Figure B5 Design curves for thermal conductivity change of IG-110 graphite, as a function of irradiation conditions (by permission of JAERI)

Table B5 IG-110 graphite irradiation thermal conductivity change data extracted from Fig. B5 using a data processing software (Fluence is in $\times 10^{26}$ n/m²).

Fluence at 400°C irradiation temperature	Relative change in thermal conductivity (K_i/K_0) at 400°C irradiation temperature	Fluence at 600°C irradiation temperature	Relative change in thermal conductivity (K_i/K_0) at 600°C irradiation temperature	Fluence at 800°C irradiation temperature	Relative change in thermal conductivity (K_i/K_0) at 800°C irradiation temperature
0.00415435	0.969249	0.00660223	0.936256	0.0254439	0.874218
0.00435441	0.959741	0.0112862	0.880338	0.0331053	0.843475
0.00539006	0.910527	0.0123689	0.828887	0.0392956	0.799305
0.00291863	0.861304	0.0238434	0.78361	0.0490166	0.754025
0.00250673	0.797545	0.0302808	0.727696	0.060444	0.710985

Table B5 IG-110 graphite irradiation thermal conductivity change data extracted from Fig. B5 using a data processing software (Fluence is in $\times 10^{26}$ n/m²).

Fluence at 400°C irradiation temperature	Relative change in thermal conductivity (K_i/K_0) at 400°C irradiation temperature	Fluence at 600°C irradiation temperature	Relative change in thermal conductivity (K_i/K_0) at 600°C irradiation temperature	Fluence at 800°C irradiation temperature	Relative change in thermal conductivity (K_i/K_0) at 800°C irradiation temperature
0.00670815	0.764556	0.0350354	0.668423	0.0806508	0.667406
0.0101681	0.683468	0.0457213	0.577283	0.0920194	0.627163
0.0113097	0.62922	0.0555953	0.524733	0.115545	0.59254
0.00962679	0.542527	0.0670344	0.481134	0.139235	0.550088
0.00881475	0.497783	0.0818748	0.442577	0.201445	0.510518
0.0200656	0.463132	0.105436	0.406276	0.282519	0.491124
0.0205011	0.44244	0.142813	0.380073	0.361511	0.487386
0.0229136	0.411125	0.211507	0.365686	0.47023	0.487629
0.0290569	0.369193	0.346541	0.365429	0.607041	0.486257
0.026456	0.326122	0.472819	0.364592	0.738556	0.486552
0.0394369	0.292594	0.590282	0.365974	0.859573	0.485704
0.0417082	0.26799	0.765647	0.365807	0.987593	0.485431
0.0717066	0.259109	1.05152	0.364209	1.12087	0.48517
0.154146	0.258175	1.26545	0.364688	1.26116	0.485484
0.28918	0.257918	1.44608	0.364533	1.34544	0.480079
0.464545	0.257751	1.67404	0.365043	1.42986	0.468523
0.669709	0.25821	1.83185	0.365396	1.52126	0.458661
0.885417	0.257574	2.03704	0.364736	1.62843	0.448833
1.09408	0.2586	2.1723	0.353853	1.75329	0.432334
1.42376	0.258219	2.29175	0.344053	1.87811	0.417513

Table B5 IG-110 graphite irradiation thermal conductivity change data extracted from Fig. B5 using a data processing software (Fluence is in $\times 10^{26}$ n/m²).

Fluence at 400 °C irradiation temperature	Relative change in thermal conductivity (K_i/K_0) at 400 °C irradiation temperature	Fluence at 600 °C irradiation temperature	Relative change in thermal conductivity (K_i/K_0) at 600 °C irradiation temperature	Fluence at 800 °C irradiation temperature	Relative change in thermal conductivity (K_i/K_0) at 800 °C irradiation temperature
1.75519	0.258401	2.46387	0.331575	2.00638	0.404936
2.14274	0.258709	2.60442	0.319026	2.12767	0.391225
2.42684	0.257666	2.73089	0.309241	2.26305	0.37475
2.65479	0.258736	2.92936	0.294585	2.4002	0.357159
2.85824	0.257513	3.12257	0.279357	2.539	0.344606
3.01794	0.251718	3.31052	0.264677	2.66209	0.328662
3.13024	0.248614	3.46336	0.251596	2.80098	0.311635
3.24955	0.245525	3.64426	0.238578	2.94857	0.297983
				3.05587	0.282563
				3.24928	0.258388
Fluence at 1100 °C irradiation temperature	Relative change in thermal conductivity (K_i/K_0) at 1100 °C irradiation temperature	Fluence at 1200 °C irradiation temperature	Relative change in thermal conductivity (K_i/K_0) at 1200 °C irradiation temperature		
0.025644	0.948044	0.0253498	0.962025		
0.0348235	0.92849	0.0399429	0.935212		
0.0404607	0.910605	0.0563485	0.905607		
0.0515822	0.882106	0.0886653	0.869885		
0.0822043	0.843584	0.135222	0.824128		
0.102176	0.811191	0.183321	0.788441		

Table B5 IG-110 graphite irradiation thermal conductivity change data extracted from Fig. B5 using a data processing software (Fluence is in $\times 10^{26}$ n/m²).

Fluence at 1100 °C irradiation temperature	Relative change in thermal conductivity (K_i/K_0) at 1100 °C irradiation temperature	Fluence at 1200 °C irradiation temperature	Relative change in thermal conductivity (K_i/K_0) at 1200 °C irradiation temperature
0.129185	0.777694	0.248766	0.761742
0.164891	0.747572	0.31047	0.74622
0.216426	0.715249	0.36683	0.734601
0.28532	0.691354		
0.362746	0.678664		
0.485788	0.664957		

B6 Creep Coefficient

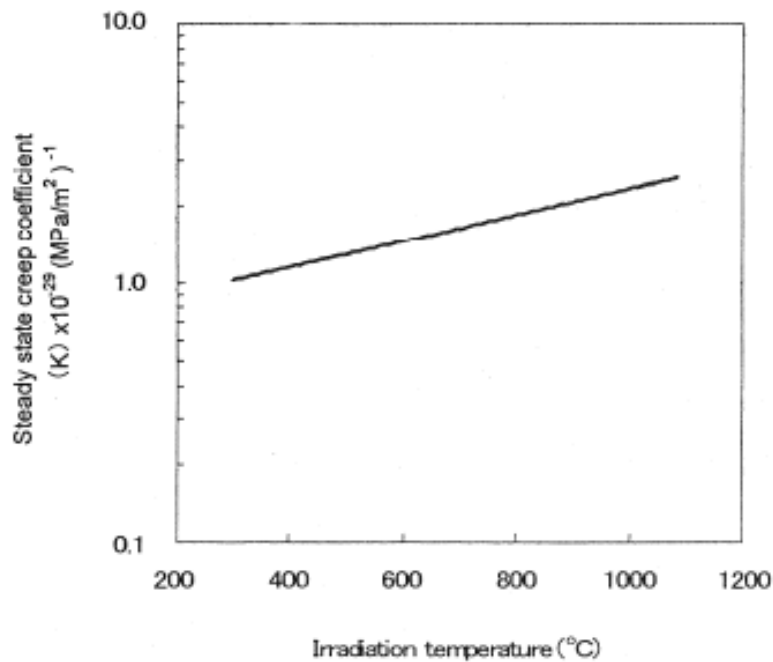


Figure B6 Creep coefficient plot of IG-110 graphite, as a function of temperature (by permission of JAERI)

Table B6 The numerical values of the IG-110 irradiation creep coefficient extracted from Fig. B6 using a data processing software.

Irradiation temperature (°C)	Steady state creep coefficient $K \times 10^{-29} (\text{MPa-n/m}^2)^{-1}$
298.08	1.02108
359.712	1.10862
415.481	1.17921
475.942	1.27281
522.318	1.33803
561.058	1.41068
601.566	1.46996
647.941	1.54981
684.926	1.61019
718.969	1.68767
755.362	1.7689
788.825	1.83241
829.328	1.92626
869.242	2.03086
912.096	2.12865
952.013	2.23113
986.062	2.31802
1018.34	2.42244
1048.87	2.49473
1084.67	2.63788